

SCANNED PROBE MICROSCOPY STUDIES OF  
THIN ORGANIC FILMS USING CANTILEVER  
FREQUENCY NOISE

A Dissertation

Presented to the Faculty of the Graduate School

of Cornell University

in Partial Fulfillment of the Requirements for the Degree of

Doctor of Philosophy

by

Showkat Monika Yazdanian

August 2009

© 2009 Showkat Monika Yazdanian

ALL RIGHTS RESERVED

SCANNED PROBE MICROSCOPY STUDIES OF THIN ORGANIC FILMS  
USING CANTILEVER FREQUENCY NOISE

Showkat Monika Yazdanian, Ph.D.

Cornell University 2009

Scanned probe microscopy techniques can be used to create nanometer-resolution surface maps of forces as small as an attonewton. In this work, a new method for measuring local electric field gradients at the surface of a polymer film is presented.

The centerpiece of this thesis is a protocol for measuring and deciphering noise in a cantilever's resonance frequency (Chapter 4). The protocol was tested on thin polymer film samples; these measurements confirmed the predictions of a zero-free parameter theory described in Chapter 3, which relates cantilever frequency noise to local dielectric fluctuations emanating from within the polymer.

Chapter 5 is a presentation of preliminary efforts towards achieving a local measurement of carrier mobility in an organic semiconductor.

## BIOGRAPHICAL SKETCH

Showkat completed her thesis work in the Department of Chemistry and Chemical Biology under the supervision of Professor John Marohn. She spent a significant portion of her time at the Cornell Nanoscale Science and Technology Facility, learning methodologies and techniques for manipulating matter at the nanoscale. Many more happy hours were spent in the Baker building with the Marohn group's custom-built force microscopes.

Showkat completed course-work in Quantum Chemistry, Statistical Thermodynamics, Solid State Physics, and Mathematics for the Physical Sciences. Outside of the lab, she enjoyed barbeques at Stewart Park, hiking, touring the Finger Lakes, and ice cream at the Cornell Dairy Bar.

Dedicated to the memory of Jeevan Marc Mykoo (b. Diego Martin, Trinidad,  
May 29 1977; d. Ithaca, United States, July 22 2007).

## **ACKNOWLEDGEMENTS**

First, I thank my parents for the education I have been so fortunate to receive, and the rest of my family for their support.

I thank my supervisor, Professor John Marohn, for cheerfully teaching me how to be a scientist. I am grateful above all for his unabashed and infectious enthusiasm for science. I am also indebted to my committee member and collaborator Professor Roger Loring, and to Tom McCarrick.

I have met many good friends and good teachers in the Marohn group. Bill Silveira and Tse Nga Ng initiated me into the lab. Seppe Kuehn taught me much of what I know about scanned probe microscopy and the importance of "doing things right". Steven Hickman has been of great assistance at the nanofabrication facility and Nikolas Hoepker has been an invaluable lab partner. Thanks also to lab mates past and present: Eric Moore, SangGap Lee, Justin Luria, Sarah Wright, Jonilyn Longnecker, Boyan Penkov and Michael Jaquith as well as my three undergraduate students True Merrill, Rebecca Lee and Robert Bruce.

Anna and Johannes Hachmann, Clare Kelleher, Tamara Church, Aviva Litovitz, Dominika Zgid, Garnet Chan, Chris Orilall, Georgios Markopoulos, Nancy Nead, Ying Luu, Franco Saliola and especially Francesco Matucci have filled these five years in Ithaca with warmth and laughter.

Finally, I thank my husband and best friend, Alexander Fishman.

## TABLE OF CONTENTS

Biographical Sketch . . . . .	iii
Dedication . . . . .	iv
Acknowledgements . . . . .	v
Table of Contents . . . . .	vi
List of Tables . . . . .	ix
List of Figures . . . . .	x
<b>1 Introduction</b>	<b>1</b>
1.1 The limits of force detection . . . . .	1
1.2 Atomic force microscopy . . . . .	2
1.3 Electric force microscopy . . . . .	3
1.4 Non-contact friction and frequency jitter . . . . .	6
1.5 Summary and outline of the thesis . . . . .	7
<b>2 Apparatus</b>	<b>9</b>
2.1 Summary . . . . .	9
2.2 Microscope super-structure . . . . .	11
2.3 Vertical positioning . . . . .	12
2.4 Lateral positioning . . . . .	14
2.5 Voltage sources . . . . .	15
2.6 Protective box for piezo stack . . . . .	18
2.7 Sample holder and cantilever holder . . . . .	19
2.8 Vibration isolation and vacuum . . . . .	21
2.9 Interferometer . . . . .	22
2.10 Cantilever design . . . . .	23
2.11 Cantilever fabrication . . . . .	25
2.12 Measurement protocols . . . . .	28
2.13 Drive circuit . . . . .	30
2.14 Locating the surface . . . . .	33
<b>3 Theory of cantilever jitter over thin polymer films</b>	<b>35</b>
3.1 Summary . . . . .	35
3.2 Literature survey: theoretical studies of jitter and non-contact friction . . . . .	36
3.3 Description of the system . . . . .	38
3.4 Derivation of cantilever frequency shift induced by a fluctuating electric field . . . . .	40
3.5 Friction and jitter . . . . .	42
3.6 Field correlation functions from linear response theory . . . . .	44
3.7 Connection between non-contact friction and electric field correlation function . . . . .	45
3.8 Solving for the reaction field . . . . .	47

3.9	Connection between frequency jitter and electric field gradient correlation function . . . . .	48
3.10	Comparison to results of Israeloff et al. . . . .	52
3.11	Field correlation functions from stochastic electrodynamics . . . . .	53
3.12	Conclusions . . . . .	54
<b>4</b>	<b>Measurement of low-frequency cantilever noise over thin polymer films</b>	<b>55</b>
4.1	Summary . . . . .	55
4.2	Literature survey: scanned probe studies of electric field fluctuations . . . . .	56
4.3	Configuration of the experiment . . . . .	58
4.4	Cantilever noise in the frequency domain . . . . .	60
4.5	Cantilever frequency noise in the absence of a sample . . . . .	63
4.6	Cantilever frequency noise over a thin polymer film . . . . .	65
4.7	Bandwidth . . . . .	67
4.8	Amplitude dependence of jitter . . . . .	68
4.9	Dependence of jitter on tip charge . . . . .	69
4.10	Comparison of predicted and measured power spectra . . . . .	71
4.11	Inputs to the theory: capacitance, dielectric spectra and contact potential . . . . .	72
4.12	Theory versus experiment . . . . .	74
4.13	The contact potential . . . . .	77
4.14	Origin of the parabolic dependence of friction and frequency on tip charge . . . . .	79
4.15	Additional sources of jitter: cantilever anharmonicity . . . . .	83
4.16	Sensitivity . . . . .	84
<b>5</b>	<b>Toward a local measurement of carrier mobility in organic field effect transistors</b>	<b>86</b>
5.1	Summary . . . . .	86
5.2	Why organic semiconductors? . . . . .	88
5.3	Introduction to field effect transistors . . . . .	90
5.4	Literature survey: theoretical descriptions of carrier mobility in organic semiconductors . . . . .	93
5.5	Literature survey: experimental techniques for measuring mobility in organic semiconductors . . . . .	95
5.6	Literature survey: non-contact friction studies of semiconductor devices . . . . .	97
5.7	A new approach to measuring carrier mobility in an organic semiconductor . . . . .	98
5.8	Experiment: substrate fabrication . . . . .	102
5.9	Experiment: preparation of thin organic films . . . . .	102
5.10	Non-contact friction over a thin polythiophene film . . . . .	105

5.11	Summary and future directions . . . . .	107
<b>A</b>	<b>CAD drawings for renovated dissipation microscope</b>	<b>109</b>
<b>B</b>	<b>Cantilever fabrication recipe</b>	<b>116</b>
B.1	Tip thinning pits . . . . .	116
B.2	Cantilever definition . . . . .	118
B.3	Backside processing . . . . .	119
<b>C</b>	<b>Substrate fabrication recipe</b>	<b>122</b>
<b>D</b>	<b>Dielectric spectroscopy</b>	<b>124</b>
<b>E</b>	<b>Measurement of the minimum detectable force</b>	<b>128</b>
E.1	Introduction to the minimum detectable force . . . . .	128
E.2	Details of the measurement of $k$ . . . . .	131
<b>Bibliography</b>		<b>134</b>

## LIST OF TABLES

## LIST OF FIGURES

1.1	Atomic force microscope . . . . .	4
1.2	Contrast between atomic and electric force microscopes . . . . .	6
2.1	Rendering of the microscope . . . . .	10
2.2	Principle of coarse motion in a piezo actuator . . . . .	13
2.3	Photograph of scanning probe microscope with lateral scanning capabilities . . . . .	17
2.4	Renderings of the protective box for the Attocube nano-positioners	18
2.5	Photograph of sample holder . . . . .	19
2.6	Renderings of the sliding “drawer” holding the cantilever to the microscope . . . . .	21
2.7	What is $Q$ ? . . . . .	24
2.8	Cantilever fabrication process . . . . .	26
2.9	Scanning electron micrographs of a custom-fabricated cantilever	27
2.10	Scanning electron micrographs of a custom-fabricated cantilever	28
2.11	Common failures of the fabrication process . . . . .	29
2.12	Experimental observables . . . . .	29
2.13	Linearity of the drive circuit . . . . .	31
2.14	Response of cantilever amplitude to drive voltage . . . . .	31
2.15	Two different ways to measure $Q$ . . . . .	32
2.16	Natural decay of $Q$ in an increasing pressure environment . . . . .	33
3.1	Configuration of the experiment . . . . .	39
4.1	Measurement protocol for dielectrics . . . . .	58
4.2	Polymers studied . . . . .	60
4.3	Visual algorithm for separating signal from noise . . . . .	61
4.4	Visual algorithm for generating a power spectrum of cantilever frequency fluctuations . . . . .	62
4.5	Power spectrum of frequency noise in the absence of a sample . .	64
4.6	Cantilever frequency fluctuations over a 200 nm thick film of PMMA at large tip-sample separation . . . . .	66
4.7	Cantilever frequency jitter in a 100 Hz bandwidth . . . . .	69
4.8	Frequency jitter versus tip-sample voltage over a 466 nm thick film of PMMA . . . . .	70
4.9	Observed and calculated power spectra of cantilever frequency fluctuations over a thin film of PMMA . . . . .	73
4.10	Dependence of jitter on tip-sample separation for six polymer films	75
4.11	Simultaneously acquired jitter, non-contact friction and frequency	78
4.12	Frequency shift versus applied tip-sample voltage over epitaxial gold . . . . .	80
4.13	Frequency shift versus applied tip-sample voltage at different heights . . . . .	81

4.14	Forces acting on a cantilever oscillating parallel to the sample surface . . . . .	81
4.15	Dependence of cantilever frequency on drive amplitude . . . . .	84
5.1	Small molecules for organic semiconductors . . . . .	88
5.2	Organic semiconductors: organic polymers . . . . .	89
5.3	Thin film transistor . . . . .	91
5.4	Charge motion through an organic semiconductor . . . . .	92
5.5	Characteristic current-voltage curves for a TPD field-effect transistor . . . . .	93
5.6	Schematic of the charge carrier experiment . . . . .	101
5.7	Two different field-effect transistor architectures . . . . .	103
5.8	Output curves for a polythiophene field-effect transistor . . . . .	105
5.9	Friction parabolas over a thin film of polythiophene . . . . .	108
5.10	Output curves for a polythiophene field-effect transistor . . . . .	108
A.1	CAD: Protective box for Attocubes . . . . .	110
A.2	CAD: Brass rings supporting piezo stack . . . . .	111
A.3	CAD: Thick brass ring supporting piezo stack . . . . .	112
A.4	CAD: Adaptor piece for cantilever mount . . . . .	113
A.5	CAD: Slider piece for cantilever mount . . . . .	114
A.6	CAD: Adaptor for pin connector . . . . .	115
D.1	Dielectric spectroscopy apparatus . . . . .	125
D.2	Dielectric spectra of PMMA and PVAc . . . . .	126
E.1	Power spectrum of cantilever frequency fluctuations . . . . .	130
E.2	Method for calculating cantilever spring constant . . . . .	132

# CHAPTER 1

## INTRODUCTION

### 1.1 The limits of force detection

The detection of small forces has been of interest since at least 1798, when Henry Cavendish first succeeded in detecting the gravitational force between lead spheres with a resolution of  $10^{-8}$  N [1]. With the invention of the atomic force microscope (AFM) in 1986 by Binnig, Quate and Gerber [2], the detection of much smaller forces, in the range of  $10^{-10}$  to  $10^{-13}$  N, has become routine. Forces of this magnitude are suitable for atomic resolution imaging because they can be exerted between a probe tip and a sample without seriously perturbing the surface atomic structure [1]. By comparison, the force required to break a chemical bond is roughly a nanonewton ( $10^{-9}$  N) and the force between two electrons situated a micron apart is about 0.1 femtonewtons ( $10^{-16}$  N).

Recent innovations in the fabrication of mechanical resonators have facilitated the detection of forces as small as an attonewton ( $10^{-18}$  N); for ease of reference, we shall henceforth refer to these measurements as “ultra-sensitive”. Ultra-sensitive cantilevers have thus opened up the possibility of access to an even more remote realm of forces. In 1997, Stowe *et al.* [3] measured a 36 aN electrostatic force between a cantilever tip and a gold electrode situated 1 mm apart in high vacuum and at a temperature of  $T = 4.8$  K. Ultra-sensitive cantilevers have since demonstrated a force sensitivity as good as 0.82 aN in a 1 Hz bandwidth in high vacuum at  $T = 110$  mK [4]. Ultra-sensitive cantilevers have been used to study local dopant density [5], to measure the magnetic properties of individual nanomagnets [6, 7, 8], and to detect magnetic resonance from

small numbers of nuclear spins [9, 10] and from individual electron spins [11]. Ultra-sensitive cantilevers will be used in this thesis to explore the mechanisms of non-contact friction and to probe minute electric field (and field gradient) fluctuations near surfaces [12, 13, 14, 15].

## 1.2 Atomic force microscopy

A schematic of the operation of an atomic force microscope is shown in Figure 1.1. The force sensor in an AFM is a sharp tip mounted on the end of a flexible cantilever that is usually made of silicon or silicon nitride. The separation between the tip and a sample is adjusted by means of a piezoceramic actuator. Once the tip and sample are in close proximity, the tip is “scanned” parallel to the  $xy$  plane in length increments of roughly a few nanometers, and forces acting on the tip cause the cantilever to deflect. This deflection is typically detected by using a four-quadrant photodiode to infer the deflection of a laser beam as it is reflected from the cantilever end. Older microscopes operated in “contact mode”, whereby the tip was brought into contact with the sample surface and deflection was caused by the inter-atomic repulsion between the tip and the sample. “Tapping mode” operation is much more common, and entails applying a driving force to the cantilever, then monitoring changes in its oscillation amplitude as it scans along a sample surface.

AFM is now only one element of a large set of scanned probe microscopies. The original ensemble of a flexible micro-mechanical force sensor, deflection detector and actuating element has since been combined with other technologies to create new techniques for mapping magnetization [16], electrostatic poten-

tial [17], chemical forces [18], capacitance [17], dopant density in semiconductors [5], magnetic resonance [19] and dielectric fluctuations [13].

Atomic force microscopy not only enabled the detection of minute forces, it also provided a glimpse into the local spatial distribution of these forces. Binning and Quate's seminal paper on the topography of an  $\text{Al}_2\text{O}_3$  surface was the first study to map atomic forces at mesoscale lateral resolution. The mesoscopic realm falls into the sizeable grey area between the quantum and the bulk and typically describes regions comprised of a few thousand atoms or molecules. Surprisingly, the bulk behavior of a material can be strongly influenced by its ordering on the mesoscopic scale [20]. For instance, it was shown by Surin and co-workers [21] via atomic force microscopy that thin films of polythiophene (an organic semiconductor) are a patchwork of crystalline and amorphous regions and that the ratio of these areas can significantly affect the bulk conductivity.

The AFM can be used not only to sense forces but also to apply them. In 1989, researchers at IBM's Almaden research center demonstrated the ability to manipulate individual atoms with atomic-scale precision, forming the letters "I-B-M" with individual Xenon atoms [22]. More recently, in 2008 the same group measured the force required to move a single cobalt atom over a smooth platinum surface [23].

### 1.3 Electric force microscopy

Electric force microscopy (EFM) is one of the techniques employed in the work presented in this thesis. EFM was first demonstrated in 1988 by Wickramasinghe *et al.* [24] and probes electrostatic forces arising from the attraction or

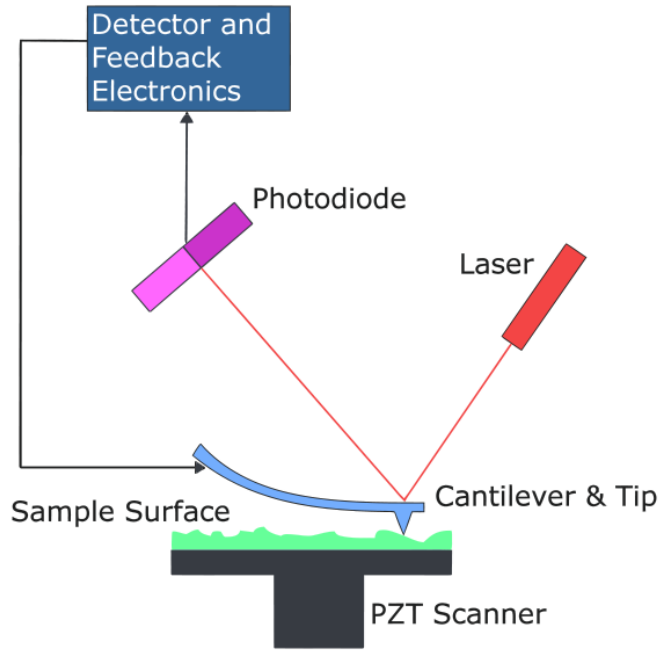


Figure 1.1: The atomic force microscope consists of a cantilever with a sharp tip, a photodiode to monitor the deflection of the cantilever in response to forces on the sample surface, and a piezo actuator to facilitate scanning. Image taken from the public domain.

repulsion between charge on the cantilever tip and charge on the sample and can be used to measure local capacitance and potential. Because electrostatic forces are long range, EFM images can be obtained at tip-sample separations as large as roughly 200 nm. This is a useful attribute of the technique because perturbations due to chemical and mechanical interactions are minimized [25] and because it facilitates access to interesting phenomena such as charge trapping [26]. Electric force microscopy (and its fraternal twin, Kelvin probe microscopy) has been used extensively to study organic semiconductors, including dopant distributions in electrochemically prepared films [27], energy level alignment [28], charge injection [29, 30, 31, 32], the development of the accumulation layer [33], charge transport [34, 29, 35], charge trapping [36, 37, 38, 39], and degradation [40] in films and working transistors. It has also been used

to measure the density of states in thin amorphous films [41], to study the motion of ions in light-emitting electrochemical cells [42, 43] and to image charge generation in photovoltaic films [44].

The observable in a classic AFM experiment is the cantilever's DC deflection in response to a force. In an EFM experiment, the observable quantity is a shift in the cantilever's resonance frequency originating from the Kelvin force [24]. The Kelvin force can be derived from the energy stored in a capacitor and is given by:

$$F_z = -\frac{1}{2} \frac{\partial C}{\partial z} \left( V_{ts} + \frac{\mu_t}{e} + \phi_s(x, y) \right)^2 \quad (1.1)$$

where  $C$  is the tip-sample capacitance,  $z$  is the tip-sample separation,  $V_{ts}$  is the applied tip-sample potential,  $\mu_t$  is the chemical potential of the tip, and  $\phi_s$  is the electrostatic potential in the sample directly below the tip. In deriving Eq. (1.1) it is assumed that the tip is vibrating in the  $z$  direction, that charge redistributes instantaneously between the tip and the sample during the cantilever oscillation in order to maintain the tip at a constant voltage, and that  $\phi_s(x, y)$  is independent of  $z$ . The contact potential difference is the difference between the work functions of the cantilever tip and the surface. Eq. (1.2) gives the shift in the cantilever's resonance frequency in response to an electrostatic force as a function of the applied tip-sample voltage,

$$\Delta f \approx f_c - \frac{f_c}{4k_c} \frac{\partial^2 C}{\partial z^2} \left( V_{ts} + \frac{\mu_t}{e} + \phi_s(x, y) \right)^2 \quad (1.2)$$

The contact potential difference may thus be defined as

$$\Delta\phi \equiv \frac{\mu_t}{e} + \phi_s(x, y) \quad (1.3)$$

where  $\Delta f$  is the frequency shift,  $k_c$  is the cantilever's spring constant and  $f_c$  is the cantilever's resonance frequency. The frequency shift  $\Delta f$  shift can originate either from the topography of the sample or from the surface potential.

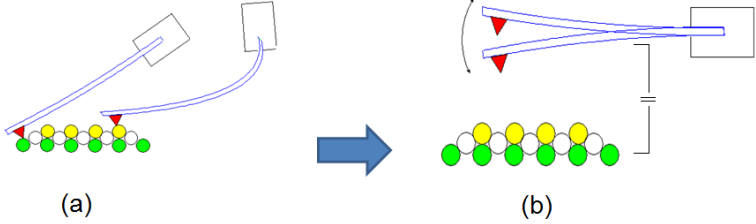


Figure 1.2: Cartoon of the contrast between the atomic force microscope (a) (shown here in contact mode to highlight the difference between the two techniques) and the electric force microscope (b). In electric force microscopy (b), a potential is applied between the tip and the sample.

## 1.4 Non-contact friction and frequency jitter

All experiments described herein rely on the assumption that a cantilever can be modeled as harmonic oscillator. In fact this is an extremely faithful approximation and is discussed at length in Appendix E. In principle, the behavior of a cantilever can be entirely described by the equation of motion for a harmonic oscillator,

$$m\ddot{x}(t) + \Gamma\dot{x}(t) + kx(t) = F(t), \quad (1.4)$$

where  $x(t)$  is the direction of the cantilever's motion,  $m$  is the mass of the cantilever,  $\Gamma$  is the intrinsic friction and  $F(t)$  is the force. The thermal fluctuations acting to damp the cantilever motion act as a stochastic force whose power spectral density is given by

$$P_F = 4k_B T \Gamma \quad (1.5)$$

The minimum detectable force is given by  $F_{\min} = (P_F b)^{1/2}$  where  $b$  is the detection bandwidth, the inverse of the averaging time.

The development of single-crystal ultra-sensitive cantilevers significantly reduced the cantilever's intrinsic friction, thus lowering the noise floor and facilitating the observation of quantities other than the static frequency shift. It is now possible to fabricate a cantilever with a damping parameter  $\Gamma$  lower

than the frictional drag exerted on the cantilever tip by, for instance, a sheet of epitaxial gold located about 100 nm away (assuming a tip charge of about  $10^{-18}$  C). Prior to the invention of ultra-sensitive cantilevers, the signal-to-noise ratio would have precluded such an experiment from taking place.

Ultra-sensitive cantilevers have also greatly improved the signal-to-noise ratio associated with measurements of the time-dependent fluctuation in the resonance frequency,  $\delta f_c$ ,

$$\delta f_c(t) = f_c(t) - \bar{f}_c, \quad (1.6)$$

where  $\bar{f}_c$  is the average resonance frequency. The square of this quantity is called “jitter” and is discussed at length in Chapter 3. Jitter has not been as widely studied as friction, but as we will show in this thesis, it can contain interesting information about the low-frequency atomic motions in thin-film materials. Jitter and friction are the primary observables utilized for the experiments described in this thesis.

## 1.5 Summary and outline of the thesis

AFM is now a standard technique for the characterization of surface topography. Ultra-sensitive force detection has shown great promise but still has not developed into a “workhorse” technique. In large part, this is because the interpretation of these experiments can be very complicated.

The experiments of Rugar and co-workers [12, 11, 3] and many others have served to refine the techniques of atomic force microscopy in environments engineered to test the limits of force detection. Over the past few years, our group has sought to apply these techniques and others to measure microscopic forces

in real systems. Israeloff and co-workers [20, 45, 46] have measured frequency noise over thin polymer films, and in 2006, Kuehn *et al.* [13] presented the first measurements of non-contact friction in an organic system. Here we present the first ultra-sensitive measurements of frequency jitter in an organic system, and provide a clear interpretation of our results. Briefly, we have been able to show that cantilever frequency jitter can be a direct probe of stochastic electric field gradients arising from thermal dielectric fluctuations in thin polymer films.

The outline of the thesis is as follows. Chapter 1 is a brief introduction to the concepts of scanned probe microscopy. Chapter 2 describes our custom-built scanned probe microscope, measurement protocols and also contains details of the cantilever fabrication process. Chapter 3 is a presentation of a theory which allows us to predict cantilever frequency jitter from a polymer's dielectric function and thickness and the cantilever tip's height and radius, each of which may be measured independently. Experimental evidence for this theory is provided in Chapter 4, which contains the bulk of the work completed by the author. In Chapter 5, we present our preliminary efforts toward applying the techniques of Chapter 4 to an even more interesting system – an organic semiconductor. Organic semiconductors are promising materials for display technology, but the microscopic origins of their charge transport properties are not well-understood.

## CHAPTER 2

### APPARATUS

#### 2.1 Summary

All experiments were conducted using a custom-built scanning probe microscope. The fundamental elements of the microscope are:

- (a) a cantilever for mechanical force detection (Section 2.11 and in greater detail in Appendix B),
- (b) an interferometer for monitoring the cantilever's displacement (Section 2.9),
- (c) a means of inducing the cantilever to oscillate (Section 2.13),
- (d) a means of manipulating the lateral position of the sample relative to the cantilever (Section 2.4)
- (e) a means of adjusting the separation between the cantilever and the sample (Section 2.3), and
- (e) a means of isolating the microscope from ambient vibrations (Section 2.8).

The microscope was originally designed by Seppe Kuehn, a former graduate student at Cornell, to facilitate rapid exchange of samples in a room-temperature, high-vacuum environment isolated from ambient vibrations. For the experiments contained in Chapter 4, the only modification we made was to change the model and orientation of the vertical positioner. The microscope was significantly altered for the experiments of Chapter 5, which required greater lateral scanning capabilities than afforded by the original design.

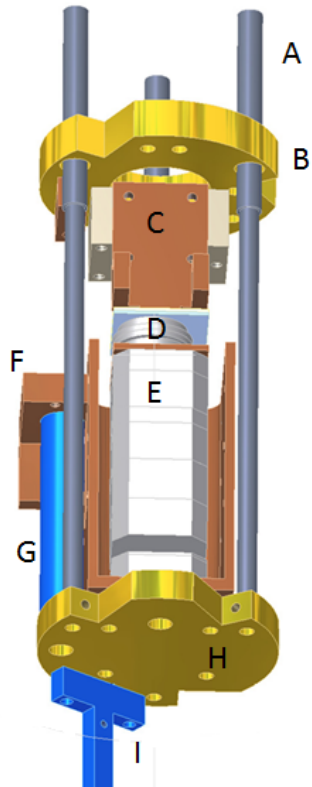


Figure 2.1: Rendering of the microscope. The brass rings (**B** and **H**) hold the microscope components and provide structural stability. The rings are threaded onto stainless steel rods (**A**) and secured with set screws. The sample holder (**D**) is connected to the Attocube piezo stack (models ANPz-51, ANPx-50, ANPx-51 and ANSxy-50) (**E**) with a double stack of sapphire plates mounted on magnets. The entire structure is fastened to a flexible bellows, which in turn is connected to the vacuum line. The delicate piezo stack is encased in a protective aluminum box (**F**). The cantilever is mounted to an aluminum piece (**C**) that also holds the optical fiber and the drive piezo. The wires are threaded through the bellows down the microscope through a rubber tube (**G**) to a Delrin piece (**I**) that holds a pin connector.

## 2.2 Microscope super-structure

CAD drawings of the microscope's super-structure and many other useful details are available in Ref. [47] and in Appendix A. The vacuum line and vibration isolation are identical to those described by Kuehn in Ref. [47].

The microscope components are mounted onto three brass discs stacked on stainless steel rods. The brass discs are secured to the stainless steels rods with 2-56 stainless steel set screws. The top brass disc holds the electrical connections, which terminate in a 19-pin connector. The electrical connections run from the uppermost brass ring down to the underside of the lowest brass ring through a shrink-wrap tube and are soldered directly to a 2 cm long 16-pin connector. The pin connector attaches to the lowest brass ring via an adaptor piece machined from Delrin (a Dupont trademark for polyoxymethylene, a wear-resistant thermoplastic) to provide electrical insulation. Where possible, we soldered the ground pins to each other to avert the formation of ground loops.

The second disc holds the cantilever and the lowest disc holds the lateral positioning hardware. The entire structure is connected to soft edge welded bellows to isolate the experiment from vibrations.

Stops were carved into the steel rods to ensure that the lowest brass disc (which holds the lateral positioning hardware) cannot move beyond a precisely machined set point. These stops serve both to protect the cantilever from uncontrolled contact with the surface and to maintain perpendicularity. The microscope was designed to ensure that distance between the tip and the sample remained as stable as possible. The coarse-approach fiber mount is machined

from aluminum and is attached to the same brass piece as the cantilever mount. The coarse approach fiber points directly at the sample mount, so as to account for any fluctuation in the tip-sample distance resulting from thermal expansion. All experiments were conducted at room temperature in an environment where the ambient fluctuations are minimal, so materials were not chosen to match thermal expansion coefficients.

### 2.3 Vertical positioning

The separation between the tip of the cantilever and the surface of the sample can be roughly adjusted between 0 and 2 mm, and reliably varied between 2 and 5000 nm. The tip-sample separation is regulated by affixing the sample to a commercial nanopositioner, the ANPz-51 (manufactured by Attocube Systems AG). The ANPz-51 replaced the ANPx-50, which was employed as a vertical positioner in the original probe and was occasionally prone to “jump” when left at rest for long periods of time. Unlike the ANPx-50, the ANPx-51 is designed specifically for use in the vertical geometry. Attocube positioners employ piezocrystals (which rely on the converse piezoelectric effect, where the application of an electric field creates mechanical deformation in the crystal) to achieve controllable nanometer-scale motion. The piezocrystal itself is manufactured by PZT ceramics. The motor consists of three parts: a “mover”, an actuator (piezo crystal) and an inertial weight.

There are two modes of approach. “Coarse” positioning (see Fig. 2.2) is suitable for long-range, rough positioning and is achieved by sending regular sawtooth voltage pulses to the actuator. Coarse positioning operates on the “slip-

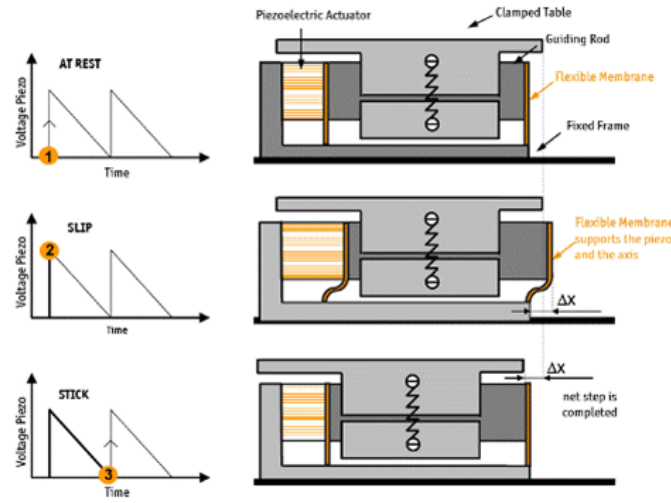


Figure 2.2: The nanopositioner operates on the “slip-stick” principle of inertial motion and is based on the controlled movement of a sliding block. The block experiences friction as it slides along a rod. To step, the rod is first accelerated rapidly over a short time period so that the inertia of the sliding block overcomes the friction. The block disengages from the accelerated rod and remains at rest. The rod moves back to its initial position slowly enough so that the sliding block sticks to it and takes a step. The rod is pushed and pulled by a piezoceramic crystal. Figure is reproduced from the Attocube User Manual, Copyright 2005 Attocube Systems AG.

“stick” principle: when a voltage is applied to the actuator, it rapidly contracts or expands. This generates a strong inertial force which induces the mover to move against static friction. When the voltage is ramped down, the actuator slowly retracts, but the static friction of the mover exceeds the inertial force and it does not return to its initial position. “Fine” motion is the preferred method for short-range, accurate positioning and is achieved by simply applying a DC voltage to the piezocrystal.

Table 2.1: Specifications for the Attocube positioners. The nm/V for coarse positioning is given for 15 V steps in the absence of a load. Both the coarse and the fine positioning calibrations were measured in our laboratory using a bench-top interferometer. The Attocube manual advises that the step sizes can change depending on the size of the load. The maximum load, fine range and coarse range parameters were obtained from the Attocube manual.

Model	nm/V (coarse)	nm/V (fine)	Max Load (grams)	Fine range ( $\mu\text{m}$ )	Coarse range (mm)
ANPz-51	108	50	50	5	2.5
ANPx-51	110	40	25	5	3
ANPx-50	31	130	25	5	4
ANSxy-50	n/a	330	50	20	n/a

## 2.4 Lateral positioning

The piezo tube scanner employed in the original dissipation microscope possessed a fine scan span of 20  $\mu\text{m}$ , but was not designed to facilitate reliable coarse motion. It was adequate for relatively homogeneous polymer films of the type studied in Chapter 4 of this thesis. However, it was not suitable for systems where there is significant topographical inhomogeneity. The organic field effect transistors described in Chapter 5 of this thesis typically consisted of arrays of 50 interdigitated electrodes of width 15  $\mu\text{m}$  spaced about 5  $\mu\text{m}$  apart.

In order to improve the scan range of the microscope, the piezo tube was replaced with three commercial nanopositioners, also purchased from Attocube Systems AG. All positioners were calibrated in our laboratory using a bench-top interferometer and the results, along with key manufacturer's specifications, are provided in Table 2.1. Whereas the new ANPx-51 and ANSxy-50 models evinced clear, highly reproducible interference patterns, the performance of the ANPx-50 significantly degraded over a six year period.

To achieve coarse lateral motion, we used the ANPx-50 (carried forward from the previous incarnation of the microscope) in conjunction with the ANPx-51 (a newer and considerably more robust version of the ANPx-50). For fine motion, we used the ANSxy-50. The maximum load of each positioner is different and they are stacked accordingly; the ANPx-50 sits at the very top because it is the most fragile. It was necessary to disassemble the ANSxy-50 to incorporate it into the stack.

In general, piezo tubes are prone to non-linear behaviour; displacement may not scale linearly with applied voltage, scans are not exactly planar, and errors tend to increase with scan range [48]. The Attocube positioners do not appear to be as susceptible to these errors. The two main disadvantages of the Attocube positioners are their extreme fragility and their price. The latter is beyond our control; our attempts to mitigate the former are described in 2.6.

## 2.5 Voltage sources

The high voltages and high currents required by the piezo actuators were supplied by the ANC 150, a voltage controller also manufactured by Attocube Systems AG. The ANC 150 can supply frequencies from 1 Hz - 8 kHz and voltages of up to 70V. The manufacturers do not recommended application of more than 20 V to any of the positioners because it may result in de-polarization of the piezo. The most reliable indicator of the positioner's performance is its capacitance. We have found that even a slight decline in the capacitance usually indicates a problem with the quality of the electrical connections. To facilitate fine motion, we supplied an external voltage to the ANC 150 from a National Instru-

ments DAQ BNC-2090 board connected to a low-noise amplifier manufactured by Piezomechanik GmbH (Model SVR 350-3-bip).

The ANC 150 unit's sole means of communicating with a computer is an RS-232 port. RS-232 technology is nearly obsolete, and it was impractical to purchase a computer with RS-232 capabilities. To remedy the problem, we bought a RS-232 to USB (Universal Serial Bus) converter cable (BAFO, Model BF-810). Unfortunately, our instrument control software (LabView 8.0, by National Instruments) does not interface smoothly with serial ports (specifically, there is no status byte for serial communication in LabView). The software driver provided by Attocube AG (ANC150\_communication.vi) will not function with a RS-232 to USB converter cable unless the LabView code is modified so that it correctly monitors the bytes at port. We wrote software to address this problem. The software sends a system request to the ANC 150 controller, and then "waits" for the controller to indicate that the command has been processed. This indication takes the form of an ASCII string  $n$  bytes in length; we instruct the software to loop so that it queries the software for the bytes received at port. The software exits the loop when it detects that  $n$  bytes have been received at port. It is important to note that one cannot simply set a large "timeout value" at the port (i.e. instruct the software to proceed after a certain length of time has elapsed) because the information at port has an indeterminate half-life. A directory of commands to the controller is located in the Attocube manual.

The ANC 150 is also quite sensitive to static charge. We found that the unit was prone to automatically power cycling when touched without a grounding strap. We also found that applying a simple low-pass RC filter centered at 200 Hz to the ANPz-51 whilst taking measurements tends to reduce cantilever



Figure 2.3: Microscope with a sample mounted. The Attocubes sit inside the aluminum box. Electrical connections are gathered at the bottom for ease of access. The entire structure is suspended from a 5" flexible bellows, which is fastened to an HV ISO 5.118" OD Flange. A 19-pin connector is welded to the flange. The bellows, flange and 19-pin connector are not pictured. A full description of these parts can be found in Ref. [47].

frequency noise.

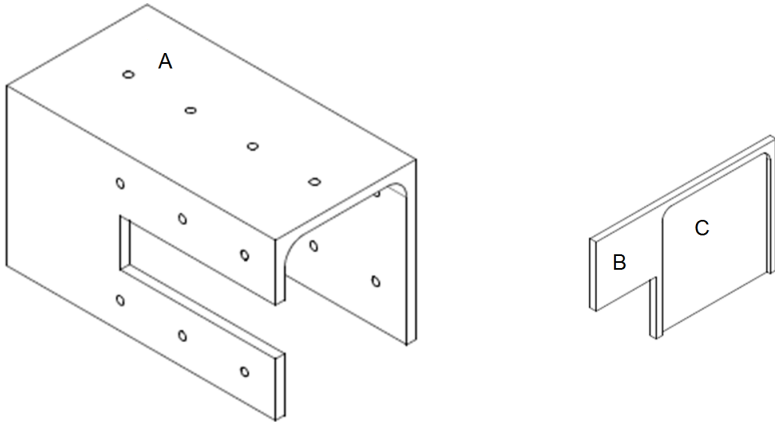


Figure 2.4: Renderings of the protective box for the nano-positioners (A) and the sample holder (B and C). The CAD drawings for these parts and others, along with all relevant dimensions, are contained in Appendix A.

## 2.6 Protective box for piezo stack

The Attocubes, particularly the now obsolete ANPx-50 model, are extremely fragile, so it was necessary to design an enclosure to protect them (refer to Figure 2.4, part A). Some research groups have machined similar boxes from titanium, which has a high thermal conductivity that makes it a good candidate for low-temperature experiments. Our experiments do not require cryogenic temperatures, so we used aluminum (60/61 alloy). The box has three walls, one of which has a wide slit in the middle to accommodate protruding twisted-pair wires. The piezo stack is fastened to the protective box with two countersunk M2 screws that attach to the ANPz-51, and the box itself is affixed to a 5 mm thick brass plate with four 2-56 screws. The lowest brass plate was cut 5 mm thick instead of 2.5 mm thick like its counterparts to increase the mass of the base. It was necessary to increase the base mass because the Attocubes require an inertial counter-weight of at least 50 grams to function properly.

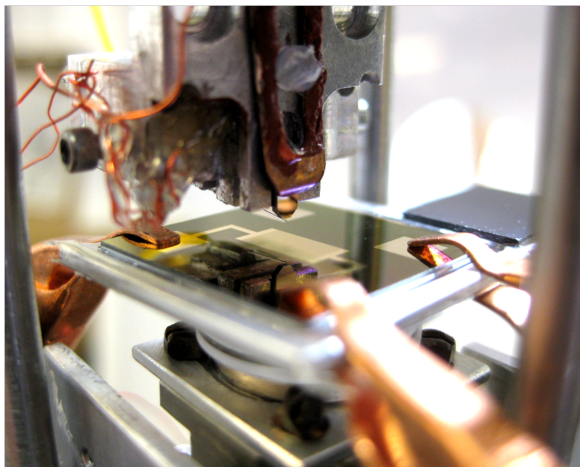


Figure 2.5: Close-up of sample mount. The cantilever is positioned directly over an interdigitated field-effect transistor device. The optical fiber is clearly visible directly below the cantilever die.

## 2.7 Sample holder and cantilever holder

The sample holder is an L-shaped sheet of aluminum with a recessed  $4\text{ cm}^2$  cavity (see Figure 2.4, part **C**). A reflective piece of silicon is superglued to the “arm” of the L-shape (part **B**). A fiber-optic cable is threaded through an aluminum tube (Small Parts, #CTSXX-6220-12) 1.5 mm in diameter and points squarely at the silicon piece to allow the motion of the ANPz-51 relative to the brass ring holding the cantilever to be monitored via interferometry. The aluminum tube is secured to the microscope with a set screw through an aluminum adaptor piece attached to a brass ring which also supports the cantilever holder. In order to minimize the shear force applied to the Attocube piezo crystal, we attached the sample holder to the piezo stack with NdFeB magnets (K&J Magnetics, Model DX01). A piece of sapphire was super-glued to a magnet, which was itself super-glued to a thin sheet of aluminum. The aluminum piece was attached to the Attocube with four 2-56 screws. A second sapphire piece/magnet was glued to the aluminum sample holder. We found that this configuration

firmly secured the sample holder to the microscope, but allowed us to remove samples without subjecting the piezo stack to excessive force. We insulated the sample holder with a layer of 0.2 mm thick clear packing Scotch tape. Electrical connections to the sample electrodes were made with copper clips (Mueller Electric Company; Model 34C).

The cantilever holder is machined from aluminum. The cantilever sits in a  $3\text{ mm}^2$  groove and is secured to the microscope with a CuBe clip that fastens to the body of the holder with a 1-64 plastic screw. The CuBe clip also supplies a voltage to the cantilever tip. To electrically insulate the clip from the body of the aluminum piece, we coated all but the very tip of the clip in an insulating varnish. We placed a small dot of silver paint at the interface between clip and cantilever base to ensure that the cantilever and the clip were in electrical contact. When the probe is fully assembled and the z-positioner fully retracted, the distance between the cantilever tip and the sample surface is only 2 mm. To minimize the probability of accidental tip-sample contact during assembly, we designed a “sliding” adaptor piece for the cantilever holder so that it can be moved smoothly in and out of the microscope like a desk drawer (see Figure A.5). The stationary base of the slider is secured to the uppermost brass ring with two 1-64 screws. The adaptor piece fastens to the cantilever holder with two 2-56 screws and can be firmly attached to the stationary base with a 1-56 screw.

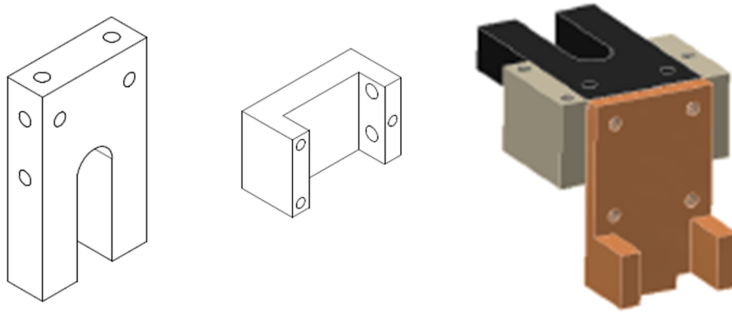


Figure 2.6: Renderings of the sliding “drawer” for moving the cantilever holder in and out of the microscope (left and center). The fully assembled piece is shown on the right, with the sliding “drawer” pieces colored gray and black and the cantilever holder colored brown.

## 2.8 Vibration isolation and vacuum

All experiments were conducted at  $10^{-6}$  mbar using a turbomolecular pump with a rotary vane backing pump (Pfeiffer; model no. DUO 2.5). Ambient vibrations from both the building and from the turbomolecular pump were of great concern, so two levels of vibration isolation were employed in the apparatus. The sample/cantilever stage was suspended from custom soft edge-welded bellows (BellowTech; loaded resonance frequency 5 Hz). The entire vacuum chamber was mounted on a commercial vibration-isolation table (Minus-k technologies, model 250BM-3; loaded mechanical resonance frequencies of 0.6 Hz (lateral) and 0.7 Hz (vertical)). An additional set of bellows was used to mechanically isolate the pumplines from the chamber (BellowTech).

## 2.9 Interferometer

Cantilever displacement was detected via interferometry, which enables quantitative evaluation of small displacements. The basic operation of the interferometer is described below. A laser beam propagates through a flexible optical fiber and into a 90:10 fiber-optic directional coupler (Ipitek, Model LA 26-03).

The light travels through the 10% arm of the coupler to the cleaved end of the fiber, where a small fraction of the initial power is reflected from the surface of the cleaved edge and travels back through the fiber. The remainder of the light is reflected by the cantilever “pad”. The space between the cleaved end of the fiber and the cantilever pad constitutes a Fabry-Perot cavity, where the reflected light forms a standing wave. Incident power on the cantilever is typically  $9 \mu\text{W}$ .

Reflected light from the cantilever pad travels back down the directional coupler’s 90% arm and converted to a voltage using a commercial photodetector (New Focus; model no. 2011 photodiode; gain = 104, high-pass cutoff frequency 300 Hz, low-pass cutoff frequency 30kHz).

The light source for the interferometer was a diode laser operating at a wavelength of  $\lambda = 1310 \text{ nm}$  (Laser Diode Incorporated; model no. LD-27492). The laser was driven using a precision current source (ILX Lightwave; model no. LDX-3620) delivering 16 to 28 mA. In order to set the interferometer at its sensitive point, the laser wavelength was adjusted by affixing the laser to a thermoelectric cooler (ILX Lightwave; model no. LDM-4980 Laser Diode Mount), the temperature of which was adjusted to between  $0^\circ\text{C}$  and  $40^\circ\text{C}$  using a temperature controller (ILX Lightwave; model no. LDT-5910B). A typical operating distance between the cantilever and the fiber was roughly 2 microns.

To mitigate the effect of laser mode hopping (which severely degrades the interferometer noise floor), a 5.0 dBm 250 MHz current (Hewlett Packard; model no. 8657A Signal Generator) was added to the laser's DC current using a bias tee (Minicircuits; model no. 2F BI-4R2G). To calibrate the interferometer, the cantilever was driven to a peak-to-peak amplitude larger than  $\lambda/4$  and the minimum and maximum output voltages were observed (typical values  $V_{\min}=2.5$  V to  $V_{\max} = 4.5$  V). The interferometer sensitivity was calculated from  $S = \lambda/(2\pi(V_{\max} - V_{\min}))$ . A typical  $S$  was 104 nm/V. The fringe depth of the interferometer signal was typically ranged from 2-6 V. The interferometer set-up is common to all of the scanned probe microscopes in the laboratory and is described in greater detail in Ref. [49].

## 2.10 Cantilever design

Cantilevers were designed to maximize their sensitivity to extremely small changes in resonance frequency. The minimum detectable frequency shift has been derived by Obukhov *et al.* [50] and is given by

$$\langle(\delta f_c)^2\rangle_{\min} = \frac{k_B T b f_c^2 \Gamma}{x_{\text{rms}}^2 k_c^2}, \quad (2.1)$$

where  $k_B$  is Boltzmann's constant,  $T$  is the temperature,  $b$  is the bandwidth of the measurement,  $x_{\text{rms}}$  is the amplitude of oscillation,  $k_c$  is the spring constant and  $\Gamma$  is the intrinsic friction. The quality factor  $Q$  describes the cantilever's response to a driving force at its resonance frequency. The higher the  $Q$ , the narrow the width of the response peak (see Figure 2.7). According to Eq. (4.3), highest sensitivity is achieved when when  $\Gamma$  is as small as possible. An expression for  $\Gamma$  in terms of cantilever geometry was derived by Stowe *et al.* [51] and was used a

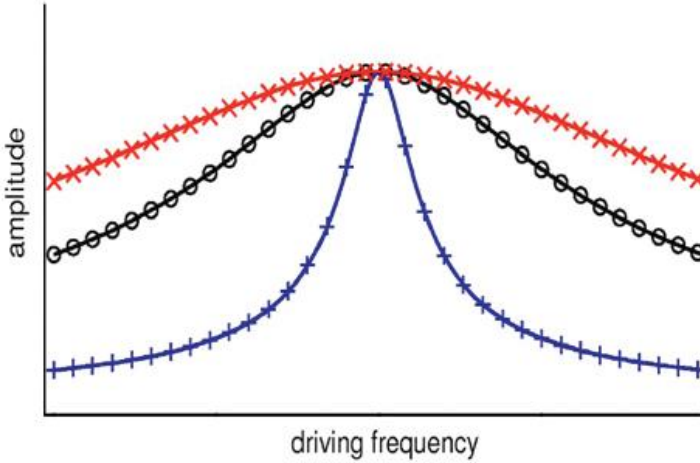


Figure 2.7: The quality factor  $Q$  is the quality of the cantilever's response at its resonance frequency. Here we depict data for fictional cantilevers with a high  $Q$  (blue lines), medium  $Q$  (blue circles) and low  $Q$  (red crosses). All three peaks are centered at the same resonance frequency.

guide for cantilever design:

$$\Gamma = 0.29 \frac{wt^2}{l} \frac{12\sqrt{\rho E}}{Q}, \quad (2.2)$$

where  $w$  is the width of the cantilever,  $l$  is its length,  $t$  is its thickness,  $\rho$  is the density of silicon ( $2330 \text{ kg/m}^3$ ),  $E$  is Young's modulus (150GPa) and  $Q$  is the cantilever's quality factor. Eq. (2.2) suggests that  $\Gamma$  is minimized when the cantilever is as thin, narrow and long. Long cantilevers are also beneficial because it is known [52] that short cantilevers, which are more susceptible to support loss and surface loss through the native oxide layer, tend to have lower quality factors.

For a typical commercial EFM cantilever with  $f= 1 \text{ kHz}$ ,  $k=1 \text{ N/m}$ ,  $Q=1000$ ,  $l=290 \mu\text{m}$ ,  $w=40 \text{ nm}$  and  $t=2 \mu\text{m}$ ,  $\Gamma$  is on the order of  $10^{-9} \text{ kg/s}$ . Rugar *et al.* [53, 3] and Marohn *et al.* [7] have fabricated single crystal silicon with non-contact friction coefficients as low as  $10^{-13} \text{ kg/s}$ . Recently, Budakian *et al.* [54] have fabricated cantilevers from silicon nanowires with non-contact friction coefficients as low as  $10^{-15} \text{ kg/s}$ . The cantilevers are batch-fabricated from single-crystal

silicon and are extremely thin ( $0.1\text{ }\mu\text{m}$ ). The fabrication process was modified from a protocol described by Kuehn in Ref. [47], which itself was adapted from Ref. [51]. The process is described in the following section and in Appendix B.

## 2.11 Cantilever fabrication

This section is a condensed account of the fabrication process. All details of the process are contained in Appendix B. We fabricated our cantilevers at the Cornell Nanoscale and Technology Facility (CNF) and a schematic of the process is shown in Figure 2.8. The starting material is a silicon-on-insulator (SOI) wafer purchased from Soitech. Figure 2.8 shows the architecture of these wafers: 400 nm of thermally grown  $\text{SiO}_2$  sandwiched between 450  $\mu\text{m}$  of 100 n-type polished silicon and 340 nm of 100 n-type silicon. The resistivity of the silicon layer was  $1\text{-}50\Omega\text{ cm}$ . In theory, it is possible to fabricate silicon-on-insulator wafers *de novo*. However, the CNF does not currently possess the technology to grow single crystal silicon wafers of comparable quality to those produced by Soitech. The quality of the silicon crystal has a direct bearing on the quality factor of the cantilever.

As discussed in the previous section, cantilevers that are long, narrow and thin provide the best sensitivity to frequency noise. To facilitate greater sensitivity,  $200 \pm 20\text{ nm}$  deep pits were etched into the top 340 nm silicon layer (see Figure 2.8(a)). Etching deeper than 240 nm usually renders the tips too weak to withstand processing.

Figure 2.8(a)-(e) is a schematic of the wafer's top-side processing. In step (b), the cantilevers are defined in a layer of photoresist, which serves as a mask

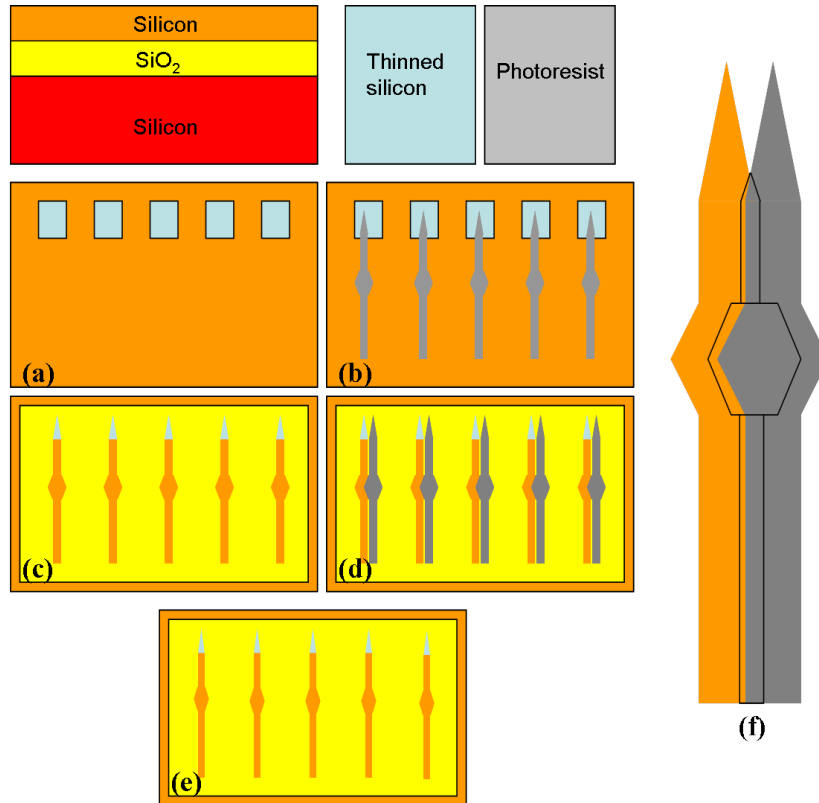


Figure 2.8: Cantilever fabrication process. Generally, the smallest features that can readily be defined via photolithography are on the order of about 1 micron. Here we are able to use photolithography to fabricate cantilevers with tips as small as 100 nm in diameter. The cantilevers are defined in the intersection between two photolithographically defined layers (f). Note that the offset in (f) is exaggerated for visualization purposes. In reality, the two cantilever layers lie nearly on top of each other.

for the etch step depicted in (c), where the wafer is subjected to a reactive ion etch. The reactive ion etch removes the entire silicon layer except for the parts that have been “masked” by photoresist. In step (d), the photoresist definition is repeated, with the cantilevers offset by 0.025 mm), and a second reactive ion etch removes all unmasked silicon. After the photoresist is removed, what remains is the intersection of the two sets of defined cantilevers (see step (f)). This process can produce cantilever tips as small as 100 nm. As indicated by Figure 2.8, at this stage, the wafer consists of cantilevers embedded in a 400 nm layer of

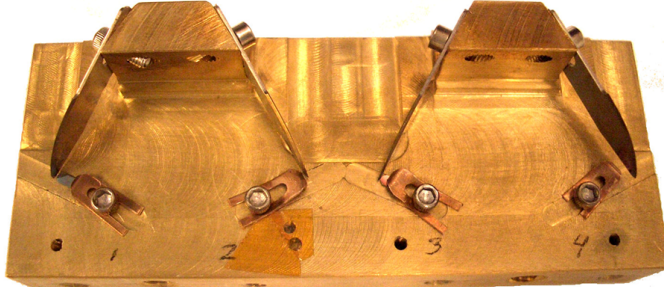


Figure 2.9: Custom-machined brass rig for evaporating metal onto the cantilever tips. The rig is described in greater detail in Ref. [47].

$\text{SiO}_2$ , which is itself embedded in 450  $\mu\text{m}$  of polished p-type silicon. To enable handling of the wafers, rectangular 2x3 mm dies are defined in the handle wafer using a backside exposure process. The remainder of the process is devoted to removing the excess material. A protective 2  $\mu\text{m}$  layer of  $\text{SiO}_2$  is deposited onto the front side of the wafer using a plasma-enhanced chemical vapour deposition process. The excess silicon via a Botsch etch, and the  $\text{SiO}_2$  is carefully removed via a liquid HF etch. The cantilevers are removed from solvent using a critical point dryer. The finished cantilevers are typically 275  $\mu\text{m}$  in length, 6  $\mu\text{m}$  in width, and 340 nm thick; the tips of the cantilevers are triangular prismatic in shape. We coat the cantilever tips with 15 nm of platinum by “masking” the cantilever from the reflective pad to the base with a razor blade mounted on top of a custom machined brass rig (see Figure 2.9). The cantilevers are secured to the rig using a CuBe clip and a 2-56 screw. Scanning electron micrographs of the finished cantilevers are shown in Figure 2.10. The cantilever fabrication scheme is very sensitive to processing conditions. Even small errors can destroy the final product; Figure 2.11 shows scanning electron micrographs of some of the most common processing failures. We found that in roughly 10% of cases, after 12 hours in vacuum, platinum-coated cantilevers experienced a decline in Q of roughly two orders of magnitude. The cause of this decline is unknown.

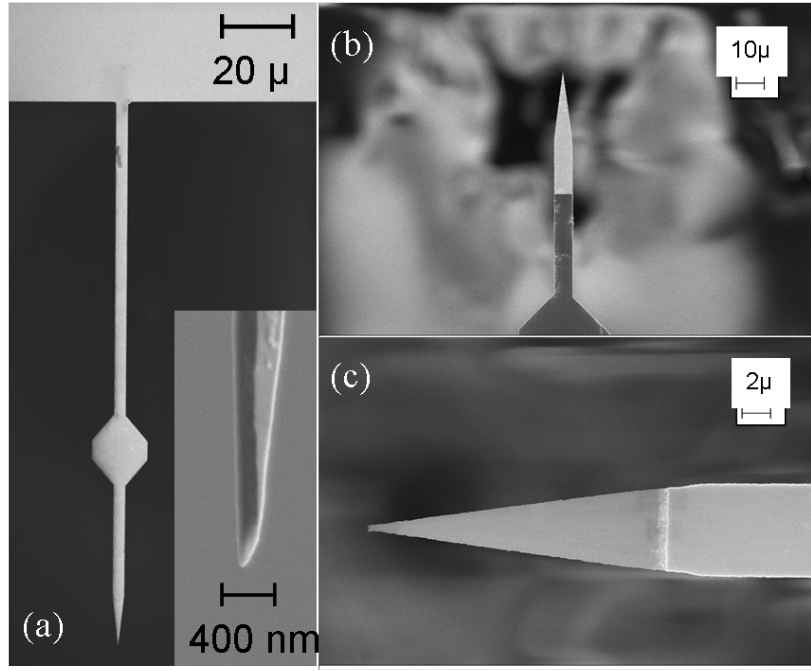


Figure 2.10: Cantilever glamor shots. Scanning electron micrographs of (a) the cantilever attached to the die. Inset: The diameter of the cantilever tip can be as small as 100 nm. (b) A 15 nm thick layer of platinum has been deposited in the light-colored region. (c) The silicon in the triangular tip region has been thinned to about 120 nm. The thickness of the rectangular region is 340 nm.

## 2.12 Measurement protocols

There are two observables in this experiment. The first is the cantilever damping parameter  $\Gamma$ , defined in Chapter 1 and discussed in Appendix E. We measure  $\Gamma$  by driving the cantilever at a set amplitude  $A$ , then abruptly terminating the drive signal, allowing the cantilever to “ring down” to equilibrium. The “ringdown time” is defined as the time required for the cantilever’s oscillation amplitude to reach an amplitude of  $A/e$ . The ringdown time  $\tau$  is related to the cantilever’s intrinsic friction parameter  $\Gamma$ ,

$$\Gamma = \frac{k}{2\pi^2 f_0^2 \tau}, \quad (2.3)$$

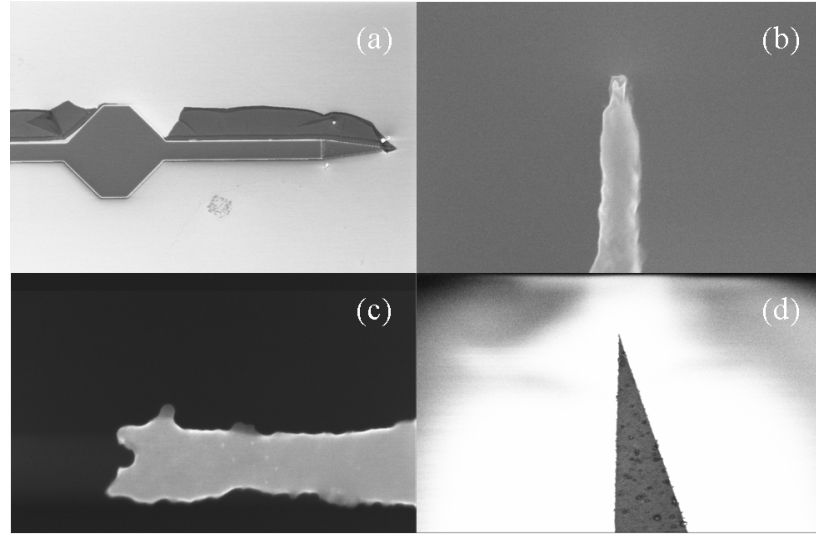


Figure 2.11: Some of the most common failures of the cantilever fabrication process: (a) failure to completely remove the  $\text{SiO}_2$  during the HF etch resulted in superfluous material clinging to the cantilever, (b) over-etching during the cantilever definition steps rendered the cantilever tip too weak to withstand processing, so it fell off, (c) failure to completely remove the silicon during the cantilever definition etch steps resulted in a “two-headed” cantilever and (d) the cantilever acquired a layer of dirt after prolonged use in the scanned probe microscope.

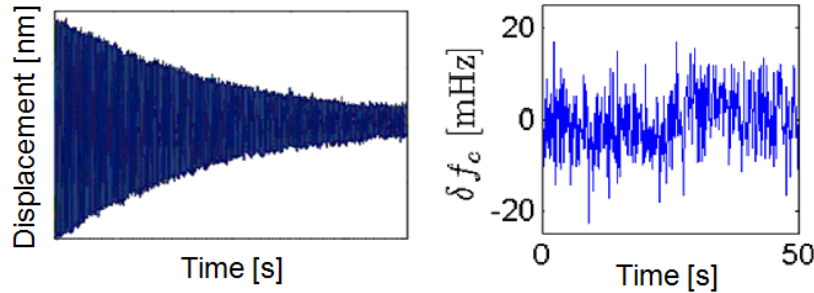


Figure 2.12: Left: Simplified picture of a ringdown. At  $t = 0$ , the driving force to the cantilever is abruptly terminated and the cantilever is allowed to “ring down” to equilibrium. Right: Jitter is the time-random fluctuation in the cantilever resonance frequency.

where  $Q$  is the cantilever’s quality factor and  $f_c$  is the resonance frequency. Jitter,  $\langle \delta f_c \rangle^2$ , is conceptually simpler. The time-dependent frequency shift  $\delta f_c(t)$  is sim-

ply the noise in the cantilever's resonance frequency and is defined as follows,

$$\delta f_c(t) = f_c(t) - \bar{f}_c, \quad (2.4)$$

where  $f_c(t)$  is the time-dependent frequency of the cantilever and  $\bar{f}_c$  is the mean frequency. Jitter is a separate entity from the static frequency shift  $\Delta f$ .

## 2.13 Drive circuit

When a cantilever circuit is connected to an outside power source, the oscillation is said to be "driven". The cantilever was driven via a self-oscillation circuit.

In our system, which was designed by Dr. SangGap Lee, the cantilever signal is sent through a bandpass filter centered roughly within 100 Hz of the cantilever's resonance frequency. The  $Q$  of the filter is 0.625. The signal is then phase-shifted by -90 degrees; this is critical to the operation of the circuit because it is the effect of the lag in the drive signal's phase shift that induces the cantilever to oscillate on resonance. The cantilever drive signal was fed to a 2x4 mm bimorph piezocrystal (Piezo Systems) that was mounted underneath the cantilever. One side of the bimorph piezo was electrically isolated from the rest of the probe. The -90 degree phase-shifted signal was converted to a 5 V peak-to-peak square wave. The square wave was multiplied by a set DC voltage supplied by a DAC Board (National Instruments, Model BNC-2090) until the cantilever reached a full-fringe amplitude. It was then sent through a band pass ( $Q=2.5$ ) filter centered at the cantilever's resonance frequency. The key features of the circuit are its flat-gain wide-phase accessible phase shifter and its automatic gain controller (consisting of a voltage comparator followed by a band pass filter). The circuit usually operated in constant drive amplitude

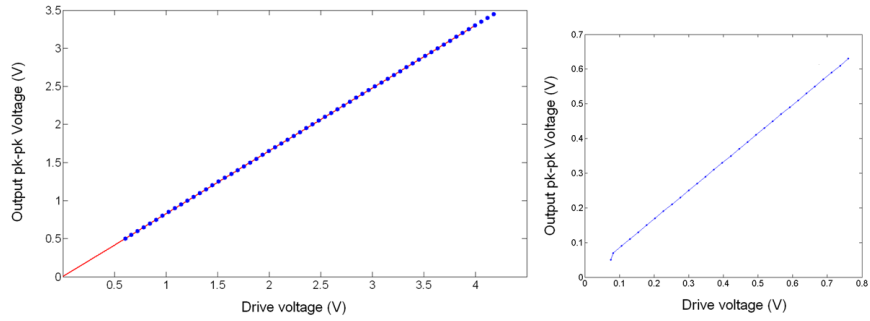


Figure 2.13: We found that the peak-to-peak output of the circuit (blue circles) was linear in applied voltage. Left: The input was a test sine wave with a peak to peak amplitude of 0.56 V and a frequency of 4600 Hz (chosen to emulate a typical cantilever resonance frequency). The red line ( $y = 0.82x + 0.0035$ ) is a best fit to the data. Right: close-up of the region from 0.1-0.8 V.

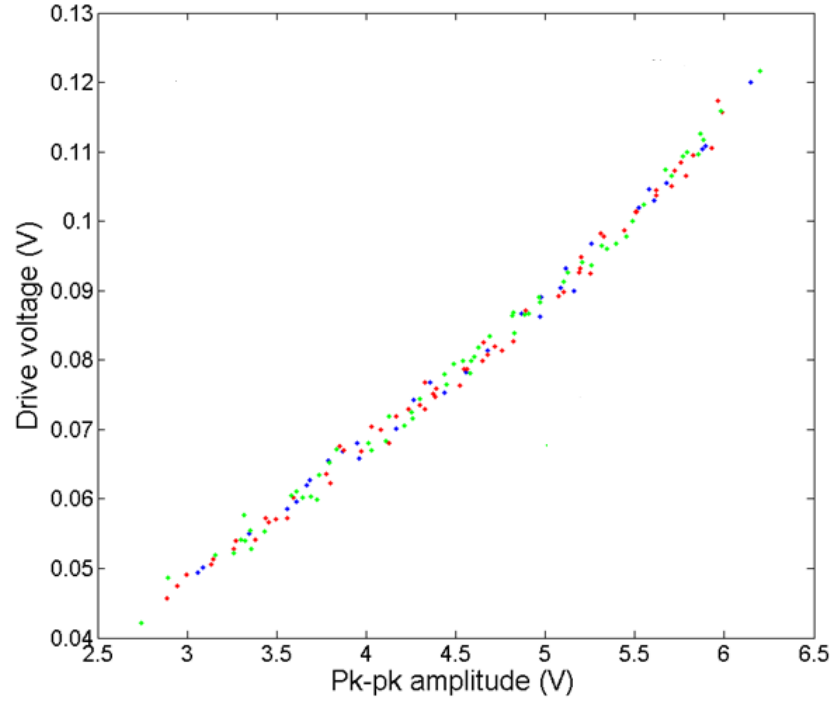


Figure 2.14: We measured the response of the cantilever's amplitude to the drive voltage at tip-sample separations of 450 nm (blue dots), 145 nm (red dots) and 20 nm (green dots). We found that the response is linear.

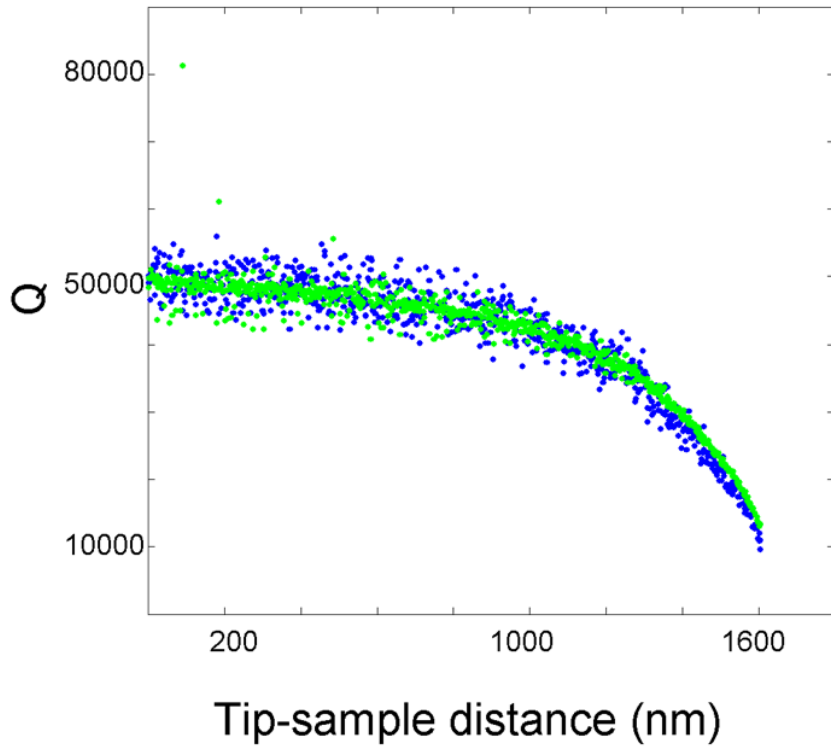


Figure 2.15:  $Q$  measured over 280 nm PMMA via the “ringdown” method (blue dots) and via a scaled measurement of the output voltage to the drive piezo (green dots). The surface is defined as the location at which  $Q$  extrapolates to zero. Here the surface is at 1730 nm. The cantilever’s spring constant is 0.0007 N/m and the frequency was 7 KHz; the allotted time for the piezo voltage to “settle” was 5 seconds.

mode. It was possible to maintain constant oscillation amplitude by adjusting the set DC voltage via a PID loop. The PID was implemented in software using a program supplied by National Instruments.

To ensure that the feedback electronics did not make an appreciable contribution to the frequency noise, we systematically tested the response of the circuit to the DC set voltage (drive voltage). As shown in Figure 2.13, we found that the magnitude of the output signal generated by the circuit was linear in the input for voltages ranging from 0.1 to 8 Volts. We also tested the response of the output amplitude of an actual cantilever signal to the drive voltage (see Figure 2.14). We found that for three different tip-sample separations, the can-

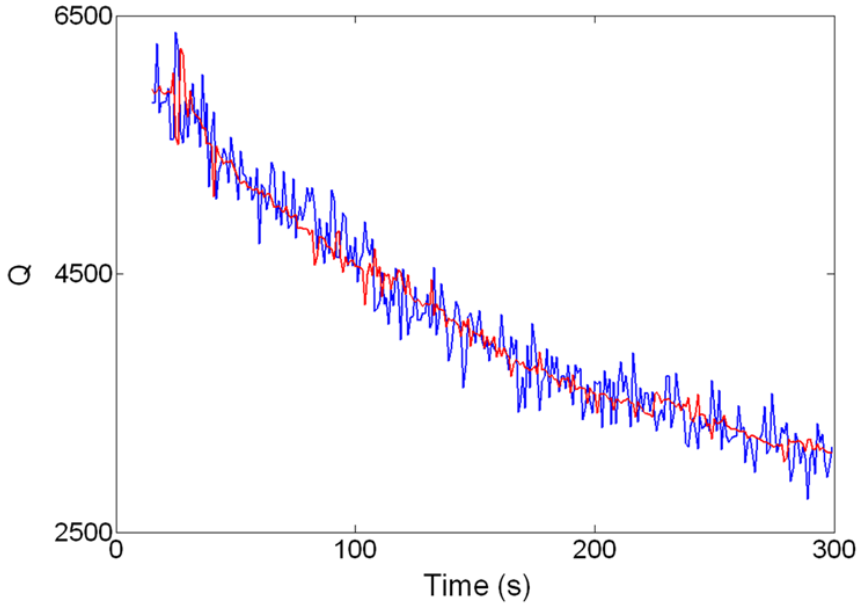


Figure 2.16:  $Q$  versus time measured via ringdowns (blue) and via a scaled measurement of the output voltage to the drive piezo (red). In order to isolate this experiment from possible contributions from the sample or from the feedback electronics, we conducted the experiment in the absence of a sample, with the vacuum vent valve cracked slightly open so that  $Q$  could diminish without any external interference.

tillever's response was linear in drive voltage.

## 2.14 Locating the surface

In many EFM experiments, the location of the surface is determined by gently forcing the cantilever into physical contact with the sample (when the cantilever contacts the surface, the sudden large mechanical deflection causes a large, easily measured spike in the DC signal from the interferometer). This was not a palatable option for our experiment because our low- $k$  cantilevers are extremely delicate and contact with the surface tends to blunt the tip, diminishing the cantilever's quality factor  $Q$  (see Figure 2.11 (d)). Instead, we determined

tip-sample separation by measuring the cantilever’s quality factor via a “ring-down” method, described in detail in Ref. [3] and in Ref. [47]. In this method,  $Q$  is measured as a function of piezo extension, but the cantilever never contacts the surface. The  $Q$  of the cantilever gradually diminishes as the tip nears the surface; this decline is due to interactions between the tip and the sample. The  $Q$  can decrease by as much as 95% before the tip contacts the surface. The nature of these interactions is described in greater detail in Chapters 3 and 4.

The surface is defined as the location at which the quality factor extrapolates to zero. We verified that the technique is accurate to within  $\pm 2$  nm by comparing the results to those obtained from the “forced contact” method (this entailed the sacrifice of several cantilevers). We confirmed that the drive voltage to the cantilever piezo is directly proportional to  $Q$  (see Figure 2.16) and can thus also be used as a means of locating the surface.

## CHAPTER 3

### THEORY OF CANTILEVER JITTER OVER THIN POLYMER FILMS

#### 3.1 Summary

Chapter 3 and Chapter 4 are a summary of the results published in Ref. [14] and in Ref. [15], which together describe a new approach to measuring microscopic electric field gradients in polymers via an analysis of cantilever frequency fluctuations.

In this chapter, we make the case that non-contact friction and frequency jitter over polymers can both originate from dielectric relaxation processes. The connection between frequency jitter and dielectric fluctuations has previously been suggested by Israeloff and co-workers [20, 55]. However, we present the first zero-free parameter theory of cantilever frequency fluctuations over an organic system, and fully describe the dependence of these fluctuations on tip height, dielectric spectrum, polymer film thickness and tip charge. In Chapter 4, we will present experimental evidence consistent with this theory.

The expressions contained in Sections 3.4 to 3.11 were derived entirely by Professor Roger Loring in Ref. [14] and are included here only for the convenience of the reader. The experimentalist may be most interested in the final result, contained in Eq. (3.59), which is an analytical expression for the power spectral density of frequency fluctuations at the cantilever tip in the presence of a thin polymer film.

### 3.2 Literature survey: theoretical studies of jitter and non-contact friction

Stipe et al. [12] studied dissipation over epitaxial gold in high vacuum and introduced the idea that the non-contact friction coefficient  $\Gamma$  is connected to the spectral density of sample electric field fluctuations at the cantilever frequency via the fluctuation-dissipation theorem:

$$\Gamma = \frac{q_c^2 S_E(\omega_c)}{4k_B T}, \quad (3.1)$$

where  $q_c$  is the charge at the tip and  $S_E$  is the spectral density of electric field fluctuations at the cantilever frequency. This was a significant finding because it facilitated a means of access to microscopic electric field fluctuations. They proposed that inhomogeneous fields emanating from the cantilever tip and the sample induced charges in the opposing surface, and that the motion of the tip led to a current, resulting in Ohmic dissipation. However, friction was observed at unexpectedly long ranges, suggesting that their proposed mechanism could not completely account for the effect.

Stipe's work motivated several theoretical [56, 57, 58, 59] and experimental [60, 13, 61, 62, 15] quests for the fundamental origins of electric field fluctuations over metals. Persson et al. [63] calculated the contribution to the non-contact frictional force between moving two flat metal surfaces from Coulombic interactions. They hypothesized that for most practical cases, the Coulomb drag makes a negligible contribution to the friction force. However, they also conceded that their invocation of two perfect single-crystal metal surfaces was improbable and suggested that friction derived from fluctuations could make an important contribution if there were physically adsorbed impurities on the metal surface giv-

ing rise to strong local electric fields. Zurita-Sanchez et al. [59] also derived an expression for the non-contact friction experienced by a classical oscillator induced by the electromagnetic field generated by thermally fluctuating currents in the environment. They predicted that friction is related to correlation functions involving the induced dipole and the fluctuating electric field or field gradient; they also predicted that friction over a dielectric should be considerably larger than that observed over a metal.

Unfortunately, none of these early theories satisfactorily accounted for the large discrepancy between theory and experiment. Persson predicted that even assuming an imperfect crystal, contributions to friction from thermal fluctuations were only expected to be significant at separations of  $d = 1$  nm or less. Stipe and co-workers, on the other hand, observed non-contact friction even at distances  $d = 20$  nm or greater.

To address this discrepancy, Volokitin and Persson [58] refined their model so that it more closely resembled an atomic force microscope tip and a metal substrate in the presence of a bias voltage. They predicted that large long-range non-contact friction is due to the electromagnetic interaction of the moving charges induced on the surface of the tip by the bias voltage, with acoustic vibrations in an adsorbate layer on the surface.

The work of Kuehn et al. [13] is the most relevant to this chapter. They conducted the first measurements of non-contact friction over an organic surface (thin polymer films). They presented a theory linking non-contact friction to the fluctuating electric field correlation function via the complex-valued dielectric response of the sample [61] and conducted experiments that correctly predicted the magnitude of the predicted effect.

Cantilever frequency jitter has not been systematically studied over metals. However, Israeloff et al. [20] have extensively studied frequency fluctuations over thin polymer films. They observed  $1/f$  noise in dielectric materials and theorized that this noise arises from thermal polarization fluctuations, which are related to the dielectric susceptibility via the fluctuation-dissipation theorem. In a series of variable temperature studies, they found that for films of poly(vinyl acetate) and poly(methyl methacrylate),  $1/f$  fluctuations peaked in intensity near the glass transition. They also studied the size of “co-operative regions” within thin polymer films. By assuming that broadband kinetics arise from a distribution of locally exponential processes and that dipoles reorient co-operatively, they estimated that the cooperative length scale for PVAc is on the order of a few nanometers in size [64].

Israeloff and co-workers [46] were the first to access the dielectric spectrum of a polymer by means of scanned probe microscopy. They measured the  $2f$  component of the cantilever frequency, which is directly proportional to the force gradient at the cantilever tip. They then derived a simple expression for the force gradient as a function of the material’s dielectric properties by modeling the tip/dielectric/metal system as a parallel plate capacitor.

### 3.3 Description of the system

The system of interest is depicted in Figure 3.1. We consider a cantilever tip located a distance  $z = d > 0$  above a dielectric slab of thickness  $h$  layered over a conductor. The dielectric slab has a complex-valued dielectric function  $\epsilon(\omega) = \epsilon'(\omega) + i\epsilon''(\omega)$  and a dielectric constant  $\epsilon'(0)$ . The motion of the cantilever

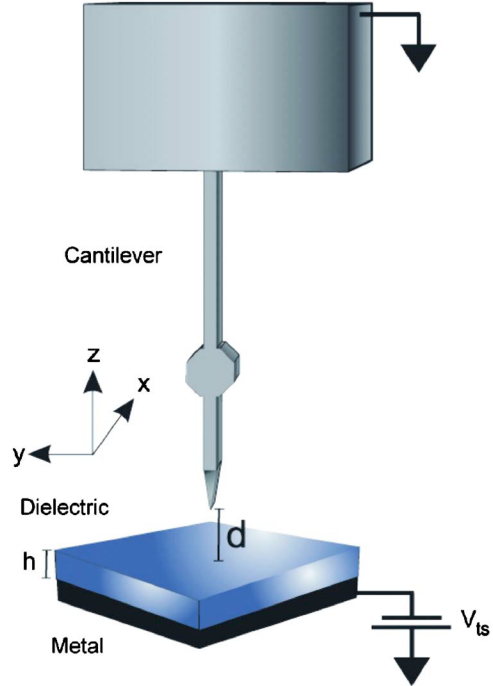


Figure 3.1: To probe electric field fluctuations, a cantilever tip oscillates in the  $x$  direction at height  $z = d$  above the surface of a dielectric sample of thickness  $h$ .

is assumed to be harmonic; this assumption is justified by the experimental observation that the cantilever obeys the equipartition theorem:

$$\langle x_{\text{rms}}^2 \rangle = \frac{k_B T}{k_c}, \quad (3.2)$$

where  $x_{\text{rms}}$  is the mean-squared variation in the cantilever displacement,  $k_B$  is Boltzmann's constant,  $T$  is the temperature and  $k_c$  is the cantilever's spring constant.

The cantilever tip is driven to oscillate in the  $x$  direction by an applied force that undergoes time-random fluctuations,  $F_x(t)$ . We apply a voltage  $V_{\text{ts}}$  between the tip and the sample, enabling us to approximate the tip/vacuum/dielectric/gold system as a parallel plate capacitor with  $q_c = CV_{\text{ts}}$ , where  $C$  is the capacitance, and  $q_c$  is the charge on the cantilever tip. The driven cantilever obeys the Langevin equation given in Eq.(3.3). A Langevin equation

is a stochastic differential equation describing Brownian motion in a potential.

$$\ddot{x}(t) = -\omega_c^2 x(t) - \frac{\gamma}{m} \dot{x}(t) + \frac{q_c}{m} \mathcal{E}_x(x, t), \quad (3.3)$$

where  $\omega_c$  is the resonance frequency of the cantilever,  $\gamma$  is the non-contact friction coefficient and  $m$  is the effective mass (related to the cantilever spring constant  $k_c$  by  $m \equiv k_c/\omega_c^2$ ).

### 3.4 Derivation of cantilever frequency shift induced by a fluctuating electric field

Equation (3.3) implies that both the cantilever's non-contact friction coefficient and its resonance frequency can be affected by changes in the external field  $\mathcal{E}_x(x, t)$ . In this section, we will derive an expression for the change in the cantilever's resonance frequency that occurs in the presence of a fluctuating electric field. This change has both a time-dependent and a time-independent component; the time-dependent component is related to the frequency jitter, an expression for which shall be derived in the next few sections.

We express the fluctuating electric field  $\mathcal{E}_x(x, t)$  in terms of its average value,  $E_x(x) \equiv \langle \mathcal{E}_x(x, t) \rangle_{q_c}$  and the fluctuation about this mean,  $\delta\mathcal{E}_x(x, t)$ ,

$$\mathcal{E}_x(x, t) = E_x(x) + \delta\mathcal{E}_x(x, t). \quad (3.4)$$

The angular brackets  $\langle \dots \rangle_{q_c}$  designate an average over all degrees of freedom of the dielectric in the presence of nonzero probe charge  $q_c$ . Both mean and fluctuation are then linearized in  $x$  about  $x = 0$ ,

$$E_x(x) \approx E_x(0) + xE_{xx}, \quad (3.5)$$

$$\delta\mathcal{E}_x(x, t) \approx \delta\mathcal{E}_x(t) + x\delta\mathcal{E}_{xx}(t), \quad (3.6)$$

with  $E_{xx} \equiv (\partial E_x / \partial x)_{x=0}$  and  $\delta\mathcal{E}_{xx}(t) \equiv (\partial \delta\mathcal{E}_x(x, t) / \partial x)_{x=0}$ . We may now re-write the fluctuating electric field term in the Langevin equation so that it reflects the linearization:

$$\ddot{x}(t) = -\omega_c^2 x(t) - \frac{\gamma}{m} \dot{x}(t) + \frac{q_c}{m} (E_x(0) + x(t)E_{xx} + \delta E_x(t) + x(t)\delta E_{xx}(t)), \quad (3.7)$$

Grouping terms together yields:

$$\ddot{x}(t) = -(\omega_c^2 - E_{xx} - \delta E_{xx}(t))x(t) - \frac{\gamma}{m} \dot{x}(t) + \frac{q_c}{m} (E_x(0) + \delta E_x(t)), \quad (3.8)$$

Within this linearization, we may formulate the following expression:

$$\omega' \approx (\omega^2 - \frac{q}{m} E_{xx} - \frac{q}{m} \delta E_{xx}(t))^{1/2}, \quad (3.9)$$

Dividing through by  $\omega$  yields:

$$\frac{\omega'}{\omega} \approx (1 - \frac{q}{m\omega^2} E_{xx} - \frac{q}{m\omega^2} \delta E_{xx}(t))^{1/2}, \quad (3.10)$$

For  $y = (1 + x)^b$  and  $bx \ll 1$ , the Taylor expansion of  $y \approx (1 + xb)$ . Thus:

$$\frac{\omega'}{\omega} \approx 1 - \frac{q}{2m\omega^2} E_{xx} - \frac{q}{2m\omega^2} \delta E_{xx}(t), \quad (3.11)$$

Finally,

$$\omega' \approx \omega - \frac{q}{2m\omega} E_{xx} - \frac{q}{2m\omega} \delta E_{xx}, \quad (3.12)$$

Equation 3.3 thus becomes a Langevin equation for a Brownian harmonic oscillator with a frequency containing a static field-induced shift  $\Delta\omega_c$ , as well as a time-varying fluctuation  $\delta\omega_c(t)$ ,

$$\ddot{x}(t) = -\omega_c'^2(t)x(t) - \frac{\gamma}{m} \dot{x}(t) + \frac{q_c}{m} \delta\mathcal{E}_x(t), \quad (3.13)$$

$$\omega_c(t) \approx \bar{\omega}_c + \delta\omega_c(t), \quad (3.14)$$

$$\bar{\omega}_c \equiv \omega_c + \Delta\omega_c, \quad (3.15)$$

$$\Delta\omega_c \equiv -\frac{q_c}{2m\omega_c} E_{xx}, \quad (3.16)$$

$$\delta\omega_c(t) \equiv -\frac{q_c}{2m\omega_c} \delta\mathcal{E}_{xx}(t). \quad (3.17)$$

In Eq. (3.14), we have made the experimentally justified [13] assumption that the field-induced frequency shifts are small compared to the resonance frequency.

### 3.5 Friction and jitter

We now proceed to seek relationships between non-contact friction and frequency jitter and fluctuations in the dielectric slab. We assume that the dielectric slab undergoes thermally induced, time-random fluctuations, and that the tip charge  $q_c$  has no effect on these fluctuations (or, effectively, that  $q_c = 0$ ).

In the absence of perturbation by the tip charge  $q_c$ , the friction coefficient in Eq. (3.13) is related to the equilibrium correlation function of electric field fluctuations by the fluctuation-dissipation relation [12, 61] given in Eq. (3.18). The fluctuation-dissipation theorem states that the response of a system in thermodynamic equilibrium to a small applied force is the same as its response to a spontaneous fluctuation. Eq. (3.18) encapsulates the direct relationship between the fluctuation properties of the thermodynamic system and its linear response properties [61].

$$\gamma = \frac{q_c^2}{k_B T} \int_0^\infty dt \cos(\omega_c t) C_{xx}(t), \quad (3.18)$$

$$C_{xx}(t) \equiv \langle \mathcal{E}_x(t) \mathcal{E}_x(0) \rangle \quad (3.19)$$

In Eq. (3.19),  $\langle \dots \rangle$  is the correlation function for the fluctuating electric field  $\mathcal{E}_x(t)$ . A correlation function for a fluctuating quantity  $A$  may be defined as

$$C(t) = \langle \delta A(0) \delta A(t) \rangle = \langle A(t) A(0) \rangle - \langle A \rangle^2, \quad (3.20)$$

and can be conceptualized as a means of quantifying the time over which the system has a “memory” of its previous state [47]. The correlation function  $C_{xx}(t)$

represents the equilibrium average of the thermally induced electric field fluctuations. Eq. (3.18) implies that non-contact friction should be quadratic in tip charge  $q_c$ . In Chapter 4, we will present experimental data confirming that this is the case.

We will characterize the frequency jitter by its power spectrum  $P_{\delta\omega_c}(\omega)$  [20, 45, 64, 65, 66],

$$P_{\omega_c}(\omega) = 4 \int_0^\infty dt \cos \omega t \langle (\delta\omega(t))(\delta\omega(0)) \rangle, \quad (3.21)$$

Substituting Eq. (3.17) yields,

$$P_{\omega_c}(\omega) = 4 \int_0^\infty dt \cos \omega t \langle (-\frac{q_c}{2m\omega_c} \delta\mathcal{E}_{xx}(t))(-\frac{q_c}{2m\omega_c} \delta\mathcal{E}_{xx}(0)) \rangle, \quad (3.22)$$

If  $C_{xx,xx}(t) = \langle \delta\mathcal{E}_{xx}(t)\delta\mathcal{E}_{xx}(0) \rangle$ , then

$$P_{\omega_c}(\omega) = -\frac{q_c^2}{m^2\omega_c^2} \int_0^\infty dt \cos \omega t C_{xx,xx}(t), \quad (3.23)$$

Integrating this expression over  $\omega$  and remembering that  $\int_0^\infty dt \cos \omega t = \pi\delta(t)$  yields

$$\langle (\delta\omega)^2 \rangle = \left( \frac{q_c^2}{4m^2\omega_c^2} \right) \int_0^\infty dt \delta(t) C_{xx,xx}(t). \quad (3.24)$$

Setting  $t = 0$  yields an expression for the mean-squared frequency fluctuations in terms of a fluctuating electric field correlation function,

$$\langle (\delta\omega_c)^2 \rangle = \left( \frac{q_c^2}{4m^2\omega_c^2} \right) C_{xx,xx}(0). \quad (3.25)$$

According to this analysis, non-contact friction originates from electric field fluctuations within the dielectric, and frequency jitter arises from electric field gradient fluctuations within the dielectric. Evaluation of the noncontact friction requires the equilibrium correlation function of electric field fluctuations in Eq. (3.19), while evaluation of the statistics of frequency jitter requires the equilibrium correlation function of electric field gradient fluctuations that appears in

Eq. (3.24). The calculation of these two quantities is addressed in Sections 3.7 and 3.9.

### 3.6 Field correlation functions from linear response theory

The objective of this analysis is to calculate the spontaneous thermal fluctuations associated with a thin dielectric slab. Recall that the fluctuation dissipation theorem states that the response of a system to a spontaneous fluctuation is equivalent to the response of the same system to a perturbation. Our approach is to calculate the response of the dielectric to a *fictitious* perturbation at the location of the cantilever tip. It is important to remember that the actual tip charge  $q_c$  is assumed to exert no effect on the thin dielectric slab.

We calculate the field and field-gradient autocorrelation functions in Eqs. (3.19) and (3.24) by assuming that the fluctuating electric field in the sample responds linearly to a perturbation. We imagine that this perturbation is a fictitious time-varying charge distribution located at the cantilever tip, which polarizes the dielectric. This polarization in turn produces an electric reaction field [67] back at the tip. The reaction field is then calculated using the quasi-static approximation to electrodynamics, in which Fourier components of the electric field and charge distribution are assumed to obey the static version of Maxwell's equations [67, 68].

The electric field correlation function  $\hat{C}_{xx}(\omega)$  is determined by considering the polarization of the dielectric by a time-varying electric dipole, since the electric dipole moment couples to the electric field in the Hamiltonian. The electric field-gradient correlation function  $\hat{C}_{xx,xx}(\omega)$  is calculated by treating the interac-

tion of the dielectric with a time-varying electric quadrupole, since this quantity couples to electric field gradients in the Hamiltonian.

As stated previously, these dipole and quadrupole perturbations are fictitious. They do not physically represent any aspect of the actual measurement, but are devices in a thought experiment that allow the equilibrium electric field and electric field gradient correlation functions to be calculated from macroscopic electrostatics. The fictitious charge distributions are deliberately chosen so that a linear response calculation of the reaction field [69, 67, 70, 71] generated by the dielectric requires a “response function” related to the autocorrelation function we seek. The response function is defined in the next section.

### 3.7 Connection between non-contact friction and electric field correlation function

To compute the coefficient of noncontact friction, we consider a fictitious electric dipole  $\mu(t)$ , oriented along  $x$ , and located at  $z = d > 0$ , interacting with the dielectric according to the perturbation Hamiltonian

$$H_{\text{int}}(t) = -\mu(t)\mathcal{E}_x(t). \quad (3.26)$$

where  $\mathcal{E}_x(t)$  is the fluctuating reaction field induced by the dipole perturbation. We choose a dipole because its energy is linear in electric field. Because materials do not polarize instantaneously in response to an applied field, it is necessary to define a “linear response function” that describes the time-dependent response of the electric field to the perturbation. Classical mechanical linear response theory can be used to relate the reaction field to the perturbing dipole

through the response function  $\Phi_\mu(t)$

$$\mathcal{E}_x(t) = \int_0^t d\tau \Phi_\mu(t - \tau) \mu(\tau), \quad (3.27)$$

where  $t$  is the time at which the field is measured and  $\tau$  is the time at which the perturbation takes place. The response function is given by:

$$\Phi(t) = -\frac{1}{k_B T} \frac{d}{dt} C_{xx}(t) \quad (3.28)$$

where  $C_{xx}(t)$  is the equilibrium correlation function of electric field fluctuations, as defined in Eq. (3.19). It is useful to define the Fourier-Laplace transform of  $C_{xx}(t)$ :

$$\hat{C}_{xx}(\omega) = \int_0^\infty dt e^{i\omega t} C_{xx}(t) = \hat{C}'_{xx}(\omega) + i\hat{C}''_{xx}(\omega). \quad (3.29)$$

Eqs. (3.27) and (3.28) are more compactly formulated in Fourier space:

$$\hat{\mathcal{E}}_x(\omega) = \hat{\mu}(\omega) \hat{\Phi}_\mu(\omega), \quad (3.30)$$

$$\hat{\Phi}_\mu(\omega) = \frac{[i\omega \hat{C}_{xx}(\omega) + C_{xx}(0)]}{k_B T} \quad (3.31)$$

The final expression for the reaction field is thus:

$$\hat{\mathcal{E}}_x(\omega) = \hat{\mu}(\omega) \frac{[i\omega \hat{C}_{xx}(\omega) + C_{xx}(0)]}{k_B T} \quad (3.32)$$

However, for the purposes of computing non-contact friction, we need only consider the real part of the complex correlation function defined in Eq.(3.29), which is related to the friction via the fluctuation-dissipation theorem, expressed below in frequency space:

$$\gamma = \frac{q_c^2}{k_B T} \hat{C}'_{xx}(\omega_c) \quad (3.33)$$

In the next section, we will derive an expression for the response function  $\hat{\Phi}_\mu(\omega)$  using electrostatics, which in turn will yield an expression for  $\gamma$ .

### 3.8 Solving for the reaction field

The time-independent electric field  $E_x$  defined in Eq. (3.5) obeys the conventional form of Maxwell's equations, and is related to the microscopic, time-dependent fluctuating field  $\mathcal{E}_x$  in Eq. (3.26) by  $E_x = \langle \mathcal{E}_x \rangle$ , with the brackets denoting an average over the degrees of freedom of the dielectric. We invoke the quasi-static approximation,

$$\nabla \times \hat{\mathbf{E}}(\omega) = 0, \quad (3.34)$$

$$\epsilon(\omega) \nabla \cdot \hat{\mathbf{E}}(\omega) = 4\pi \hat{\rho}(\omega), \quad (3.35)$$

with  $\epsilon(\omega)$  the complex-valued dielectric function and  $\hat{\rho}(\omega)$  the free charge density. The system is subject to the boundary conditions of continuity across the interface of the component of the electric displacement  $\epsilon(\omega)\hat{\mathbf{E}}(\omega)$  perpendicular to the interface and of the component of  $\hat{\mathbf{E}}(\omega)$  parallel to the interface. We now solve for the response function  $\hat{\Phi}_\mu''(\omega)$  by treating the problem as a boundary value problem which may be solved, for example, by the method of images [61]

$$\hat{\Phi}_\mu(\omega) = \frac{\zeta(\omega)}{2d^3} I_2(\omega), \quad (3.36)$$

$$I_n(\omega) \equiv \int_0^\infty dq q^n e^{-2q} \left( \frac{1 - e^{-4q(h/d)}}{1 + \zeta(\omega)e^{-2q(h/d)}} \right), \quad (3.37)$$

$$\zeta(\omega) \equiv \frac{\epsilon(\omega) - 1}{\epsilon(\omega) + 1}. \quad (3.38)$$

Substitution of this result for the response function in Eq. (3.31) for the field autocorrelation function gives

$$\hat{C}'_{xx}(\omega) = \frac{k_B T \zeta''(\omega)}{2\omega d^3} J_2(\omega), \quad (3.39)$$

$$\begin{aligned} J_n(\omega) &\equiv \int_0^\infty dq q^n e^{-2q} \\ &\times \left( \frac{1 - e^{-4q(h/d)}}{(1 + \zeta'(\omega)e^{-2q(h/d)})^2 + (\zeta''(\omega))^2 e^{-4q(h/d)}} \right). \end{aligned} \quad (3.40)$$

In the limit of infinite dielectric thickness  $h \gg d$ , the integral in Eq. (3.40) may be performed analytically, and the field autocorrelation function varies as  $d^{-3}$ ,

$$\hat{C}'_{xx}(\omega) \approx \left( \frac{k_B T}{4\omega d^3} \right) \left( \frac{\epsilon''(\omega)}{|\epsilon(\omega) + 1|^2} \right). \quad (3.41)$$

For finite sample thickness, additional  $d$  dependence results from the integral in Eq. (3.40). The noncontact friction for arbitrary  $h/d$  follows from substituting Eq. (3.39) into Eq. (3.18) [13, 61]:

$$\gamma = \frac{q_c^2 \zeta''(\Omega)}{2\Omega d^3} J_2(\omega_c). \quad (3.42)$$

This relation connects  $\gamma$  to the tip charge, sample dielectric function and thickness, and tip-sample separation.

### 3.9 Connection between frequency jitter and electric field gradient correlation function

We next apply this response function strategy to calculate the autocorrelation function of field gradient fluctuations. A fictitious time-varying electric quadrupole is located a distance  $d > 0$  from the interface. The quadrupole tensor is diagonal in the Cartesian basis of Figure 3.1, with nonzero quadrupole tensor elements  $Q_{xx} \equiv Q(t)$ ,  $Q_{yy} = Q_{zz} = -Q(t)/2$ . This charge distribution may be visualized, for example, as a central charge of magnitude  $-2q(t)$  with two charges of magnitude  $q(t)$  displaced from the central charge along  $x$  by  $\pm r$ , in the limit  $r \rightarrow 0$  with  $4q(t)r^2 = Q(t)$ . The orientation of this charge distribution is chosen for convenience, in that rotating this quadrupole would not alter the final results obtained below. The interaction between quadrupole and medium

is specified by the Hamiltonian

$$H_{\text{int}}(t) = -\frac{Q(t)}{6} \left[ \frac{\partial \mathcal{E}_x}{\partial x} - \left(\frac{1}{2}\right) \frac{\partial \mathcal{E}_y}{\partial y} - \left(\frac{1}{2}\right) \frac{\partial \mathcal{E}_z}{\partial z} \right]. \quad (3.43)$$

The analog of Eqs. (3.27)-(3.28) relating macroscopic field gradients to response functions  $\hat{\Phi}_Q^\alpha(\omega)$  and then to correlation functions of fluctuating field gradients is

$$\hat{E}_{\alpha\alpha}(\omega) = \hat{Q}(\omega) \hat{\Phi}_Q^\alpha(\omega), \quad (3.44)$$

$$\begin{aligned} \hat{\Phi}_Q^\alpha(\omega) &= \frac{1}{6k_B T} \left[ i\omega \hat{C}_{\alpha\alpha,xx}(\omega) + C_{\alpha\alpha,xx}(0) \right. \\ &\quad - \frac{1}{2} \left( i\omega \hat{C}_{\alpha\alpha,yy}(\omega) + C_{\alpha\alpha,yy}(0) \right) \\ &\quad \left. - \frac{1}{2} \left( i\omega \hat{C}_{\alpha\alpha,zz}(\omega) + C_{\alpha\alpha,zz}(0) \right) \right], \end{aligned} \quad (3.45)$$

with  $\alpha = x, y, z$  and  $C_{\alpha\alpha,\beta\beta}(t) \equiv \langle (\partial \mathcal{E}_\alpha(t)/\partial \alpha)(\partial \mathcal{E}_\beta(0)/\partial \beta) \rangle$ . Solving the quasistatic version of Maxwell's equations in Eqs. (3.34) and (3.35) for these field gradients gives

$$\hat{\Phi}_Q^x(\omega) = \frac{9}{4} R(\omega), \quad (3.46)$$

$$\hat{\Phi}_Q^y(\omega) = \frac{3}{4} R(\omega), \quad (3.47)$$

$$\hat{\Phi}_Q^z(\omega) = -3R(\omega), \quad (3.48)$$

$$R(\omega) \equiv \frac{\zeta(\omega)}{24d^5} I_4(\omega). \quad (3.49)$$

The integral  $I_4(\omega)$  is defined in Eq. (4.10). Equations (3.46)-(3.48) necessarily satisfy  $\sum_\alpha \hat{\Phi}_Q^\alpha(\omega) = 0$ , which follows from  $\nabla \cdot \hat{\mathbf{E}}(\omega) = 0$ .

The jitter power spectrum in Eq. (3.22) is proportional to the cosine transform  $\hat{C}'_{xx,xx}(\omega)$ . Taking the imaginary parts of Eqs. (3.46)-(3.48) relates cosine transforms of various field gradient correlation functions to the imaginary part of  $R(\omega)$  in Eq. (3.49).

$$\left( \frac{27k_B T}{2\omega} \right) R'' = \hat{C}'_{xx,xx} - \frac{1}{2} \hat{C}'_{xx,yy} - \frac{1}{2} \hat{C}'_{xx,zz}, \quad (3.50)$$

$$\left(\frac{9k_B T}{2\omega}\right)R'' = \hat{C}'_{yy,xx} - \frac{1}{2}\hat{C}'_{yy,yy} - \frac{1}{2}\hat{C}'_{yy,zz}, \quad (3.51)$$

$$\left(\frac{18k_B T}{\omega}\right)R'' = \frac{1}{2}\hat{C}'_{zz,yy} - \hat{C}'_{zz,xx} + \frac{1}{2}\hat{C}'_{zz,zz}. \quad (3.52)$$

These field gradient correlation functions are not all distinct. From classical mechanical time-reversal symmetry,  $\hat{C}'_{\alpha\alpha,\beta\beta}(\omega) = \hat{C}'_{\beta\beta,\alpha\alpha}(\omega)$  and from the isotropy of this particular problem in the  $xy$  plane,  $\hat{C}'_{xx,xx}(\omega) = \hat{C}'_{yy,yy}(\omega)$  and  $\hat{C}'_{xx,zz}(\omega) = \hat{C}'_{yy,zz}(\omega)$ . With these equalities, Eqs. (3.51) and (3.52) become

$$\left(\frac{9k_B T}{2\omega}\right)R'' = \hat{C}'_{xx,yy} - \frac{1}{2}\hat{C}'_{xx,xx} - \frac{1}{2}\hat{C}'_{xx,zz}, \quad (3.53)$$

$$\left(\frac{18k_B T}{\omega}\right)R'' = \frac{1}{2}(\hat{C}'_{zz,zz} - \hat{C}'_{xx,zz}), \quad (3.54)$$

so that Eqs. (3.50), (3.53), and (3.54) represent three constraints for four unknown correlation functions.

The fourth constraint required to determine  $\hat{C}'_{xx,xx}(\omega)$  is constructed by applying the quasistatic version of Maxwell's equations to the mesoscopic fluctuating field  $\mathcal{E}$  rather than the macroscopic averaged field  $\mathbf{E}$  in Eqs. (3.34) and (3.35). In the Maxwell's equations obeyed by  $\mathbf{E}$ , the dielectric medium is represented by its dielectric function  $\epsilon(\omega)$ , while in the Maxwell's equations obeyed by  $\mathcal{E}$ , the medium is represented microscopically as a time-varying charge distribution. In vacuum, the fluctuating field satisfies  $\nabla \cdot \mathcal{E}(t) = 0$ , so that for  $z > 0$ ,

$$\begin{aligned} \langle (\nabla \cdot \mathcal{E}(t)) (\nabla \cdot \mathcal{E}(0)) \rangle &= 2C_{xx,xx}(t) + C_{zz,zz}(t) + \\ &\quad 4C_{xx,zz}(t) + 2C_{xx,yy}(t) = 0. \end{aligned} \quad (3.55)$$

Taking Fourier transforms yields,

$$\hat{C}'_{xx,xx} + \frac{1}{2}\hat{C}'_{zz,zz} + 2\hat{C}'_{xx,zz} + \hat{C}'_{xx,yy} = 0. \quad (3.56)$$

Equations (3.50), (3.53), (3.54) and (3.56) provide four independent constraints for four field-gradient correlation functions, and can be solved for the desired  $\hat{C}'_{xx,xx}(\omega)$ ,

$$\hat{C}'_{xx,xx}(\omega) = \frac{3k_B T \zeta''(\omega)}{8\omega d^5} J_4(\omega). \quad (3.57)$$

The integral  $J_4(\omega)$  is defined in Eq. (3.40). As with Eq. (3.39) for the field autocorrelation function, Eq. (3.57) simplifies in the limit of an infinitely thick sample,  $h/d \gg 1$ ,

$$\hat{C}'_{xx,xx}(\omega) = \left( \frac{9k_B T}{16\omega d^5} \right) \left( \frac{\epsilon''(\omega)}{|\epsilon(\omega) + 1|^2} \right). \quad (3.58)$$

The jitter power spectrum for general  $h/d$  may then be determined,

$$P_{\omega_c}(\omega) = \frac{3q_c^2 k_B T \zeta''(\omega)}{8m^2 \omega_c^2 \omega d^5} J_4(\omega). \quad (3.59)$$

In the limit of low frequency [20, 45],  $\epsilon''(\omega) \ll \epsilon'(\omega) \approx \epsilon'(0)$ , the power spectrum in Eq. (3.59) factors into a product of a function of frequency and a function of tip-sample separation and sample thickness,

$$P_{\omega_c}(\omega) \approx \frac{3q_c^2 k_B T J_4(0)}{4m^2 \omega_c^2 d^5 (\epsilon'(0) + 1)^2} \left( \frac{\epsilon''(\omega)}{\omega} \right). \quad (3.60)$$

Frequency jitter may also be more simply characterized by the mean-squared frequency fluctuation in Eq. (4.8). The zero-time limit of the field gradient correlation function may be obtained by the static analog of the strategy that produced Eqs. (3.50), (3.53), (3.54) and (3.56). The static analogs of these relations may be obtained with the substitutions  $\hat{C}'_{\alpha\alpha,\beta\beta}(\omega) \rightarrow C_{\alpha\alpha,\beta\beta}(0)$  and  $R''(\omega)/\omega \rightarrow R(0)$ . The mean-squared frequency fluctuation is then given by

$$\langle (\delta\omega)^2 \rangle = \frac{3q_c^2 k_B T \zeta(0)}{32m^2 \omega_c^2 d^5} I_4(0), \quad (3.61)$$

with  $I_4(0)$  the integral in Eq. (4.10) with  $n = 4$  and with  $\epsilon(\omega)$  set to  $\epsilon'(0)$ . The mean-squared frequency fluctuation depends on the dielectric constant  $\epsilon'(0)$ , through  $\zeta(0)$ , defined as the zero frequency limit of Eq. (4.11).

### 3.10 Comparison to results of Israeloff et al.

The power spectrum of the frequency jitter induced by a dielectric on an oscillating charged probe has been measured by Israeloff and coworkers [20, 45] and analyzed with the form

$$P_{\omega_c}(\omega) = \left( \frac{\partial \bar{\omega}}{\partial V_{ts}} \right)^2 (4C_0G) \left( \frac{k_B T \epsilon''(\omega)}{\omega C^2} \right), \quad (3.62)$$

with  $C$  and  $C_0$  respectively the capacitance with and without the dielectric sample. These experiments were carried out with a probe oscillating perpendicular to the interface rather than parallel to it as considered here.  $G$  is a dimensionless factor that is stated [45, 20] to depend on experimental geometry and on the dielectric constant of the sample. Like our limiting expression for  $\omega \rightarrow 0$  in Eq. (3.60), Eq. (3.62) factors into a product of a function of  $\omega$  and a function depending on dielectric constant and geometry. The two expressions predict the same  $\omega$  dependence:  $\epsilon''(\omega)/\omega$ . To compare the frequency-independent factors in Eqs. (3.62) and (3.60), we must determine the voltage derivative of the mean probe frequency appearing in Eq. (3.62). The static, sample-induced shift in the probe frequency is related in Eq. (3.16) to the averaged field gradient  $E_{xx}$ . Solving the same electrostatics boundary value problem that led to Eq. (3.61) gives

$$E_{xx} = -\frac{\zeta(0)q_c}{2d^3} I_2(0), \quad (3.63)$$

with  $I_2(\omega)$  defined in Eq. (4.10). The tip charge  $q_c$  is then proportional to the voltage derivative of the frequency in Eq. (3.16), according to

$$q_c = \left( \frac{\partial \bar{\omega}}{\partial V_{ts}} \right) \frac{2m\omega d^3}{\zeta(0)I_2(0)C}. \quad (3.64)$$

Substitution of this result into our limiting expression for  $P_{\omega_c}(\omega)$  in Eqs. (3.60) gives

$$P_{\omega_c}(\omega) = \left( \frac{\partial \bar{\omega}}{\partial V_{ts}} \right)^2 \left( \frac{3dJ_4(0)}{[\zeta(0)I_2(0)(\epsilon'(0) + 1)]^2} \right) \left( \frac{k_B T \epsilon''(\omega)}{\omega C^2} \right). \quad (3.65)$$

Comparison of our limiting Eq. (3.65) to Eq. (3.62) shows that the two relations predict the same frequency dependence for  $S(\omega)$ , with Eq. (3.65) providing explicit dependence on dielectric constant, sample thickness, and tip-sample separation.

### 3.11 Field correlation functions from stochastic electrodynamics

In the previous section, we showed a calculation for the autocorrelation functions of electric field and electric field gradient fluctuations by determining the response functions associated with the reaction fields induced by fictitious time-varying charge distributions. These reaction fields were then determined with a quasistatic approximation to electrodynamics.

Reference [14] describes an alternative strategy, also devised by Professor Roger Loring, based on a full electrodynamic description, applying the stochastic form of Maxwell's equations used by Lifshitz [72, 73, 74] to determine the dispersion force [75, 76] between two semi-infinite dielectric slabs to calculate the correlation functions directly in the absence of external charge distributions. The result of the analysis is identical to the result of Section 3.9. However, this approach is more readily generalizable and has the potential to treat a more complete model of the measurement.

### 3.12 Conclusions

In summary, we have derived expressions for the non-contact friction and jitter experienced by a cantilever in close proximity to a thin dielectric slab. Our results have two potential applications. First, they can provide a means for predicting frequency jitter and friction that can limit the direct mechanical detection of very weak spin forces ([19, 11]) and hence may find application in designing such measurements. Second, they can be applied to interpret electric force microscopy results as a local probe of dielectric fluctuations ([47]) at surfaces.

# CHAPTER 4

## MEASUREMENT OF LOW-FREQUENCY CANTILEVER NOISE OVER THIN POLYMER FILMS

### 4.1 Summary

It has been observed by us [15] and by others [20] that when a charged cantilever tip and a thin polymer film are in close proximity, the time-random noise in the cantilever's resonance frequency significantly increases. In this chapter, we seek the origins of this phenomenon and present the most sensitive and most broadband measurements to date of frequency noise over an organic system. In Chapter 3, we presented a zero-free parameter theory identifying the source of the excess noise as dielectric relaxation processes within the polymer film. Here we show that the theory is consistent with the experimental evidence.

This finding is significant because it confirms that the entire low frequency spectrum of electric field gradient fluctuations is encoded in cantilever frequency noise [55, 46]. Moreover, our results show that our custom-made cantilevers are a particularly broadband detector, capable of quantifying electric field gradient fluctuations from below  $10^{-2}$  Hz to nearly  $10^3$  Hz. Our findings can potentially be applied to probe other microscopic fluctuations, such as charge fluctuations in heterogeneous electronic materials. In this chapter, we also:

- (a) describe the experimental techniques involved in measuring and analyzing cantilever frequency fluctuations (Sections 4.3, 4.4)
- (b) show that noise in the cantilever's resonance frequency can contain a wealth of information about both the sample and the apparatus (Section 4.6), and

(c) describe a method for separating noise emanating from the sample from noise intrinsic to the apparatus (Section 4.5).

## 4.2 Literature survey: scanned probe studies of electric field fluctuations

The first measurements of local electric field fluctuations via scanned probe microscopy were conducted by Denk and Pohl [77], who measured dissipation by monitoring changes in the cantilever's mechanical quality factor. They found that cantilever dissipation over GaAs/AlGaAs semiconductor heterostructures depended on the dopant concentration, the type of material, and the applied voltage. This was an important result because it established that cantilever dissipation can be sensitive to the electrical properties of the sample. Stowe *et al.* [5] extended this work by using non-contact friction to measure doping levels in silicon. Stipe *et al.* [12] studied dissipation over epitaxial gold in high vacuum and introduced the idea that the cantilever's non-contact friction coefficient  $\gamma$  can be connected to random electric field fluctuations within a sample via the fluctuation-dissipation theorem. This was a significant finding because it established a relationship between  $\gamma$ , which is relatively easy to measure, and microscopic electric field fluctuations, which are almost impossible to determine experimentally by other means. Stipe's work motivated several theoretical [56, 57, 58, 78, 59] and experimental [60, 13, 61, 62, 15] quests for the fundamental origins of electric field fluctuations over metals.

Israeloff and coworkers [20, 45] used commercial cantilevers to study low-frequency cantilever frequency fluctuations near the glass transition tempera-

ture in thin films of PVAc and PMMA. Two major conclusions can be drawn from their work on thin films of PVAc: that low-frequency cantilever frequency noise can be an effective probe of dielectric relaxation, and that the intensity of low-frequency  $1/f$  fluctuations peaks near the polymer's glass transition temperature. These were the first studies to suggest that low frequency ( $<1$  Hz)  $1/f$  fluctuations could be related to thermal dielectric polarization fluctuations. Unfortunately, their experiments relied on commercial cantilevers that restricted their measurements to extremely low frequencies, limiting their ability to make a systematic test of their hypothesis. Furthermore, their theory did not explicitly account for the dependence of the fluctuations on experimental parameters like the tip-sample separation, the thickness of the film or the identity of the polymer. In the present study, we attempt to address these issues and several others.

Kuehn *et al.* [13] achieved the first direct mechanical detection of non-contact friction due to local electric field fluctuations in an organic system. They used ultra-sensitive cantilevers to measure energy losses over PMMA (poly(methyl methacrylate)), PVAc (poly(vinyl acetate)) and polystyrene thin films and found that the cantilever's non-contact friction parameter  $\gamma$  was directly proportional to the spectral density of electric field fluctuations within the polymer film occurring at the cantilever's resonance frequency. They also presented a theory delineating the quantitative dependence of non-contact friction on parameters including the tip charge, the tip-sample separation and the complex-valued dielectric response of the sample  $\epsilon(\omega)$  [61].

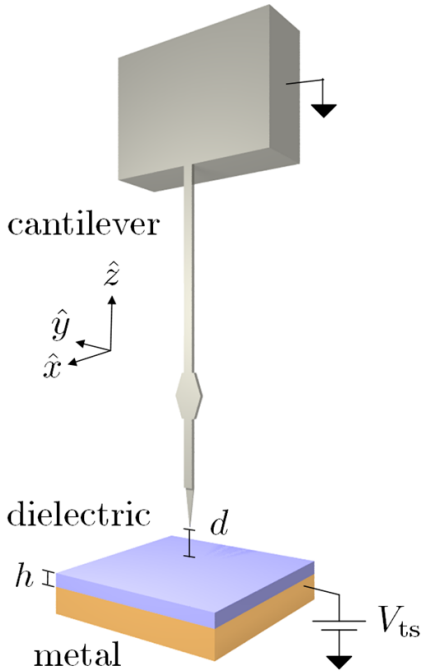


Figure 4.1: Configuration of the experiment: a charged cantilever tip oscillates in the  $x$  direction, parallel to the sample surface, at a height  $z = d$  above the surface of a dielectric sample of thickness  $h$ . The tip is charged by applying a voltage  $V_{ts}$  between the tip and a metal film under the sample.

### 4.3 Configuration of the experiment

We measured cantilever frequency noise in the vicinity of the cantilever's resonance frequency as a function of distance and sample thickness over three different polymers. A schematic of the experiment is depicted in Figure 4.1. Chapter 2 contains a detailed description of the apparatus. We prepared thin polymer films from the following species: poly(methyl methacrylate), poly(vinyl acetate), and polystyrene. Chemical structures of the polymers are shown in Figure 4.2, and their specifications are given in Table 4.1. All polymers were spin-cast from toluene onto epitaxial Au(111)-on-mica substrates (Agilent; Part No. N9805B-FG). Sample thicknesses were measured by profileometry. The samples were annealed in a high vacuum oven ( $P = 10^{-6}$  mbar) and annealed at

Table 4.1: Polymers studied. Here  $\epsilon_r$  is the relative dielectric constant,  $M_w$  is the weight-averaged molecular weight,  $M_w/M_n$  is the polydispersity, and  $T_g$  is the glass transition temperature from Refs. [79, 80, 81].

polymer	$\epsilon_r$	$M_w$ (kDa)	$M_w/M_n$	$T_g$ (°C)	Maker
atactic PMMA	3.9	145	1.05	115	Scientific Polymer Products
atactic PVAc	2.4	140	3.1	35	Aldrich
polystyrene	2.5	151	1.09	108	Scientific Polymer Products

$T_g + 10^\circ\text{C}$  for 12 hours to remove solvent and water. We obtained  $T_g$  values from the literature [79, 80, 81].

All measurements of cantilever frequency noise were carried out using the custom-fabricated silicon cantilevers described in 2.11. Several different cantilevers used were used in the experiment; all were  $L=275\ \mu\text{m}$  long,  $7\ \mu\text{m}$  wide and  $340\ \text{nm}$  thick with resonance frequencies between 5 and 6 kHz and mechanical quality factors as high as 15 000 in high vacuum ( $P = 10^{-6}\ \text{mbar}$ ). The spring constants of the cantilevers varied from  $7.6 \times 10^{-4}\ \text{N/m}$  to  $1.7 \times 10^{-3}\ \text{N/m}$ . Cantilever spring constants were measured using the approach pioneered by Hutter and Beckhoefer [82]. This method is described fully in Appendix E. We affixed an ultra-sensitive cantilever to our custom-built scanning probe microscope and applied a voltage  $V_{ts}$  between the cantilever and the substrate. The cantilever was gradually lowered until the distance  $d$  between the tip and the sample was 1000 nm or less in accordance with the protocol described in 2.14. The cantilever was driven to oscillate at its resonance frequency via the custom-built analog positive feedback circuit described in 2.13. The instantaneous cantilever frequency  $f_c(t)$  was determined by means of a software frequency demodulator, as described in 4.4. The next section describes a method for generating a power spectrum of cantilever frequency noise.

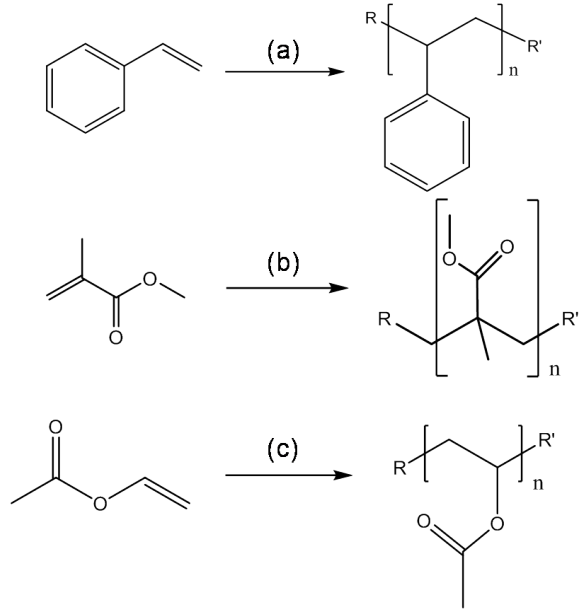


Figure 4.2: Polymers studied. We measured frequency fluctuations over thin films of three different polymers: (a) polystyrene, (b) poly(methyl methacrylate) and (c) poly(vinyl acetate).

#### 4.4 Cantilever noise in the frequency domain

Frequency jitter can be analyzed in the time domain (See Figure 4.3, but the frequency domain is more informative. In this section we describe a method for transferring time-domain fluctuation data into the frequency domain. The practical advantage of this approach is discussed at length in the next section.

Recall the definition of jitter:

$$\delta f_c(t) = f_c(t) - \bar{f}_c, \quad (4.1)$$

Jitter in the time domain and the frequency domain are related by:

$$\langle (\delta f_c(t))^2 \rangle = \int_0^\infty P_{\delta f_c}(f) df, \quad (4.2)$$

where  $P_{\delta f_c}(f)$  is the power spectrum of cantilever frequency noise. A typical frequency fluctuation power spectrum is shown in Figure 4.4(d). The spectrum was obtained by digitizing 25 s of cantilever self-oscillation data and passing it

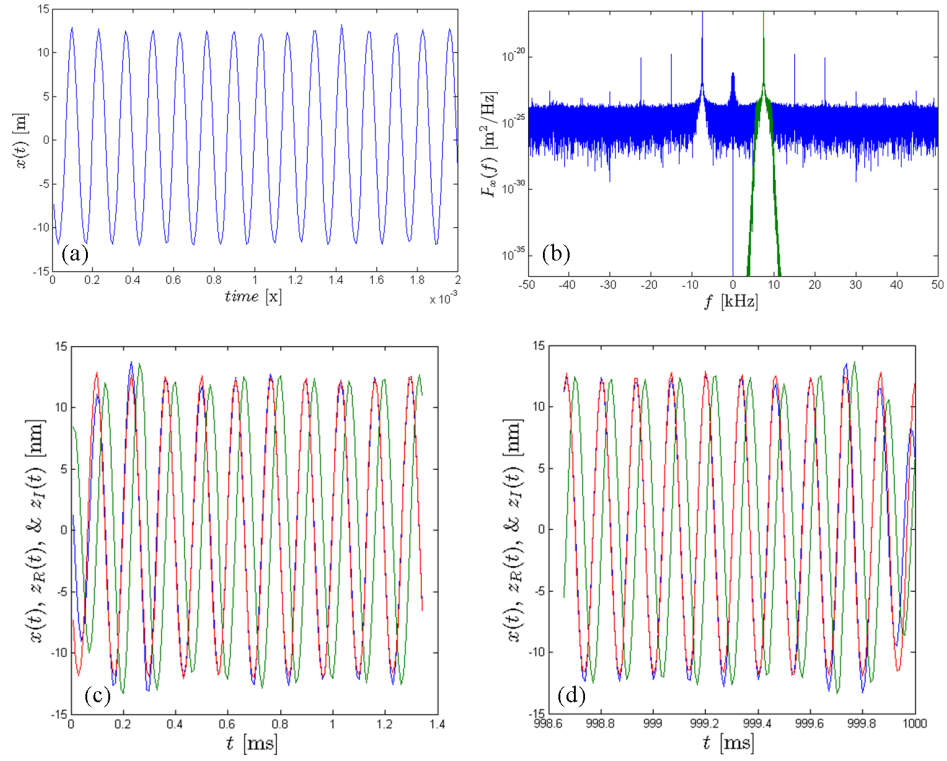


Figure 4.3: Visual algorithm for separating the “raw” data into position and phase components. (a) Cantilever position versus time data (b) Fourier transform of data in (a). For subsequent analysis, everything is discarded except the data in green. (c) and (d) Original data (blue), plotted with in-phase (red) and out-of-phase (green) components of the inverse Fourier transform. Shown at the start and at the end.

through a software frequency-demodulation algorithm. The functioning of the algorithm is summarized below.

A typical example of the cantilever’s position versus time data  $X(t)$  is shown in Figure 4.3 (a). A Hilbert transform is carried out by Fourier transforming  $X(t)$ , bandpass filtering the transformed signal by multiplying it with a 1 kHz wide window centered at the cantilever frequency, discarding the negative half of the Fourier transform. The power spectrum of the data is shown in Figure 4.3 (b), with the filtered region colored green. A  $90^\circ$  phase-shifted copy of the oscillation,  $Y(t)$ , is created via a Hilbert transform. The filtered signal is back

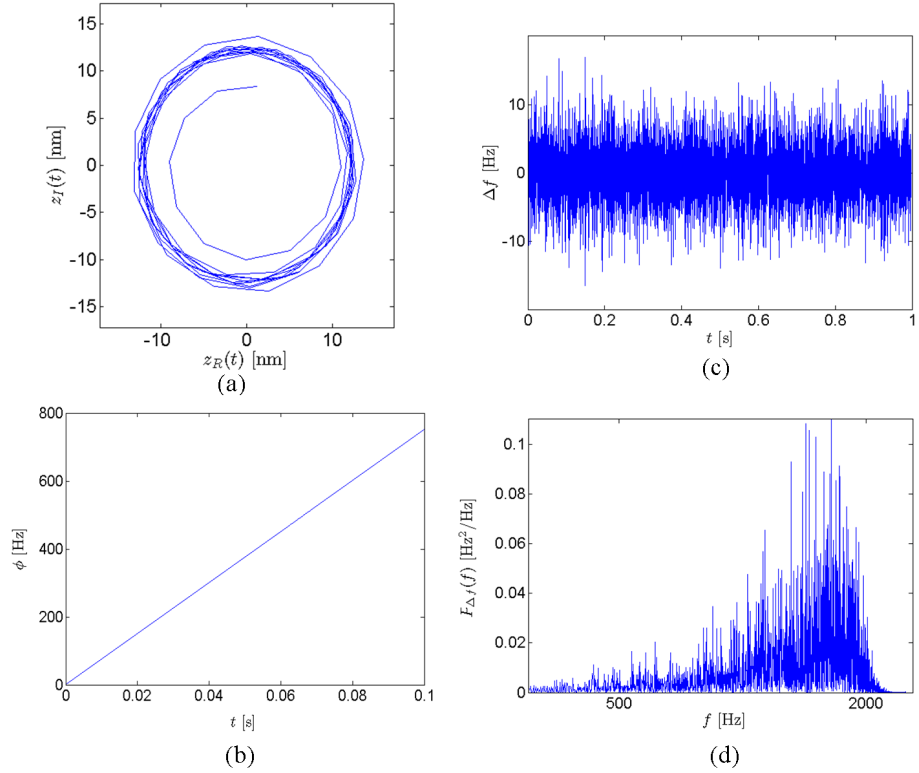


Figure 4.4: Visual algorithm for generating a power spectrum of cantilever frequency fluctuations from the phase versus time data. (a) In-phase component versus out-of-phase component. (b) Phase versus time. The slope of the line is equal to the frequency. (c) Frequency shift versus time (d) Fourier transform of the frequency versus time data.

Fourier-transformed to give  $Z(t) = X(t) + iY(t)$ , as shown in Figure 4.3 (c). The instantaneous cantilever phase was calculated as  $\phi(t) = \frac{\arctan Y/X}{2\pi}$  and the cantilever amplitude  $A(t)$  was calculated from  $A(t) = \sqrt{(X(t)^2 + Y(t)^2)}$ . Here  $X(t)$  is the original oscillation signal multiplied by 1/2 and  $Y(t)$  is the phase-shifted copy of the input oscillation signal, also multiplied by 1/2.

Figure 4.4(a) plots the in-phase versus the out-of-phase components of the signal. The phase versus time data  $\phi(t)$  was broken into 250  $\mu$ s segments and each segment was fit to a line, shown in Figure 4.4(b); the slope of the line is the cantilever frequency  $f_c(t)$ . The time-random fluctuation in the mean frequency,

$\delta f_c(t)$ , is depicted in Figure 4.4(c) and was computed by subtracting the mean  $\bar{f}_c$  frequency from  $f_c(t)$ . This data is Fourier transformed to yield the final result, a power spectrum shown like the one shown in Figure 4.4 (d). The data in Figure 4.4 (d) terminates abruptly at roughly 2000 Hz because a tenth-order Butterworth filter has been applied at half the Nyquist frequency. The effect of the filter is to prevent noise at higher frequencies from folding into the power spectrum and distorting the result. Code for this procedure was developed in MATLAB by Professor John Marohn.

## 4.5 Cantilever frequency noise in the absence of a sample

Figure 4.5 is an average of 100 cantilever frequency fluctuation power spectra, all of which were generated using the method described in Section 4.4. The data used to generate the power spectrum were obtained using a custom fabricated (the fabrication process is described in Appendix B) cantilever which was driven to oscillate at  $x_{\text{rms}}=57$  nm. The cantilever had a spring constant  $k$  of  $4 \times 10^{-3}$  N/m, a Q of  $1660 \pm 60$  and a resonance frequency  $f_c$  of 7073 Hz.

There was no sample in the microscope and the cantilever simply was allowed to oscillate in high vacuum; 4 s of oscillation data were collected. In the absence of a sample or other perturbation,  $P_{\delta f_c}$  is equal to the sum of the frequency noise arising from thermo-mechanical (Brownian) motion and noise from the detector:

$$P_{\delta f_c}^{\min} = P_{f_c}^{\text{therm}} + P^{\text{det}} f^2, \quad (4.3)$$

where

$$P_{f_c}^{\text{therm}} = \frac{k_B T}{2\pi^2 x_{\text{rms}}^2 k_c \tau}, \quad (4.4)$$

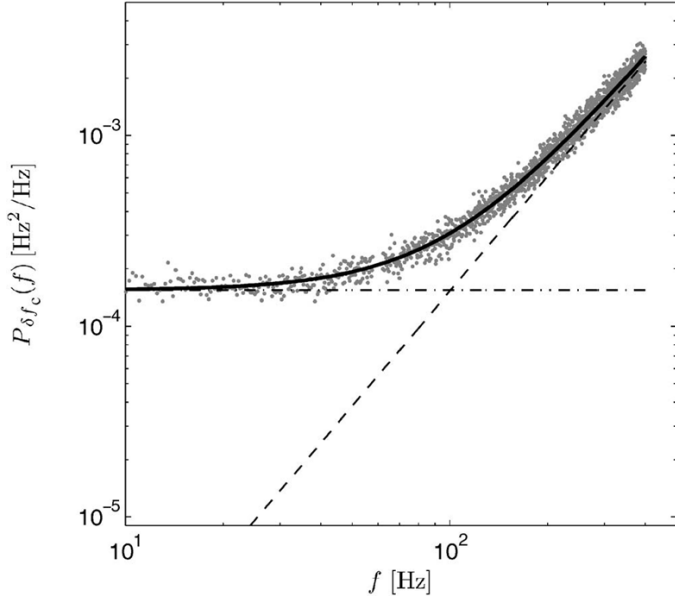


Figure 4.5: Power spectrum of frequency noise in the absence of a sample (gray dots). The solid line is a fit to Eq.( 4.3). The dashed line (thermo-mechanical noise) plots Eq. (2.1), Both axes are logarithmic. At higher frequencies, the spectral density of cantilever frequency fluctuations increases quadratically due to detector noise. The cantilever's self-oscillation amplitude was  $x_{rms}=57$  nm.

and

$$p^{\text{det}} = \frac{P_{\delta x}^{\text{det}}}{x_{rms}^2}, \quad (4.5)$$

where  $P_{\delta x}^{\text{det}}$  is the position noise power spectrum. These two sources of noise are uncorrelated, and account quantitatively for the entire power spectrum of cantilever frequency fluctuations in Figure 4.5.

The thermo-mechanical noise  $P_{f_c}^{\text{therm}}$  is “white” (independent of frequency) and its magnitude is determined by the temperature, the amplitude of the cantilever’s oscillation, the spring constant  $k_c$  and the ringdown time  $\tau$ . The ringdown time is the time required for the cantilever’s amplitude to decay to  $1/e$  of its initial value when the driving force is abruptly discontinued. Eq.( 4.4) is derived in Ref. [83] and in Ref. [50].

The detector noise  $P_{\text{det}}$  is quadratic in frequency; this dependence arises from the conversion from position fluctuations to frequency fluctuations.  $P_{\text{therm}}$  and  $P_{\text{det}}$  are both inversely proportional to the mean-squared amplitude of the driven cantilever.

Eq.( 4.3) quantitatively accounts for the entire power spectrum of frequency noise shown in Figure 4.5. The intersection of the dash-dot and the dotted line represents the frequency,  $f_{\text{therm}}$ , at which the contributions to the noise power spectrum from thermo-mechanical noise and detector noise are equal. The agreement between data and the functional form of Eq.( 4.3) at frequencies  $f$  lower than  $f_{\text{therm}}$  is significant. It is significant because it confirms that for frequencies lower than  $f_{\text{therm}}$ , the detection limit of the measurement is set by Brownian motion and not by detector noise. However, the sensitivity of the instrument degrades sharply (proportional to  $f^2$ ) when  $f > f_{\text{therm}}$ . We found that  $f_{\text{therm}}$  typically falls around 1000 Hz.

## 4.6 Cantilever frequency noise over a thin polymer film

In Section 4.5, we showed that in the absence of a sample, the cantilever frequency noise spectrum consists entirely of contributions from the detector and from the cantilever's Brownian motion and can be completely predicted from Eq. (4.3). In this section, we show that when the tip-sample separation falls below a certain threshold, Equation 4.3 ceases to describe the power spectrum.

This result is illustrated in Figure 4.6, a plot of frequency fluctuations over a 200 nm thick film of PMMA for a cantilever near to ( $d = 25$  nm) and far from ( $d = 2000$  nm) the surface. Fluctuations are shown in both the time (a,b) and

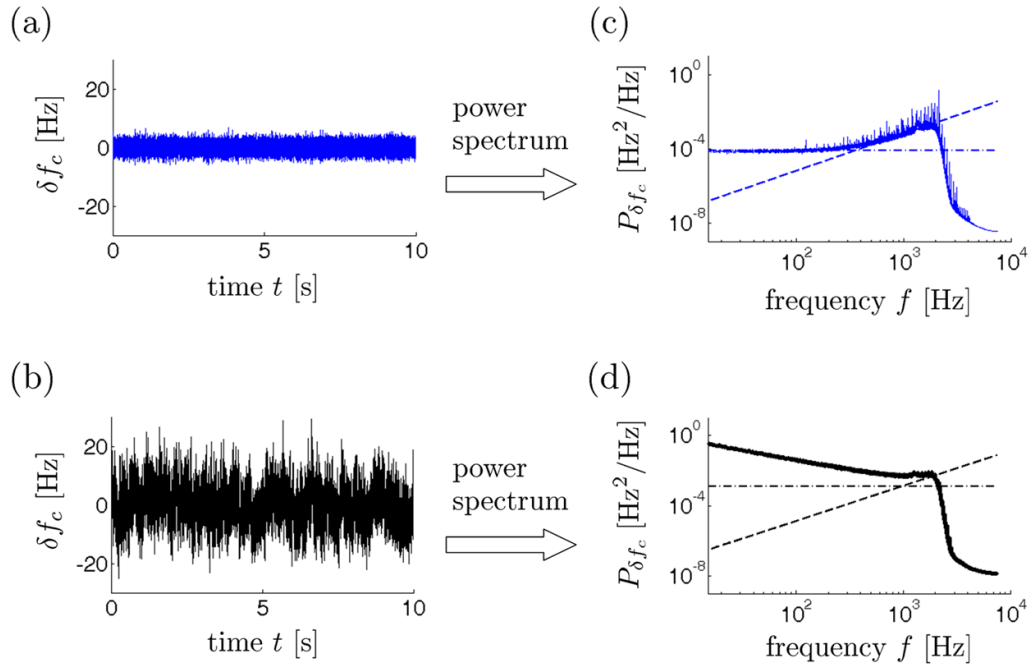


Figure 4.6: Cantilever frequency fluctuations over a 200 nm thick film of PMMA at large tip-sample separation ( $d = 2000$  nm, upper panels, blue data) and small tip-sample separation ( $d = 25$  nm, lower panels, black data). (a,b) Cantilever frequency fluctuations in a 2100 Hz bandwidth centered at the cantilever frequency. (c,d) Power spectra of cantilever frequency fluctuations. The lines show contributions to the cantilever frequency-fluctuation power spectra from detector noise (dashed) and thermo-mechanical position fluctuations (dot-dashed). Here  $f_c = 4158$  Hz,  $k_c = 0.87$  mN/m, and  $Q(d = 2000 \text{ nm}) = 4700$  while  $Q(d = 25 \text{ nm}) = 500$ . The dot-dashed lines were computed using these values and Eq.( 4.4). The dashed line was computed from Eq.( 4.5) using the measured detector noise  $P_{\delta x}^{\text{det}}(d = 2000 \text{ nm}) = 3.3 \times 10^{-6} \text{ nm}^2/\text{Hz}$  and  $P_{\delta x}^{\text{det}}(d = 25 \text{ nm}) = 6.6 \times 10^{-6} \text{ nm}^2/\text{Hz}$ . The cantilever amplitude was  $x_{\text{rms}} = 70$  nm-rms and the tip-sample voltage was  $V_{\text{ts}} = \phi + 0.5$  V where  $\phi = -0.1$  V is the measured contact potential difference between the tip and the underlying gold substrate.

frequency domains (c,d). The data of Figure 4.6 (a) and (b) show that when the tip-sample separation is decreased from  $d=2000$  to  $d=25$  nm, the rms fluctuation in the cantilever frequency increases over four-fold. The remainder of this chapter is devoted to exploring the origins of this increase. Figures 4.6(c) and (d) depict the same data in the frequency domain and were generated using the

method described in Section 4.4.

We attempted to fit both power spectra to Eq.( 4.3). The excellent fit of the power spectrum acquired at  $d=2000$  nm to Eq.( 4.3) confirms that at this distance, the interaction between the tip and the sample is negligible. We can conclude from Figure 4.6 (c) that at  $d=2000$  nm, the cantilever is insensitive to the presence of the polymer film and all frequency fluctuations arise either from detector noise or from Brownian motion.

By contrast, the data of Figure 4.6 (d), acquired at a height  $d=25$  nm from the surface of the polymer film, cannot be described by Eq.( 4.3). We may conclude that when the tip and the sample are in close proximity, there is an additional source of frequency fluctuations. At low frequencies ( $< 1000$  Hz), the fluctuations have a power spectrum over  $10^2$  times larger than the thermo-mechanical and detector contributions. We attribute this excess frequency noise to interaction between the tip and the sample. According to the central hypothesis of Chapter 3, the excess fluctuations in the cantilever's frequency originate from dielectric fluctuations within the polymer.

## 4.7 Bandwidth

In principle, the information contained within the frequency domain and the time domain is identical:

$$\langle (\delta f_c(t))^2 \rangle = \int_0^\infty P_{\delta f_c}(f) df, \quad (4.6)$$

In the physical world, however, all measurements occur in a finite bandwidth, and the limits of integration cannot be infinite. We redefine the integration limits

accordingly:

$$\langle (\delta f_c(t))^2 \rangle \approx \int_{f_L}^{f_U} P_{\delta f_c}(f) df, \quad (4.7)$$

Here  $f_L$  and  $f_U$  are respectively the lower and upper limits of the measurement in frequency space. The bandwidth  $b$  of the measurement,  $f_U - f_L$ , is selected so that it captures the bulk of the integral of the power spectrum, but excludes detector noise. The data of Figure 4.6 (d) indicate that a bandwidth of 100 Hz excludes the vast majority of the detector noise, but captures most of the area under the power spectrum. Henceforth we shall use the term “jitter” to refer to the finite-bandwidth integral of the power spectrum.

## 4.8 Amplitude dependence of jitter

Figure 4.7 contains further support for our hypothesis that the power spectrum at large tip-sample separation can be characterized by a sum of contributions from Brownian and detector noise, but the power spectrum at small-tip sample separation cannot. Both  $P_{f_c}^{\text{therm}}$  and  $p^{\text{det}}$  are proportional to  $1/x_{\text{rms}}^2$ , where  $x_{\text{rms}}$  is the rms amplitude of the driven cantilever. If Brownian motion and detector noise are the only contributors to frequency noise, then a log-log plot of rms cantilever amplitude versus jitter should have a slope of -2. Figure 4.7 (a) is a plot of jitter versus rms oscillation amplitude at a height  $d=2000$  nm over a 200 nm thick PMMA film. The solid line on the log-log plot has a slope of -2, confirming that as predicted by Eq.( 4.3), jitter is proportional to  $1/x_{\text{rms}}^2$ . By contrast, Figure 4.7 (b) plots jitter versus rms oscillation amplitude for  $d=25$  nm. At amplitudes between 50 and 150 nm, jitter does not have a slope of -2; in fact, it is essentially constant.

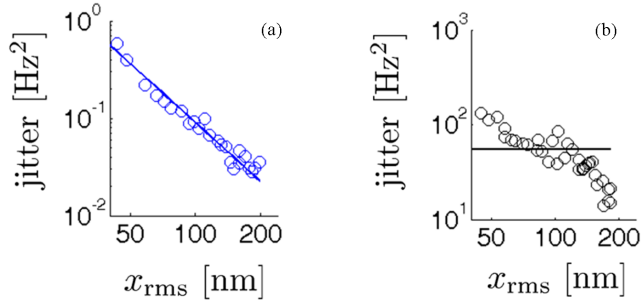


Figure 4.7: Cantilever frequency jitter in a 100 Hz bandwidth versus root-mean-square cantilever amplitude over a 200 nm thick film of PMMA at (a) 2000 nm from the surface and at (b) 25 nm from the surface.

## 4.9 Dependence of jitter on tip charge

In Chapter 3, we presented a theory which postulated that cantilever frequency fluctuations over polymers can arise from dielectric relaxation processes. In this section, we test one of the key assumptions of this hypothesis – that the tip-sample system may be described by linear response. The analysis of Section 3.5 predicts that jitter is parabolic in tip charge  $q_c$ :

$$\langle (\delta\omega_c)^2 \rangle = \left( \frac{q_c^2}{4m^2\omega_c^2} \right) C_{xx,xx}(0). \quad (4.8)$$

Assuming that the tip/vacuum/dielectric epitaxial gold system behaves as a capacitor, tip charge can be calculated from  $q_c = C(V_{ts} - \phi)$ , where  $V_{ts}$  is the voltage applied between the tip and the sample, and  $C$  is the tip-sample capacitance. Our methods for measuring the tip-sample capacitance are described in Appendix D. Here  $\phi$ , the tip-sample contact potential difference, is defined as the electric potential difference between the vacuum levels of two metals in close proximity.

We would thus expect a plot of  $V_{ts}$  versus jitter to be a parabola centered at  $\phi$  with a curvature proportional to the tip-sample capacitance. The contact

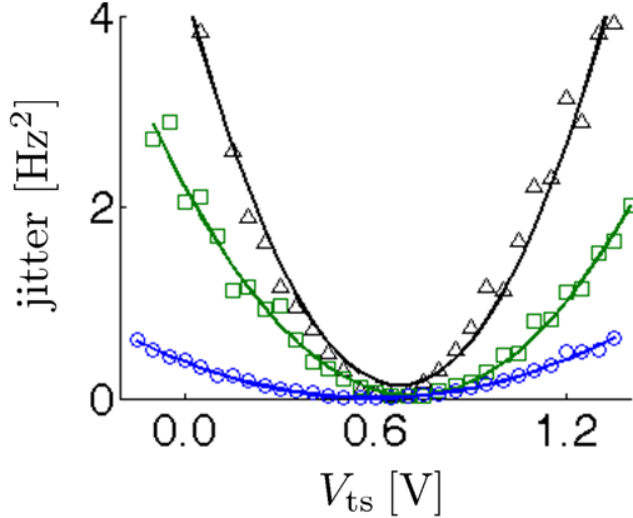


Figure 4.8: Frequency jitter versus tip-sample voltage over a 466 nm thick PMMA film at various heights. Data (points) and parabola fits (lines) are shown for tip-sample heights of  $d=75$  nm (black triangles),  $d=100$  nm (green squares) and  $d=250$  nm (blue circles). The cantilever amplitude was  $x_{\text{rms}}=75$  nm and the cutoff frequencies, as defined in Eq. 4.7 were  $f_L=0$  Hz and  $f_U=100$  Hz.

potential  $\phi$  is defined as the difference between the work function of the tip and the work function of the sample and is discussed in greater detail in Section 4.13. The data of Figure 4.8, a plot of frequency jitter versus tip-sample voltage for a cantilever at various heights over a thin film of PMMA, confirm that jitter is indeed a quadratic function of the applied voltage  $V_{\text{ts}}$ . We also note that the contact potential  $\phi$  appears to exhibit a slight height dependence.

The quadratic dependence of jitter on voltage confirms a key assumption of our theory, that cantilever frequency fluctuations can be calculated using linear-response theory. The increase in the curvature of the parabolas with increasing tip-sample proximity is consistent with the hypothesis that the curvature of the parabola is proportional to capacitance (which likewise increases with tip-sample proximity).

## 4.10 Comparison of predicted and measured power spectra

In Section 3.9, we derived an exact expression for the dependence of the cantilever frequency noise power spectrum over polymers on the dielectric spectrum, the film thickness, the tip-sample separation and the tip charge  $q_c$ :

$$P_{\omega_c}(\omega) \approx \frac{3q^2 k_B T J_4(0)}{4m^2 \omega^2 d^5 (\epsilon'(0) + 1)^2} \left( \frac{\epsilon''(\omega)}{\omega} \right). \quad (4.9)$$

where

$$I_n(\omega) \equiv \int_0^\infty dq q^n e^{-2q} \left( \frac{1 - e^{-4q(h/d)}}{1 + \zeta(\omega) e^{-2q(h/d)}} \right), \quad (4.10)$$

$$\zeta(\omega) \equiv \frac{\epsilon(\omega) - 1}{\epsilon(\omega) + 1}. \quad (4.11)$$

It is helpful to the experimentalist to consider the equation in *Système International* (SI) units. The power spectrum of the frequency jitter, rewritten in terms of experimentally relevant quantities and in SI units, is

$$P_{\delta f_c}(f) = \frac{3k_B T q_c^2 f_c^2 \text{Im}\zeta(2\pi f)}{64\pi^2 \epsilon_0 k_c^2 d^5} \frac{1}{f} \int_0^\infty dq q^n e^{-2q} \left( \frac{1 - e^{-4q(h/d)}}{1 + \zeta(2\pi f) e^{-2q(h/d)}} \right) \quad (4.12)$$

where  $f_c$ ,  $k$ , and  $q_c$  are cantilever resonance frequency, spring constant, and charge, respectively, and

$$\zeta(2\pi f) = \frac{\epsilon(2\pi f) - 1}{\epsilon(2\pi f) + 1}, \quad (4.13)$$

We proceed to compare the measured  $P_{\delta f_c}$  to the theoretical  $P_{\delta f_c}$  predicted by Eq. (4.12). However, it is first necessary to clarify all of the input parameters to Eq. (4.12). The tip charge  $q_c$  and the dielectric spectrum are particularly non-trivial quantities.

## 4.11 Inputs to the theory: capacitance, dielectric spectra and contact potential

The tip charge  $q_c$  is governed by the capacitance between the tip and the sample, a quantity which depends strongly on the tip-sample distance. Because the measurement is carried out at constant tip-sample voltage  $V_{ts}$  [13, 61],  $q_c$  varies with  $d$  and must be determined at each height using the probe-sample capacitance  $C$  and  $q_c = C V_{ts}$ . Following the method described in Ref. [13], we determined this capacitance by approximating the charged tip of the probe by a sphere of radius  $R = 70$  nm located a distance  $d$  above a dielectric slab of thickness  $h$  backed by a conductor,

$$C = 4\pi\epsilon_0 R \sum_{n=1}^{\infty} \frac{\sinh(\alpha)}{\sinh(n\alpha)}, \quad (4.14)$$

$$\alpha = \cosh^{-1} \left( 1 + \frac{d}{R} + \frac{h}{\epsilon'(0)R} \right). \quad (4.15)$$

In the limit  $\epsilon'(0) \rightarrow 1$ , this expression is exactly correct for a sphere of radius  $R$  with center a distance  $R + d + h$  above a conducting plane [84, 85]. The replacement of  $h$  with  $h/\epsilon'(0)$  is correct for a dielectric layer of thickness  $h$  within a parallel plate capacitor. The dielectric constant-dependent correction in Eq. (4.15) approximately accounts for the dielectric in the present configuration.

Dielectric spectra were measured for bulk (thicker than 450 nm) samples of PMMA and PVAc by Kuehn [47]. The dielectric spectrum of polystyrene can be difficult to measure because polystyrene is a low loss material. The impedance analyzer at Cornell (Hewlett-Packard; Model No. 4192 A LF) was not sufficiently sensitive to acquire dielectric spectrum of polystyrene. Polystyrene spectra were kindly provided by Professor Ranko Richert. A complete description

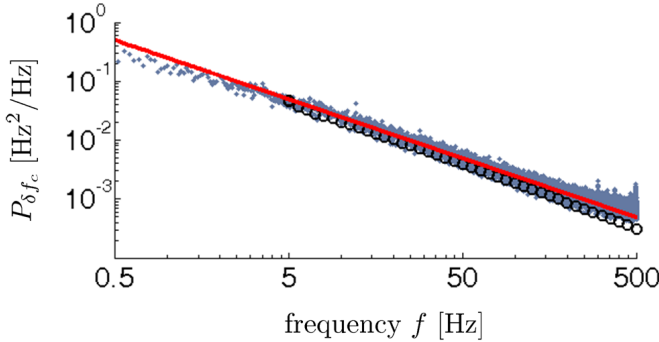


Figure 4.9: Observed and calculated power spectrum of cantilever frequency fluctuations at height  $d = 100$  nm over a 200 nm thick PMMA film. The small blue-gray dots are the observed spectrum. The large black circles are the spectrum calculated from Eq. (4.12), the measured dielectric spectrum and the tip-sample capacitance model discussed in the text. The red line shows a  $1/f$  spectrum, as a guide to the eye. Applied voltage  $V_{ts} = 0.5$  V +  $\phi$  with  $\phi = -0.1$  V; and  $x_{rms} = 70$  nm-rms, the number of averages was 50, and the acquisition time is 25 seconds.

of the dielectric spectroscopy data used in this experiment is contained in Appendix D.

The data of Figure 4.8 clearly show that jitter depends strongly on the applied tip-sample voltage (and thus the tip charge  $q_c$ ). The theoretical jitter also depends on  $q_c$ . In order to ensure that comparisons between theory and experiment were made at identical  $q_c$ , we carefully recorded the contact potential prior to every measurement. We obtained the contact potential  $\phi$  in the manner described in Section 4.9.

Figure 4.9 is a comparison of theory to experiment. The plot shows the theoretical and measured  $P_{\delta f_c}$  at a height  $d = 100$  nm above a 200 nm thick PMMA film. The measured and calculated curves agree within a factor of two over more than two decades of frequency. A  $P_{\delta f_c} \propto 1/f$  line is plotted as a guide to the eye. The cantilever frequency-fluctuation power spectrum is well approximated as a  $1/f$  spectrum for frequencies in the 5 to 500 Hz range, with small deviations

from  $1/f$  behavior apparent only below  $f \approx 5$  Hz. The theoretical curve does not extend below 5 Hz because one of the inputs to the theory is the dielectric spectrum; our instrument at Cornell was incapable of reliable measurements below 5 Hz. Thus Eq. (4.12), which contains no free parameters, quantitatively accounts for the cantilever frequency noise spectrum over a thin polymer film.

## 4.12 Theory versus experiment

Figure 4.10 is the central result of Chapters 3 and 4. In Fig. 4.10 we use the measured contact potential, estimated capacitance, measured dielectric spectrum, and Eq. (4.12) and Eq. (4.7) to predict jitter in a bandwidth from 5 to 100 Hz as a function of tip-sample separation  $d$ .

In computing tip charge, we found it necessary to account for the height dependence of the contact potential  $\phi$  shown in Fig. 4.8, as follows. In each sample  $\phi$  was measured at 4 to 10 selected heights. Over the six samples studied at heights from  $d = 10$  nm to over 200 nm, the observed  $\phi$  ranged from 0.29 V to 0.95 V. In any one sample, a variation of  $\leq 0.2$  V was seen. In each sample, a high, low, and average contact potential ( $\phi_{\text{high}}$ ,  $\phi_{\text{low}}$ , and  $\phi_{\text{avg}}$ ) were identified. The applied voltage was set to  $V_{\text{ts}} \approx 0.5$  V +  $\phi_{\text{avg}}$ . To account for the observed variation in contact potential, for each sample two theory curves are calculated: one with  $\phi = \phi_{\text{low}}$  and one with  $\phi = \phi_{\text{high}}$ . In Fig. 4.10 the region between these two curves is colored yellow.

Six samples were studied: films of PMMA, PVAc, and PS of thickness  $h = 40$  nm and  $h = 450$  nm. The theory correctly predicts the magnitude of the observed jitter and its dependence, qualitatively, on distance. The theory also

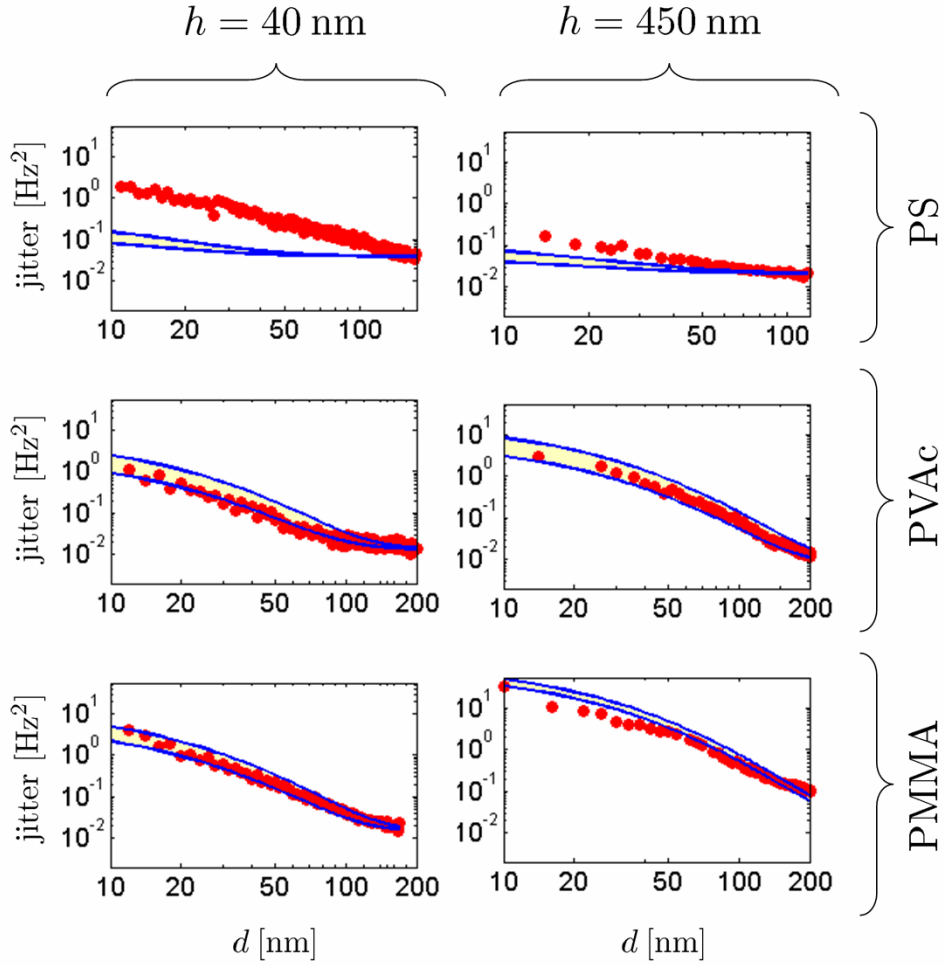


Figure 4.10: Dependence of jitter on tip-sample separation for six polymer films. The film composition and thickness are indicated in the figure. The red dots are the jitter obtained from the measured power spectrum using  $f_L = 5$  Hz and  $f_U = 100$  Hz. The yellow regions are the predicted jitter, calculated as discussed in the text. The applied voltage was  $V_{ts} \approx 0.5$  V +  $\phi_{avg}$  where  $\phi_{avg}$  is the height-averaged contact potential, measured independently in each sample. The cantilever amplitude was  $x_{rms} = 70$  nm-rms,  $N_{avg} = 50$ , and the acquisition time was 1 second.

correctly predicts whether the thick film or the thin film of the same composition will have the larger jitter at close separation. This prediction cannot be made without a detailed calculation: the electric field gradient fluctuations are largest over the thick film, but at fixed tip-sample voltage the tip charge is less over the thick film and so the fluctuations couple less well to the cantilever; differences in  $k_c$  must also be accounted for.

The agreement between theory and experiment is poorest in polystyrene, where theory underestimates the jitter observed at close separations by a factor of three in the thick film and by a factor of ten in the thin film. It is not surprising that of the three samples, polystyrene would show the worst agreement. The  $\epsilon''$  in polystyrene is very small and notoriously difficult to measure, and is likely therefore more sensitive to sample preparation than either PMMA and PVAc. Although we were able to obtain  $\epsilon'$  and  $\epsilon''$  for polystyrene of molecular weight comparable to ours [86], the sample was not identical to that used in our cantilever measurements. Treating these constants as adjustable parameters does not yield a dielectric function that reproduces the PS data for both thin and thick films with the same level of agreement shown for PVAc and PMMA. This suggests that dielectric fluctuations in the thin PS film are not well represented by bulk dielectric relaxation processes alone.

For the four PMMA and PVAc films, where  $\epsilon'$  and  $\epsilon''$  could be measured in identically prepared samples, the measured and predicted jitter are in quantitative agreement. The magnitude of the jitter and its dependence on tip-sample separation is correctly predicted over two decades of jitter in both of these samples. The agreement between theory and measurement in Figure 4.10 confirms [45, 20] that the jitter measurement probes low frequency polymer motions. In

PMMA, for example, these low frequency motions include hindered rotations of polar side groups [87].

### 4.13 The contact potential

To attain a more thorough understanding of the contact potential, we studied non-contact friction and the static frequency shift, which are also quadratic in applied tip-sample voltage. The contact potential is the primary observable in most electric force microscopy experiments. It is a useful quantity because it can be a direct indicator of the surface charge density. Silveira *et al.* [31], for instance, extracted the contact potential from frequency parabolas to directly observe the transition from Ohmic to space-charge limited conduction in an organic semiconductor.

Figure 4.11 (a) is a plot of simultaneously acquired jitter, non-contact friction coefficient  $\Gamma$  and frequency  $f_c$  as a sample of tip-sample voltage  $V_{ts}$ . The sample is 200 nm PMMA. The contact potentials obtained by fitting the jitter and  $\Gamma$  data to parabolas are statistically equivalent (respectively,  $-0.14 \pm -0.02$  V and  $-0.13 \pm -0.04$  V). In principle, the measurement of cantilever frequency should yield a contact potential equivalent to that obtained from the previous two methods. However, the contact potential inferred from the  $f_c$  versus  $V_{ts}$  curve is  $\phi_{f_c} = -1.02 \pm -0.03$  V, which is twenty four standard deviations away from the values obtained for  $\phi_{\text{jitter}}$  and  $\phi_\gamma$ . We speculate on the possible origins of this discrepancy in the next section.

We measured  $\phi_{\text{jitter}}$ ,  $\phi_\Gamma$  and  $\phi_{f_c}$  as a function of tip-sample separation for separations ranging from  $d=25$  nm to  $d=500$  nm. The results are summarized in Fig-

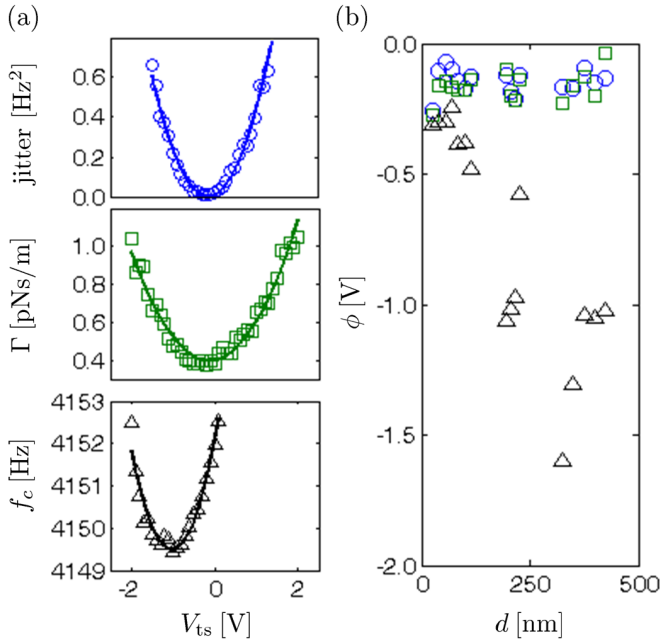


Figure 4.11: Simultaneously acquired jitter (blue circles), noncontact friction coefficient  $\Gamma$  (green squares), and cantilever frequency  $f_c$  (black triangles) vs tip-sample voltage  $V_{ts}$  at a height  $d=100$  nm over a 200 nm thick film of PMMA. Solid-lines are parabolic fits. (b) The voltage at the parabola minimum,  $\phi$ , as measured from the jitter (blue circles), noncontact friction coefficient (green squares), and frequency (black triangles) parabolae. The cantilever amplitude was  $x_{rms}=70$  nm; jitter was measured in a 100 Hz bandwidth ( $f_L=0$  Hz and  $f_U=100$  Hz).

ure 4.11 (b). The contact potentials extracted from jitter and non-contact friction parabolas agreed within 0.1 V and were essentially independent of tip-sample separation. However, this was not the case for  $\phi_{f_c}$ . The contact potential obtained from analyzing the frequency shift,  $\phi_{f_c}$ , agrees with  $\phi_{\text{jitter}}$  and  $\phi_{\Gamma}$  only at very small tip-sample separations. At large tip-sample separations, it differs from  $\phi_{\text{jitter}}$  and  $\phi_{\Gamma}$  by as much as 1.5 Volts. In Ref. [62], Rast *et al.* also observed a large height-dependent shift in contact potential in their measurements of frequency versus  $V_{ts}$  over thin gold films in ultra-high vacuum. They attributed the shift to either patch charges on the gold or to surface contamination. Unfortunately, neither of these hypotheses explains the large discrepancy between

$\phi_{f_c}$  and  $\phi_{\text{jitter}}$  or  $\phi_\Gamma$ . An alternative hypothesis is that the frequency measurement is more sensitive to the presence of charge on the silicon body of the cantilever (which has a different work function from the platinum tip), than are the measurements of friction and jitter.

## 4.14 Origin of the parabolic dependence of friction and frequency on tip charge

Stipe *et al.* [12] showed that sample-induced cantilever non-contact friction follows a fluctuation dissipation relation:

$$\Gamma = \frac{q^2 S_E(f_c)}{4k_B T}, \quad (4.16)$$

where  $q_c$  and  $\phi$  were defined in Section 4.9,  $k_B$  is Boltzmann's constant,  $T$  is the temperature, and  $S_E(f_c)$  is the power spectrum of the electric field fluctuations at the cantilever's resonance frequency arising from the sample. Figure 4.11 clearly shows that  $\Gamma$  is proportional to  $V_{ts}^2$ , confirming that non-contact friction is governed by the fluctuation-dissipation theorem of Eq.(4.16). The results for jitter and friction shown in Figure 4.11 are highly typical. We have consistently observed that both of these quantities are quadratic in applied tip-sample voltage; we have also noted that without exception, the sign of the resulting parabola is positive, and that the quality of the parabolic fits improves with increasing tip-sample proximity. The nature of the relationship between frequency shift and tip-sample voltage is less clear. Stowe [51] gives the following expression for the cantilever frequency shift in the vertical geometry in the presence of a sample:

$$\delta f = \frac{f_0}{2k_c} \left( \frac{\partial F_x}{\partial x} \right) - \frac{F_z}{l} - \frac{\partial F_z}{\partial z} \theta^2 - 2 \frac{\partial F_z}{\partial x} \theta, \quad (4.17)$$

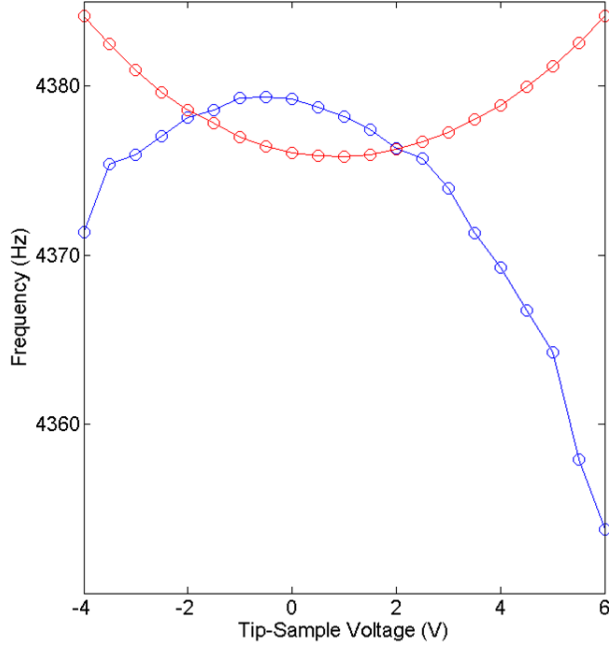


Figure 4.12: Frequency shift versus applied tip voltage over epitaxial gold at 50 nm from the surface (blue circles) and 1000 nm from the surface (green circles).

where  $\vec{F} = (F_x, F_y, F_z)$  is the force on the tip,  $x$  is the direction of the cantilever's motion,  $l$  is the length of the cantilever,  $k$  is the cantilever's spring constant,  $f_c$  is the cantilever's resonance frequency, and  $\theta$  is the angle between the cantilever and the normal to the surface. Figure 4.14 is an illustration of these competing forces. In the absence of significant angular misalignment, contributions from the latter two terms are expected to be minimal.  $F_z/l$  is the force pulling the cantilever toward the surface, and has been calculated to be significantly smaller than  $F_x$ . It is thus unlikely that  $F_z$  contributes significantly to the frequency shift. Thus  $\frac{\delta F_x}{\delta x}$ , which accounts for the sample's spatial or electrical heterogeneity, is expected to dominate. Given that  $\partial F_x/\partial x = q\partial E_x/\partial x$  and  $\partial E_x/\partial x \equiv E_{xx}$ , it is clear that this is the same term predicted in Section 3.4 to give rise to cantilever jitter:

$$\Delta\omega_c = -\frac{q_c f_c}{k_c} E_{xx}, \quad (4.18)$$

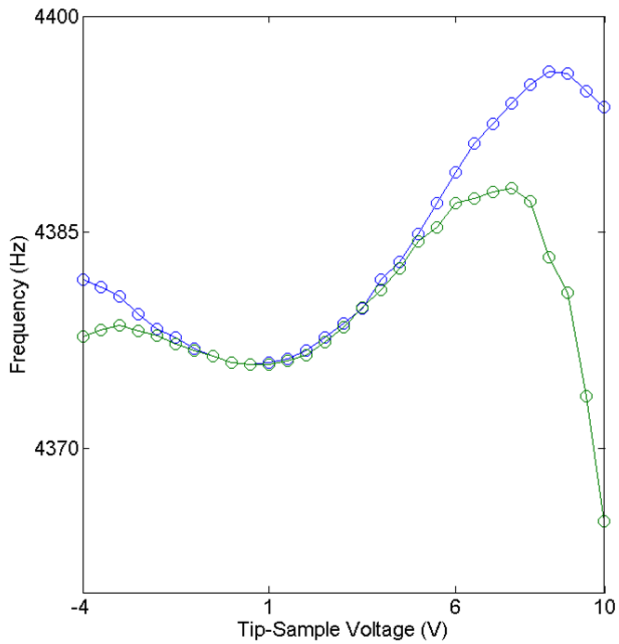


Figure 4.13: Frequency shift versus applied tip voltage over epitaxial gold at 350 nm from the surface (blue circles) and 250 nm from the surface (red circles).

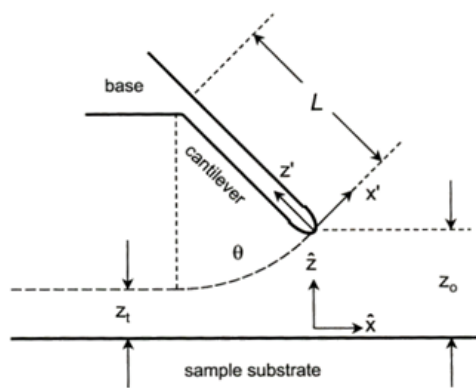


Figure 4.14: Depiction of the forces acting on a cantilever oscillating parallel to the sample surface. Figure is reproduced from Ref. [51].

If this is indeed the case, then Eq. (4.18) clearly suggests that the sign of the frequency shift versus tip sample voltage parabola should be positive. Our experiments show that the dependence is usually parabolic, but as demonstrated in Figure 4.12, the sign of the parabola can be variable. We have also observed non-parabolic behavior. Figure 4.13, a plot of frequency shift versus tip-sample voltage over epitaxial gold at two different tip-sample separations, shows the relationship between tip charge and frequency is not always quadratic.

It is possible that the inverted parabolas arise from contributions from other terms in Eq. (4.18). The most likely candidate is the pendulum term, which is also quadratic in  $V_{ts}$  (see Eq. (4.19) below), but is opposite in sign to  $\frac{\delta F_x}{\delta x}$ . If the epitaxial gold-on-mica sample is truly atomically flat, then the magnitude of  $\frac{\delta F_x}{\delta x}$  is likely to be small.  $F_z$ , on the other hand, is likely to be less sensitive to the homogeneity of the sample (unless the surface contains patch charges), but more sensitive to the tip-sample separation. This hypothesis is consistent with the observation that the inversion is observed only at small tip-sample separations. If we approximate the tip/vacuum/dielectric/gold system as a parallel plate capacitor, then

$$F_z = -\frac{1}{2} \frac{dC}{dz} V_{ts}^2, \quad (4.19)$$

where  $C$  is the tip-sample capacitance. As the tip-sample distance decreases, the magnitude of  $F_z$  increases, and thus  $F_z$  might be expected to dominate in spatially homogeneous samples when  $d$  is small - as we observed for epitaxial gold. Unfortunately, this hypothesis does not explain the data of Figure 4.13, where the dependence of frequency on  $V_{ts}$  is clearly not parabolic. Eq. (4.18), which is entirely parabolic in  $V_{ts}$ , may thus not provide a complete description of frequency shift.

## 4.15 Additional sources of jitter: cantilever anharmonicity

Although the excellent agreement between theory and experiment observed in Figure 4.10 strongly suggests that any heretofore unmentioned sources of jitter are probably negligible, we have carried out further experiments and calculations to prove it.

If the cantilever's potential energy contains an anharmonic perturbation, then force fluctuations acting in concert with the anharmonic potential lead to additional frequency noise [14]. An anharmonicity could arise from intrinsic cantilever nonlinearities or, alternatively, from tip charge interacting with the field derivative  $\partial^2 E_x / \partial x^2$  expected to be present near a film of randomly oriented dipoles. Therefore an anharmonicity could be a function of sample composition, tip location and tip-sample separation height. To measure the anharmonicity, we note that adding a cubic term  $V_a = -\alpha x^3/6$  to the potential energy of a harmonic oscillator leads to a negative fractional frequency shift which depends on oscillator drive amplitude according to [88],

$$\frac{\Delta f_c}{f_c} = -\frac{5}{24} \left( \frac{\alpha x_{\text{rms}}}{k_c} \right)^2. \quad (4.20)$$

Figure 4.15 presents a measurement of cantilever frequency as a function of drive amplitude for a charged cantilever at a height  $d = 50$  nm over a 40 nm thick PMMA film. Because the frequency in Figure 4.15 increases rather than decreases with amplitude, we conclude that the frequency dependence does not stem from a cubic, but rather from a quartic (or higher order) perturbation to the cantilever potential. A quartic perturbation,  $V_b = \beta x^4/4$ , results in a frequency shift,

$$\frac{\Delta f_c}{f_c} = \frac{3}{4} \frac{\beta x_{\text{rms}}^2}{k_c}. \quad (4.21)$$

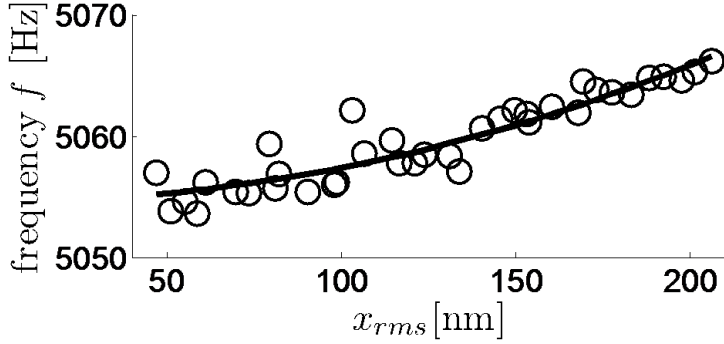


Figure 4.15: The dependence of cantilever frequency on drive amplitude at height  $d = 50$  nm over a 40 nm thick PMMA film with  $V_{ts} = 0.5$  V +  $\phi$  with  $\phi = 0.8$  V. The line is a best fit to Eq. 4.21.

Fitting the data in Figure 4.15 to Eq. (4.21), we find  $\beta/k_c = 7 \times 10^{-8}$  nm<sup>-2</sup>. To quantify this perturbation, we compare the energy of the anharmonic term to that of the unperturbed (harmonic) potential energy  $V_h = k_c x^2/2$ . At the peak of the cantilever oscillation, the ratio of these energies is,

$$r_b = \frac{V_b}{V_h} = \frac{\beta x_{\text{rms}}^2}{k_c} \quad (4.22)$$

For a typical rms cantilever amplitude of 100 nm, we find that  $r_b = 7 \times 10^{-4} \ll 1$ . Therefore our cantilever is well represented by a harmonic oscillator. Although a measurable cantilever anharmonicity is present near a polymer surface, it appears to be a negligible source of cantilever frequency fluctuations in the polymers studied here.

## 4.16 Sensitivity

The fabrication of custom single-crystal silicon cantilevers is an expensive and time-consuming process. We use these cantilevers because they improve the sensitivity of the measurement by over three orders of magnitude relative to a commercial cantilever. This is explicitly calculated below.

Let us define a spectral density of electric field gradient fluctuations  $P_{\delta E_{xx}}$  and rewrite  $P_{\delta f_c}$  (Eq.( 4.12)) in terms of  $P_{\delta E_{xx}}$ . To determine the thermally-limited minimum detectable electric field gradient, we set  $P_{\delta f_c}$  (Eq. 4.12) equal to  $P_{\delta f_c}^{\text{therm}}$  (Eq. 4.4) and find that:

$$P_{\delta E_{xx}}^{\text{therm}} = \frac{4k_B T \Gamma}{q_c^2 x_{\text{rms}}^2} \quad (4.23)$$

where we have written the result in terms of the dissipation constant using  $\Gamma = k_c/2\pi f_c Q$ . For a commercial electric force microscope cantilever,  $\Gamma = 1.5 \times 10^{-9}$  Ns/m ( $f_c = 75$  kHz,  $k_c = 3.5$  N/m, and  $Q = 5 \times 10^3$ ). For an ultra-sensitive cantilever, the friction coefficient can be as low as  $\Gamma = 5 \times 10^{-13}$  Ns/m ( $f_c = 7.4$  kHz,  $k_c = 0.7$  mN/m, and  $Q = 3.1 \times 10^4$ ) [13]. We conclude that the ultra-sensitive cantilever can resolve a 3000-fold smaller fluctuation  $P_{\delta E_{xx}}$  than can a commercial cantilever operated in vacuum with the same tip charge and amplitude.

# CHAPTER 5

## TOWARD A LOCAL MEASUREMENT OF CARRIER MOBILITY IN ORGANIC FIELD EFFECT TRANSISTORS

### 5.1 Summary

In Chapters 3 and 4, we described a method for measuring microscopic electric field and electric field gradient fluctuations using scanned probe microscopy. We tested the technique on thin films of three common polymers – PMMA, PVAc and polystyrene. These polymers were good test candidates because they are readily available, easy to prepare and have had their properties quite thoroughly characterized.

We now turn our attention to organic semiconductors, an interesting class of molecules with properties that are considerably less well understood. Organic semiconductors have attracted a great deal of attention in recent years because they are more mechanically flexible, easier to process and cheaper to synthesize than their inorganic counterparts. However, it is unlikely that they will become viable candidates for semiconductor technology in the absence of a more thorough understanding of their electronic properties. Charge transport in amorphous films of small  $\pi$ -conjugated molecules at high temperature[89, 90, 91] is believed to be mediated by transitions between localized electronic states (“hopping transport”). However, in single crystals of  $\pi$ -conjugated molecules at low temperature, there is general agreement that band transport is probably the dominant mechanism of charge transport. In polycrystalline and polymeric materials, where both ordered and disordered regions of molecules are present, models have been developed although to our knowledge these models have not

been tested microscopically [92].

The most well established methods for characterizing the temperature- and electric-field dependence of mobility in amorphous films and molecularly doped polymers are time-of-flight current-transient measurements [93, 89] and analysis of current-voltage characteristics. Time-of-flight measurements are well suited for the slow (relative to silicon) transport times of organic semiconductors, but require films with thicknesses on the order of  $\sim 10 \mu\text{m}$  - about two orders of magnitude thicker than optimal for most organic semiconductors. However, the main difficulty with both time-of-flight and current-voltage experiments is that these techniques cannot readily be used to distinguish between bulk and local effects. These local effects can include contributions from polymer chain packing, dipoles at the organic/dielectric interface, charge density, trapped charge and injection barriers.

It is possible to obtain independent estimates of contact and bulk resistance by studying many transistors with different channel lengths, but the interpretation of this data can be problematic on account of factors like short channel effects, space charge effects and contact effects. In other words, the mode of charge conduction may change with the geometry of the device. Scanned probe microscopy is a technique well suited to address this challenge because it is sensitive to local effects.

In Chapter 4, we showed that thermally induced dielectric fluctuations in polymers are detectable as frequency jitter or non-contact friction. The mobile charges in organic semiconductors are also expected to give rise to fluctuating electric fields, which in principle should be detectable as non-contact friction or jitter. In this chapter, we propose a method for measuring the local carrier

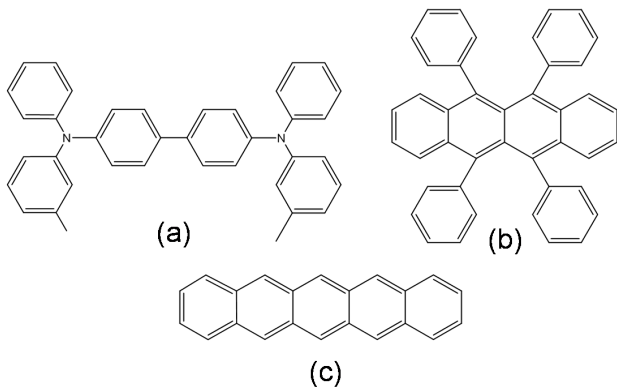


Figure 5.1: Small molecule organic semiconductors. (a) N,N'-diphenyl-N,N'-bis-(3-methylphenyl)-1,1'-biphenyl-4,4'-diamine (TPD). (b) rubrene. (c) pentacene.

mobility in an organic field effect transistor and present our preliminary efforts toward realizing this goal.

## 5.2 Why organic semiconductors?

Organic semiconductors, unlike their inorganic counterparts, transport charge by means of delocalized,  $\pi$ -conjugated linkages or by hopping between localized states instead of through a crystal lattice [94]. Most organic semiconductors are either small molecules (e.g. pentacene and rubrene) or strongly  $\pi$ -conjugated polymers such as poly(3-hexylthiophene) and poly(p-phenylene vinylene). Figures 5.1 and 5.2 depict some of the most commonly studied systems. Semiconduction in an organic species was first reported in 1963 by Weiss *et al.*, who reported high conductivity in iodine-doped oxidized polypyrrole [95]. In 1979, Shirakawa *et al.* [96] reported high conductivity in oxidized and iodine-doped polyacetylene and in 2000, Shirakawa, Heeger and MacDiarmid shared the Nobel Prize for Chemistry.

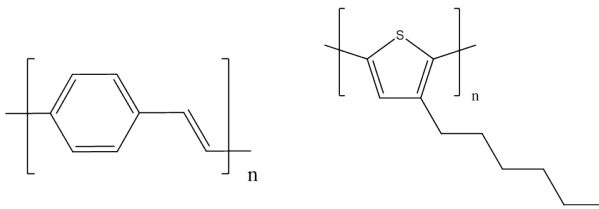


Figure 5.2: Semiconductive organic polymers. Left: poly(p-phenyl vinylene). Right: poly(3-hexyl thiophene)

In recent years, with the successful commercialization of organic light-emitting diodes, there has been a flurry of interest in organic semiconductors in both academic and industrial circles. In large part, this is because organic semiconductors are cheaper and easier to process than traditional silicon-based semiconductors [97]. Most conjugated organic polymers are solution-processable and can readily be spin-coated or inkjet printed onto a substrate, thus avoiding the expense and trouble of vacuum sublimation. Small organic molecules tend to be superior semiconductors, but generally must be deposited via vacuum sublimation. Organic semiconductors are not expected to compete with high-end silicon technology; however, they are promising candidates for lower-resolution, mechanically flexible or large area items such as identification tags, smart cards and displays [98]. In May 2007, Sony Corporation reported the first full-color, flexible, all organic display, in which both the thin film field-effect transistors and the light emitting pixels were made of organic materials. In terms of energy efficiency, these displays were a significant improvement over their liquid crystal display or plasma-based predecessors.

Silicon can form a nearly perfect crystal lattice, and for this reason the physics of inorganic semiconductors is quite well understood. Charge transport in silicon occurs via band transport, where charge is delocalized over extended

states [99]. Describing the path of charge through an amorphous, massive polymer or through a collection of loosely associated small molecules is less straightforward. However, Dunlap and Novikov [90, 91] have developed a predictive theory describing charge transport in amorphous films of small molecules. Charge transport in disordered polymers is regarded as a hopping process between localized sites, which are thought to consist of conjugated polymer chain segments [100]. The remainder of this thesis describes our experimental efforts to characterize charge transport in an organic semiconductor via scanned probe microscopy.

### 5.3 Introduction to field effect transistors

The field-effect transistor (FET), first developed by Shockley in 1952, is essentially a voltage-controlled resistor [99] and is an integral component of most digital integrated circuits. A FET is a three-terminal device constructed from the following basic components: electrodes (for the source, drain and gate), a dielectric layer (frequently  $\text{SiO}_2$ ) and a semiconducting layer. The current flow between the drain and source electrodes  $I_{\text{ds}}$  is modulated by an applied gate voltage  $V_g$ . When a voltage is applied between the source and the gate, charges are induced in the semiconductor at its interface with dielectric layer [98]. A generic FET is depicted in Figure 5.3. One of the key indicators of a FET's performance is its field-effect mobility, a term which is sometimes confused with carrier mobility in the literature. Carrier mobility is the proportionality constant between carrier drift velocity and the applied electric field across a material [99]:

$$E = \frac{v_{\text{avg}}}{\mu}, \quad (5.1)$$

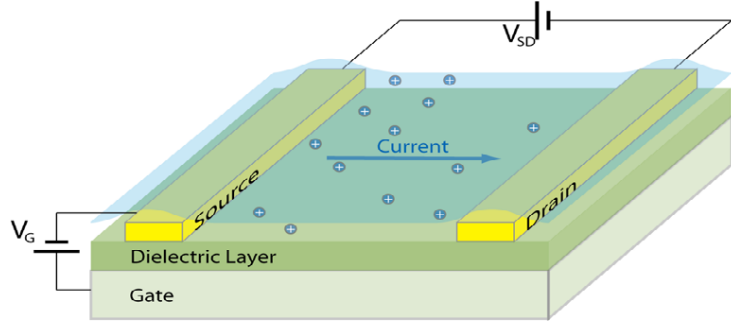


Figure 5.3: Generic field-effect transistor. Charge is induced into the interface between the dielectric layer and the semiconductor layer via application of voltage between the gate and the source. Current flows from the source to the drain. The device can be conceptualized as a voltage-controlled resistor

where  $E$  is the electric field and  $v$  is the drift velocity, or the terminal velocity that a particle such as an electron attains due to an electric field. A schematic of the motion of charge carriers through a field-effect transistor is shown in Figure 5.4. The current-voltage characteristics of a field-effect transistor prepared from N,N'-diphenyl-N,N'-bis-(3-methylphenyl)-1,1'-biphenyl-4,4'-diamine (TPD) are shown in 5.5.

The simplest and most common way to determine field-effect mobility is to extract it from the current-voltage (I-V) characteristics. The relationship between current and voltage in the saturation region is governed by the following equation, which is derived in full in Ref. [101]:

$$I_{ds} = \frac{WC_i}{2L}\mu(V_g - V_t)^2, \quad (5.2)$$

where  $I_{ds}$  is the current in the saturation region of the curve,  $V_g$  is the applied gate voltage,  $V_t$  is the threshold voltage,  $\mu$  is the field-effect mobility,  $W$  is the channel width,  $L$  is the channel length and  $C_i$  is the capacitance per unit area

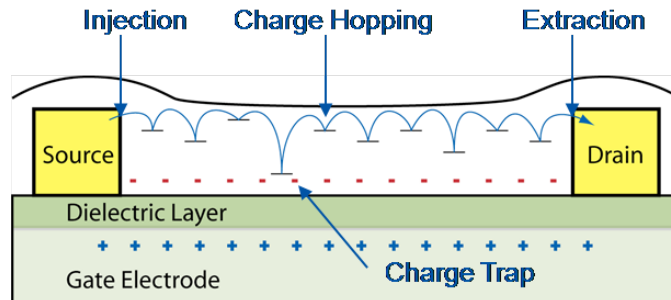


Figure 5.4: Schematic of charge motion through an organic semiconductor. Charges are induced into the channel via application of a gate voltage. Injection occurs at the source and can be a significant source of resistance. Charges “hop” between localized sites, possibly falling into low-energy “trapping” sites before eventual extraction at the drain.

of the dielectric layer. The threshold voltage is the gate voltage at which sufficient carriers accumulate in the inversion layer to enable the formation of a low resistance conducting path, or channel, between the source and the drain. At source-drain voltages significantly smaller than  $V_g$ , the device behaves like a variable resistor and the FET is said to be in “linear mode” or “ohmic mode”. In this mode, the only effect of changes to  $V_g$  is to alter the channel resistance. At source-drain voltages comparable to or larger than the gate voltage, the potential gradient across the source-drain gap increases and the shape of the channel becomes asymmetric or “pinched” at the drain. The FET is said to be in “saturation mode” and behaves as a fixed current source. The field-effect mobility  $\mu$  can be obtained by fitting I-V data to Eq. (5.2). One difficulty with field-effect mobility as an indicator of performance is that it cannot be used to discern the effects of contact resistance (i.e. the energy barrier associated with the transport of charge from a metal electrode into an organic film) from the intrinsic ability of the organic film to conduct. This may be a significant obstacle to the design of new conductive materials.

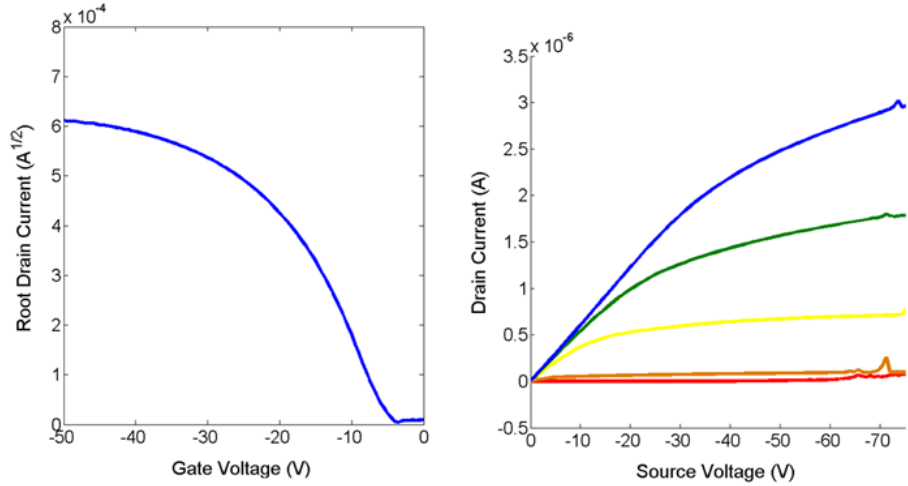


Figure 5.5: Characteristic transfer curve (left) and output curves (right) for a TPD field effect transistor. The output curves are a plot of applied source voltage versus drain current at various gate voltages: 0 V (red), -20 V (orange), -40 V (yellow), -60 V (green) and -80 V (blue). The film thickness was 80 nm and the field-effect mobility on the order of  $10^{-6} \text{ cm}^2/\text{Vs}$ . The transfer curve is a plot of the applied gate voltage versus the drain current at a current source-drain voltage of -30 V. It is clear that current begins to flow at around  $V_{\text{gate}}=+5\text{V}$ , which corresponds to the threshold voltage of the device. Here the dielectric layer was 300 nm of thermally grown ( $n=1.46$ ) silicon oxide, the total channel length was 1.5 m and the gap size was 5  $\mu\text{m}$ .

## 5.4 Literature survey: theoretical descriptions of carrier mobility in organic semiconductors

One of the difficulties with Eq.(5.2) is that it relies on an assumption that is frequently observed for inorganic semiconductors, but not for organic semiconductors – namely that mobility is field-independent. A general feature of charge transport in organic materials is that the mobility becomes field dependent at high electric fields [101]. For amorphous films of small molecules at low charge density, this dependence is well understood and has been described by Dunlap *et al.* [90], and Novikov *et al.* [91], as described in Borsenberger and Weiss [89].

There have been several other studies suggesting that  $\mu$  is governed by a number of additional quantities, including morphology [21], the number of semiconductor monolayers [102], charge density [103, 100] and the temperature [104]. None of these additional factors are reflected in Eq. (5.2), and it remains a challenge to formulate a description of charge transport that is more appropriate to an organic system.

A number of groups have endeavored to find a more suitable theoretical model for carrier mobility in organic semiconductors. Vissenberg and Matters [105] derived an analytic expression for the field-effect mobility in a thin-film transistor of an amorphous semiconductor, using percolation theory and the idea that charges in an organic semiconductor “hop” from site to site in an exponential density of localized states of the form:

$$g(\epsilon) = \frac{N_t}{k_b T_0} \exp\left(-\frac{\epsilon}{k_B T_0}\right), \quad (5.3)$$

where  $N_t$  is the number of states per unit volume and  $T_0$  is a parameter that indicates the width of the exponential distribution. Their final expression exhibits strong dependence on both temperature and charge density.

Pasveer *et al.* [100] undertook a numerical solution of a steady state master equation representing hopping of charge carriers on a lattice of sites:

$$\sum_{j \neq i} [W_{ij} p_i (1 - p_j) - W_{ji} p_j (1 - p_i)] = 0 \quad (5.4)$$

where  $p_i$  is the probability that site  $i$  is occupied by a charge and  $W_{ij}$  is the transition rate for hopping from site  $i$  to  $j$ . The factors  $1 - p_i$  reflect the assumption that only one carrier can occupy a site. They solve Eq. (5.4) by assuming that the carriers hop between sites arranged in a cubic lattice; the site energies are drawn randomly from a Gaussian distribution of width  $\sigma$ . Their final expression, which also depends strongly on charge density and temperature, agreed

well with experimental data; they found that omitting the charge density and electric field dependences significantly worsened the agreement.

Unfortunately, most theories of carrier mobility in organic systems introduce empirical parameters that are specific to a particular material, and accordingly must be fitted to experimental data [106]. A complete theory of charge transport in organic semiconductors remains elusive.

## 5.5 Literature survey: experimental techniques for measuring mobility in organic semiconductors

Many literature values of organic semiconductor mobilities were obtained via analysis of the current-voltage characteristics of field-effect transistor devices. However, there are several other more complicated, but probably more accurate experimental methods for determining field-effect mobility in organic transistors. Most of these techniques (time of flight, time-resolved microwave conductivity and electron spin resonance) suffer from the same limitation - they are generally only valid for low charge densities. In addition, none of them provide information about the effects of the electrode/semiconductor contact.

Time of flight (TOF) spectroscopy is a technique for measuring the time it takes for a particle, object or stream to reach a detector whilst traveling over a known distance in a known applied electric field. Application of TOF measurements to organic semiconductors is described in Refs. [89] and [93]. Dodabalapur and coworkers [107] were the first to use a TOF method to measure carrier mobility in an organic field effect transistor. They studied a thin film

poly-3-hexyl thiophene transistor by turning the device on, allowing it to reach a steady state, then introducing a quick voltage pulse at the source. The effect of the pulse, which is only a fraction of the applied DC bias, is to inject a few extra carriers into the channel. These carriers traverse the channel and are collected at the drain; their transit time is collected according to traditional time-of-flight techniques.

Time-resolved microwave conductivity (TMRC), was developed by Warman and co-workers [108]. In this technique, the material's microwave conductivity is monitored after irradiation with a nanosecond pulse of 3-MeV electrons. This technique may facilitate measurement of a truly intrinsic  $\mu$  because it does not require any contact with the sample. However, because charges do not move very far in a microwave-frequency electric field before they turn around, they cannot encounter imperfections like grain boundaries, defects, or chain kinks. For this reason, TDMC measurements may be of limited utility. The other disadvantage of this technique is that it requires the assumption that only one type of carrier displays a significant intrinsic  $\mu$ .

Kuroda and co-workers [109] observed charge carrier concentration in a polythiophene-based transistor using electron spin resonance (ESR). They observed ESR signals from field-induced polarons upon application of a gate voltage to the device. The ESR signal was observed to steadily decline with increasing source-drain voltage, ultimately reaching 50% of its initial intensity at the pinch-off voltage of the device.

## 5.6 Literature survey: non-contact friction studies of semiconductor devices

There have been several scanned probe microscopy studies of conductive materials. Denk and Pohl [77] were the first to study non-contact friction over a semiconductor; they observed that friction over GaAs depended strongly on the doping. Stowe *et al.* studied the dopant density in n-type and p-type silicon samples by imaging the non-contact friction near the surface. Salmeron *et al.* [110] used atomic force microscopy to show that friction over highly doped silicon depends strongly on charge carrier concentration. They patterned alternating stripes of p- and n-doped regions into silicon via ion implantation and controlled the carrier concentration by applying a tip-sample bias. They observed a significant increase in friction when a positive voltage was applied to the AFM tip whilst it was positioned over a p-type region and attributed this to induced band bending. Because carrier density depends exponentially on the energy difference between the Fermi level and the valence band edge, the band bending gives rise to accumulation of majority carriers (holes) near the semiconducting surface. Salmeron *et al.* were thus the first to directly detect charge carrier accumulation via scanned probe microscopy. However, the fact that complementary behavior was not observed over the n-doped stripe suggests that the interpretation experiment is not completely understood.

Tal *et al.* [41] determined the density of states and the microscopic effects of doping in an amorphous organic film via Kelvin probe microscopy, to the density of states, related to the contact potential difference between the cantilever tip and the sample. They also found that the density of states broadened signif-

icantly upon addition of a dopant.

## 5.7 A new approach to measuring carrier mobility in an organic semiconductor

Most of the common methods for measuring carrier mobility exploit the relationship between carrier mobility and current. We attack the problem from another angle. Device current is related to carrier mobility via  $J = \sigma\mu E$ , where  $\sigma$  is the charge density and  $E$  is the applied electric field. However, mobility is also related to the intrinsic diffusion constant of the material's charge carriers. This relationship is encapsulated by the Einstein relation:

$$D = \mu k_B T, \quad (5.5)$$

where  $D$  is the diffusion constant and  $\mu$  is the mobility of the particles. Hirao and coworkers [111] have explored the relationship between mobility and the diffusion coefficient in molecularly doped polymers for a time-of-flight experiment. They assume that the initial carrier distribution of charges in the channel is injected via a light pulse, and then use the equation for the transient current of a thin sample to calculate the photocurrent resulting from the initial carrier distribution. They fitted this equation to measured photocurrent transients to obtain a relationship between mobility and the diffusion constant. They also derived a relationship between mobility and the diffusion coefficient from the Langevin equation for a molecularly doped polymer (e.g. TPD in polystyrene), modelling the mobile charges as randomly oriented dipoles which give rise to a random, fluctuating electric field.

Professor John Marohn has derived a relationship between cantilever frequency jitter/friction and the diffusion constant. Assuming a two-dimensional plane of charged particles in the absence of an applied electric field, the density of particles evolves according Fick's law:

$$\frac{\partial \rho}{\partial t} = D \left( \frac{\partial^2 \rho}{\partial x^2} + \frac{\partial^2 \rho}{\partial y^2} \right) \quad (5.6)$$

The number of particles remains constant:

$$N = \int_{-\infty}^{+\infty} dx dy \rho(x, y; t) \quad (5.7)$$

Using Eq. 5.6 and Eq. 5.7, it is possible to formulate an expression for the distribution of these randomly diffusing charges at time  $t$ . The results of Chapters 3 and 4 suggest that these diffusing charges will give rise to a fluctuating electric field at the cantilever that can be detected as friction or jitter. An expression for the fluctuating electric field may be derived by approximating the tip as a point charge located some distance above the plane of diffusing charges, and assuming that the interaction the tip and the plane is mediated by Coulomb's law. The final expression for friction is:

$$\Gamma_s(f_c) = \frac{c_a Q^2}{k_B T} \left( \frac{q}{4\pi\epsilon_0} \right)^2 \frac{\pi}{D} P(2\pi f_c \tau) \quad (5.8)$$

where

$$P_{\delta f_c}(\theta) = \int_0^{+\infty} \frac{\alpha^3 e^{-2\alpha}}{\theta^2 + \alpha^4} d\alpha \quad (5.9)$$

and where  $\theta = \frac{2\pi f h^2}{D}$ ,  $h$  is the distance between the tip and the sample,  $c_a$  is the charge density and  $\tau = \frac{h^2}{D}$ . The final expression for jitter is:

$$S_{\delta f}(f) = \frac{3\pi}{16} \left( \frac{c_a q^2 f_c^2}{k_c^2} \right)^2 \left( \frac{q}{4\pi\epsilon_0} \right)^2 P' \left( \frac{2\pi f h^2}{D} \right) \quad (5.10)$$

where

$$P'(\theta) = 4 \int_0^{+\infty} \frac{\alpha^5 e^{-2\alpha}}{\theta^2 + \alpha^4} d\alpha \quad (5.11)$$

Our approach to the experiment is to fabricate an organic thin-film transistor, position the cantilever over the device perpendicular to the direction of charge motion and then test the predicted dependence of jitter and friction on tip-sample height and charge density. A schematic of the experiment is depicted in Figure 5.6. Two promising candidates for this experiment are poly-3-hexylthiophene and TPD.

Regioregular poly(3-hexylthiophene) (P3HT) is one of the most promising organic semiconductors (its structure is shown in Fig.5.2). Field-effect mobilities as high as 0.1-0.3 cm<sup>2</sup>/Vs have been achieved for this species; these values rival those of amorphous silicon [21]. Thin films of P3HT adopt a microcrystalline lamellar microstructure. They are usually comprised of two-dimensional conjugated layers with strong  $\pi$ - $\pi$  interchain interactions that are separated by layers of solvating, insulating side chains. The mobility of P3HT depends very sensitively on the degree of head-to-tail regioregularity and deposition conditions [112].

TPD (see Fig.5.1 (a)) is a small molecule that has a modestly high hole drift mobility and was initially developed as a charge transport layer in xerography [89, 112]. TPD-doped polystyrene is a very low-mobility material and thus is not considered a promising candidate for commercial electronic devices. Indeed, Furukawa *et al.*'s 2003 report on the infrared structure of thermally evaporated TPD is one of the few published instance of a TPD-based transistor [113]. However, in principle, TPD is an excellent test system for the theory described in Section 5.7, which assumes that electric field fluctuations arise only from the motion of randomly diffusing mobile charges. TPD is believed to conduct exclusively by "hopping". On the other hand, thin films of P3HT are known to

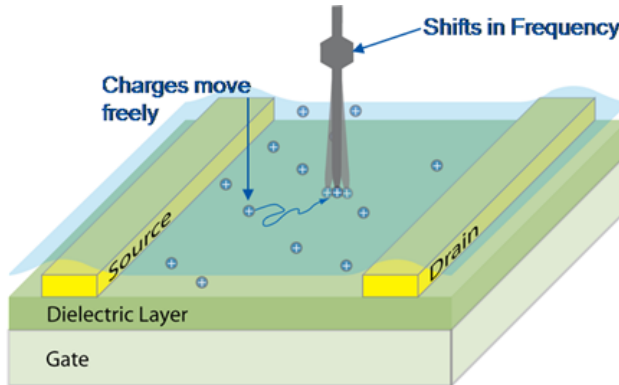


Figure 5.6: Schematic of the experiment. We prepare a field-effect transistor and deposit a thin organic film between the source and the drain via spin-casting. We position the cantilever between the source and drain electrodes and induce charges into the channel by applying a gate voltage. Because the source-drain potential is zero, we expect the motion of the charges to be governed by thermal diffusion. We then extract the diffusion constant from a relationship between friction/jitter and the gate voltage that was derived in 5.7.

contain both amorphous (low  $\mu$ ) and microcrystalline regions (high  $\mu$ ). The presence of these microcrystalline regions, which may conduct via some form of band transport [92], makes P3HT a difficult system to characterize.

The additional advantage of TPD is that it can be deposited in extremely smooth, flat films. In our laboratory, we have obtained surface roughnesses on the order of  $\pm 4$  nm. This is an attractive characteristic because the cantilever frequency shift is governed by capacitance as well as by the surface potential, and the interpretation of EFM measurements can be complicated by rough film surfaces.

## 5.8 Experiment: substrate fabrication

We fabricated two types of bottom-contact field-effect transistors from heavily doped n-type silicon (Wafer Works), both of which are depicted in Figure 5.7. Appendix C contains details of the fabrication process. In both geometries, a 300 nm layer of thermal oxide was grown onto the silicon to form a robust dielectric layer. However, the electrode patterning on the two devices was very different.

The interdigitated device in Figure 5.7 (a) was designed for a microscope with full lateral scanning capabilities. Each device contained a total of 50 source-drain gaps, so the cantilever may be positioned anywhere over a  $0.75 \text{ cm}^2$  area. The devices had a total channel length of 1.5 m and a gap size of 5  $\mu\text{m}$ . The device dielectric consisted of 300 nm of thermally grown  $\text{SiO}_2$  with an estimated gate dielectric capacitance per unit area on the order of  $1 \mu\text{F}/\text{cm}^2$ .

The right device in Figure 5.7 (b) was designed for a microscope with limited scanning capabilities. The device architecture makes it possible to align the tip squarely in the center of the device between the two electrodes by eye. The drawback of the design is that it was suitable only for variable gate voltage measurements. These devices consisted of two “C”-shaped gold electrodes 0.5 cm in width separated by a  $5\mu\text{m}$  gap.

## 5.9 Experiment: preparation of thin organic films

It is imperative that all devices are scrupulously clean prior to deposition of the organic film. Before depositing a semiconducting layer, the devices were

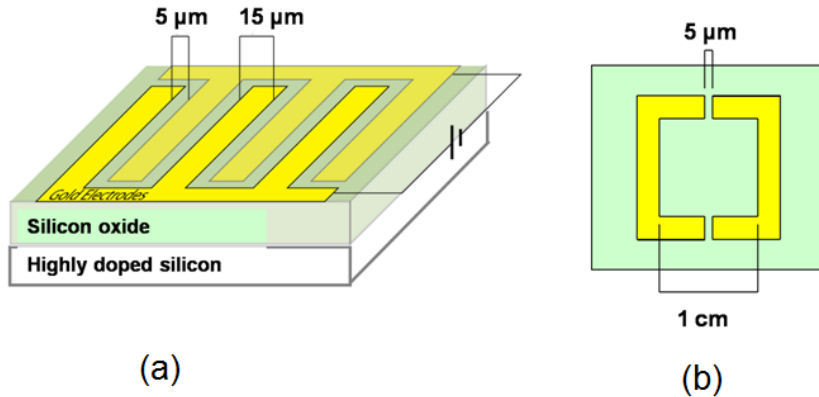


Figure 5.7: Two different device architectures. (a) interdigitated device, suitable for a microscope with scanning capabilities. (b) large-gap device, suitable for a microscope with limited scan capabilities. The silicon and dielectric layers were identical in both cases.

sonicated for 10 minutes each in acetone and isopropanol to remove photoresist or other impurities. Residual organic matter was removed via a 10 minute treatment in a UV/ozone machine (UVO-Cleaner, Model No.42, Jelight Company). We deposited the organic semiconductor by spin-coating to achieve film thicknesses on the order of 100 nm. Film thicknesses were measured via profileometry. For P3HT, we used concentrations of about 1 mg/mL and spin-cast from chloroform at 2500 rpm. P3HT was obtained from Sigma-Aldrich, Inc. (part no. 445703) and had a molecular weight of 64 kDa. We spin-cast TPD from tetrahydrofuran (purchased from Mallinckrodt Baker, part no. 8498, water content less than 0.05%) using concentrations of 15 mg/mL in 15 mg/mL of polystyrene. No additional precautions were taken to ensure that the solution was anhydrous; for a high-integrity devices it may be pertinent to do so. Polystyrene was obtained from Scientific Polymer Products and had a molecular weight of 151 kDa and a polydispersity of 1.09.

We found that device performance can be enhanced by exposing the substrate to hexamethyldisilazane (HMDS). HMDS forms a hydrophilic monolayer

on the hydrophobic SiO<sub>2</sub> surface that promotes adhesion of the organic semiconductor to the silicon oxide layer. The most assiduous technique for depositing these monolayers is vapor priming. Vapor priming is achieved by dehydrating the sample surface, then immersing it in pure HMDS vapor. Yield Engineering Systems manufactures a specialized oven for the purpose. We did not utilize this method, but rather employed a “poor man’s vapor prime”, which can be achieved by taping the substrate to the bottom of a beaker, then placing the up-turned beaker on a hot plate over a solution of HMDS. We have also found that even soaking the substrate in HMDS for 15 minutes can improve output current by an order of magnitude. HMDS was purchased from Sigma-Aldrich Inc. (part no. 379212).

Current-voltage curves for a P3HT field-effect transistor are shown in Figure 5.8; curves for a TPD FET are shown in Figure 5.5. The quality of P3HT devices can be highly variable because even small changes in the preparation process can change the morphology of P3HT thin films from amorphous to crystalline. X-ray diffraction studies have revealed that regular  $\pi$  stacking with the stacking direction in the plane of the film is important for obtaining efficient charge transport. Surin *et al.* [21] found that both the choice of solvent and the manner of deposition can have strong effects on the device performance. They also found that optimal performance is obtained when the polythiophene orders into fibrillar crystalline structures, suggesting that the fibrils act as efficient “conduits” for charge carrier transport.

We spin-cast P3HT from chloroform, but it is also soluble in 2,5-dimethyltetrahydrofuran, p-xylene and 1,2,4-trichlorobenzene. It is frequently necessary to run the solution through filter paper before spin-casting, and it is

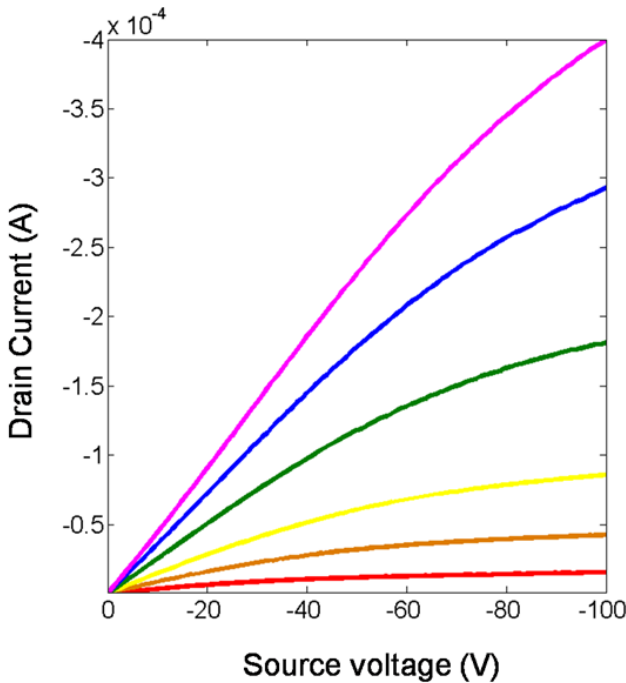


Figure 5.8: Output curves for a field-effect transistor with an active layer of 80 nm of poly-3-hexylthiophene. Here the dielectric layer was 300 nm of thermally grown silicon oxide ( $n=1.46$ ), the total channel length was 1.5 m and the gap size was 5  $\mu\text{m}$ .

critical to ensure that the glassware and all substrates are scrupulously clean, or poor device performance will be nearly a certainty. Solutions which are translucent and bright orange in color tend to yield high quality films.

We dispersed TPD in polystyrene before spin-casting it from THF. The TPD/polystyrene system is called a “molecularly doped polymer” and forms an extremely uniform amorphous film with a surface roughness of 5 nm or less.

## 5.10 Non-contact friction over a thin polythiophene film

The experiments presented in this section were conducted using the scanned probe microscope described in Chapter 2. The sample was an 80 nm film of

P3HT spin cast onto a device with the configuration depicted in Figure 5.7 (b). We grounded the source and drain electrodes, adjusted the tip-sample separation to 50 nm and varied the applied gate voltage (thus varying the charge density within the channel) from -30 V to +5 V. At each gate voltage, we measured the dependence of non-contact friction on tip voltage. One may recall from Section 4.14 that this dependence is expected to be parabolic, with the curvature of the parabola proportional to the spectral density of electric field fluctuations at the cantilever frequency. The parabola should be centered at  $\Delta\phi$ , the difference between the local electrostatic potential and the the tip's chemical potential (see Eq. 1.3).

According to the central hypothesis of this thesis, larger electric field fluctuations should give rise to a larger measured non-contact friction. We predicted that the application of a large negative voltage to the gate would induce randomly diffusing charges into the channel, generating electric field fluctuations detectable as non-contact friction. We also anticipated that the application of a positive voltage to the channel would have little or no impact on the observable non-contact friction. In fact, Figure 5.10 (b) shows that we observed precisely the opposite. We found that varying the gate voltage from 0 V to -30 V had virtually no effect on non-contact friction. On the other hand, when the applied gate voltage was positive, non-contact friction immediately evinced a dramatic increase.

On the other hand, the contact potential behaved almost precisely as predicted. Because the channel was conductive and the source and drain were grounded, we expected that the application of a negative gate voltage would induce a sheet of positive charge into the channel that would “shield” the tip

from the large negative bias, resulting in  $\Delta\phi \approx 0$  [37]. We also predicted that at positive gate voltages, the sheet of negative charges in the channel would vanish, resulting in a contact potential of  $\Delta\phi \approx V_g$ . Figure 5.10 (a) shows that this is indeed the case - the contact potential faithfully tracks positive applied gate voltages, but remains close to zero for negative gate voltages, as expected [37].

These results are puzzling. Figure 5.10 (a) appears to confirm our assumption that the application of a negative gate voltage induces hole carriers into the channel, but 5.10 (b) seems to suggest that hole carriers, if present in the channel, are either absent, immobile, or are otherwise not contributing significantly to friction. These data are simultaneously acquired, thus eliminating the possibility of trapping effects. Further experiments are necessary to fully understand this phenomenon.

## 5.11 Summary and future directions

In summary, we have fabricated, *de novo*, field-effect transistors and employed two different organic semiconductors as an active layer. We have found that non-contact friction is highly sensitive to the presence or absence of charge carriers in the transistor channel. We have also shown that  $\Delta\phi$  can be inferred by measuring  $\Gamma$  (rather than the usual observable, frequency shift) as a function of tip voltage. It may be helpful to test an organic semiconductor that conducts electrons rather than holes to see if similar results are observed.

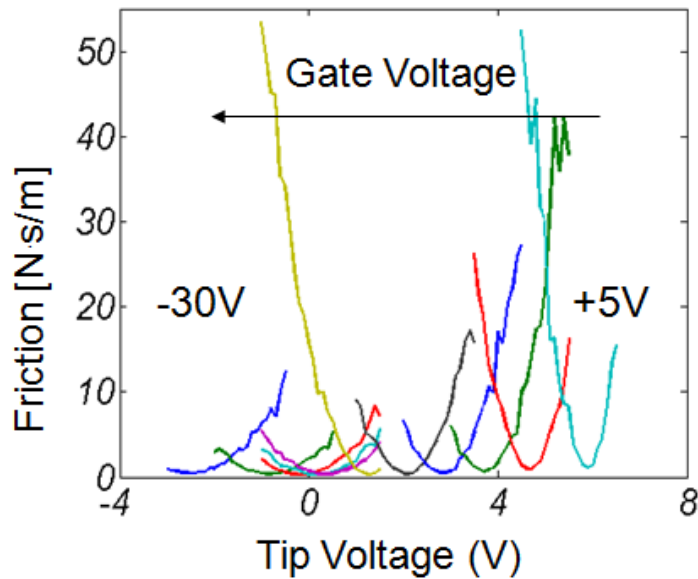


Figure 5.9: Output curves a field-effect transistor with an 80 nm thin film of poly-3-hexylthiophene. The tip-sample height was 50 nm. We grounded the source-drain potential, then applied 12 different gate voltages over the range between +5 V and -30 V. We observed that for negative voltages, where charge is expected to accumulate in the channel, the contact potential is very small. For positive gate voltages, the contact potential tracks the gate voltage.

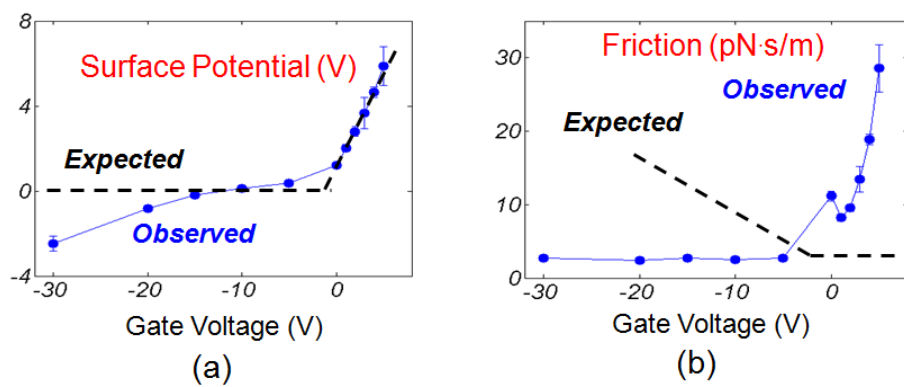


Figure 5.10: Friction over a polythiophene field-effect transistor. Theory predicts that charge accumulated in the channel should give rise to electric field and electric field gradient fluctuations, which in turn should manifest as friction or jitter at the cantilever tip.

**APPENDIX A**

**CAD DRAWINGS FOR RENOVATED DISSIPATION MICROSCOPE**

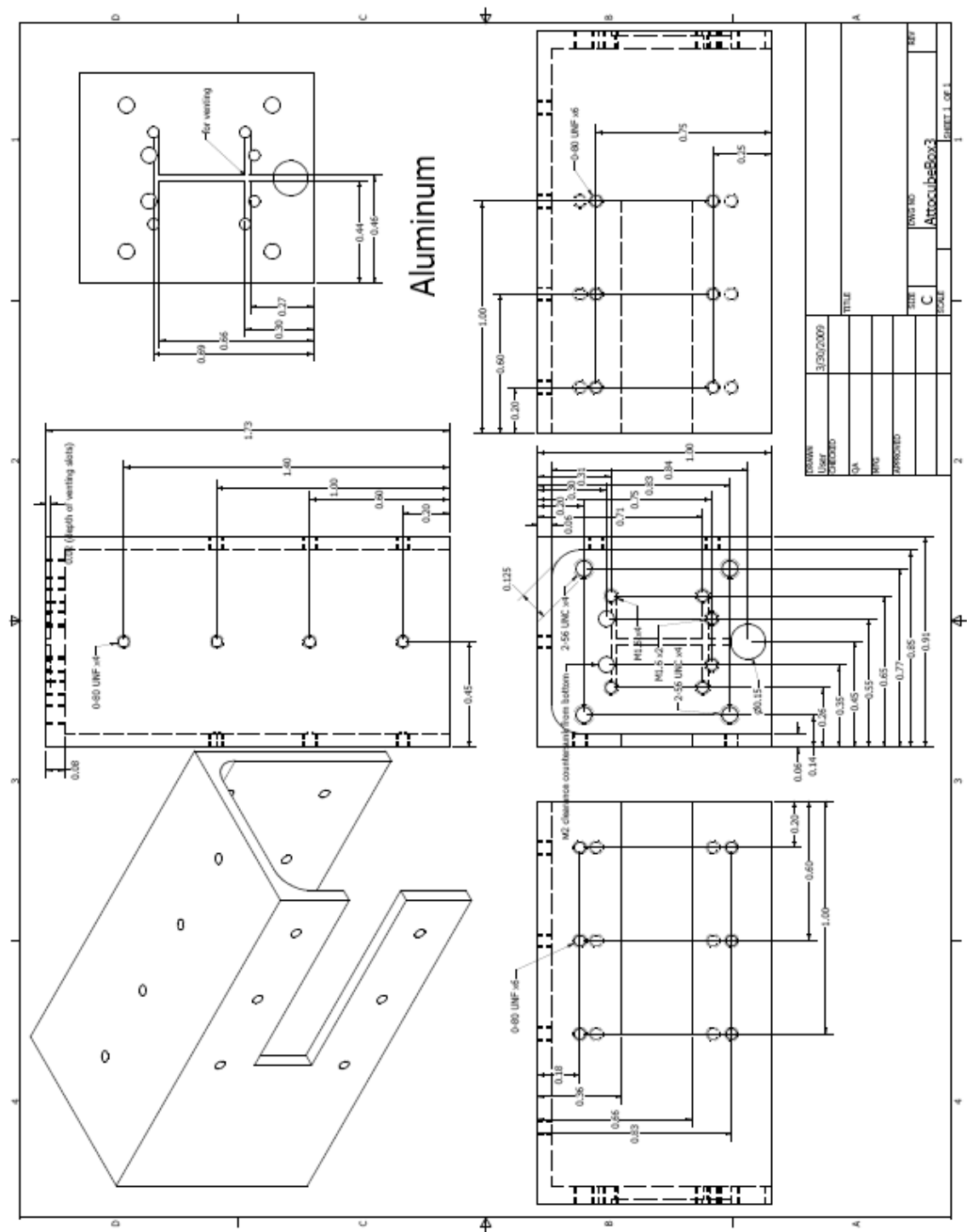


Figure A.1: The piezo stack, which consists of commercial nano-positioners purchased from Attocube AG, is exceedingly delicate. In order to protect it, we built a three-walled aluminum box to house the piezo stack. All dimensions have been carefully chosen to ensure that the stack can be mounted to the brass ring (see Figure A.2) without restricting the motion of the piezo motors.

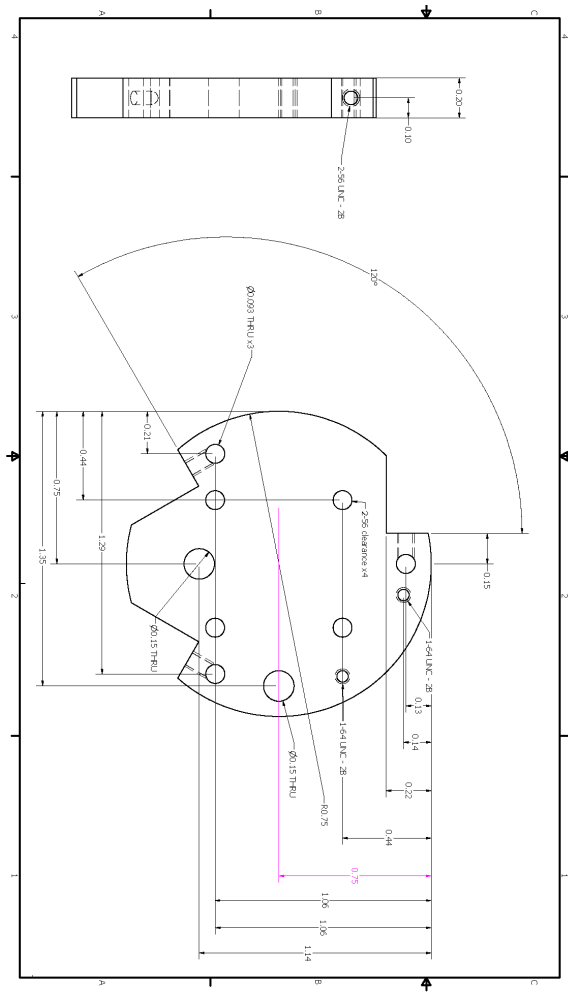


Figure A.2: The microscope's super-structure consists of three brass rings threaded onto three stainless steel rods. The upper two rings, pictured here, are identical.

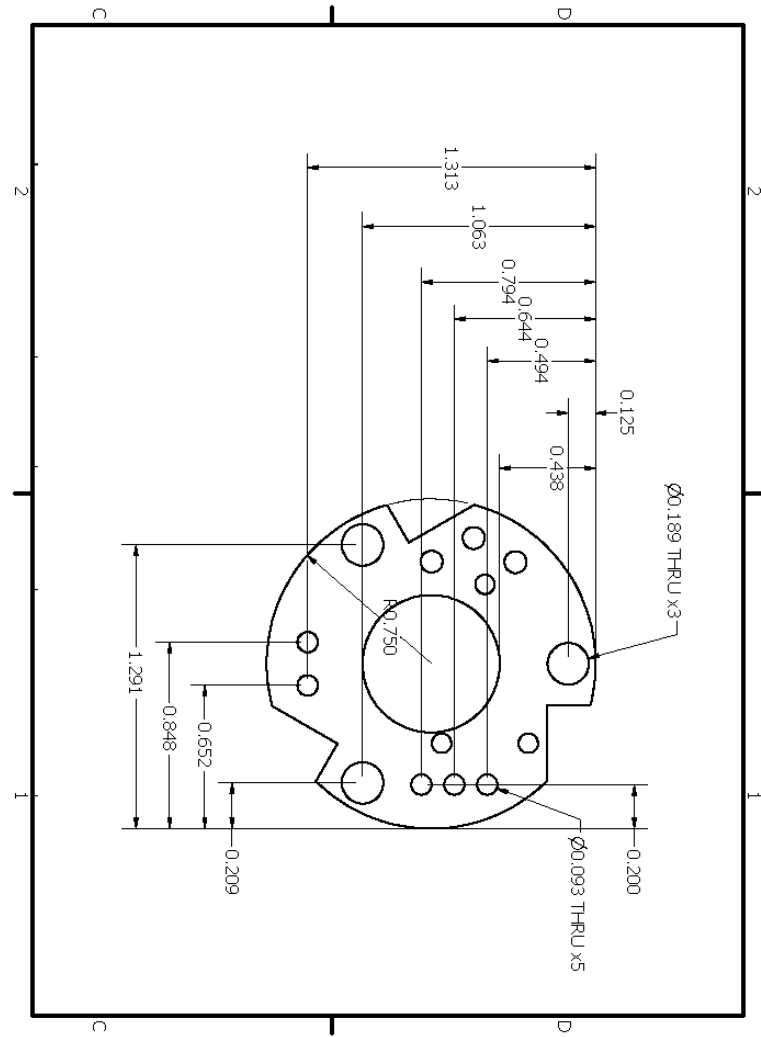


Figure A.3: The microscope's super-structure consists of three brass rings threaded onto three stainless steel rods. The stainless steel rods have a diameter of 0.125 in, except immediately below the "stops", where the diameter is 0.093 in. The lowest brass ring, pictured here, is the thickest because the piezo stack requires an inertial weight to achieve reliable coarse motion.

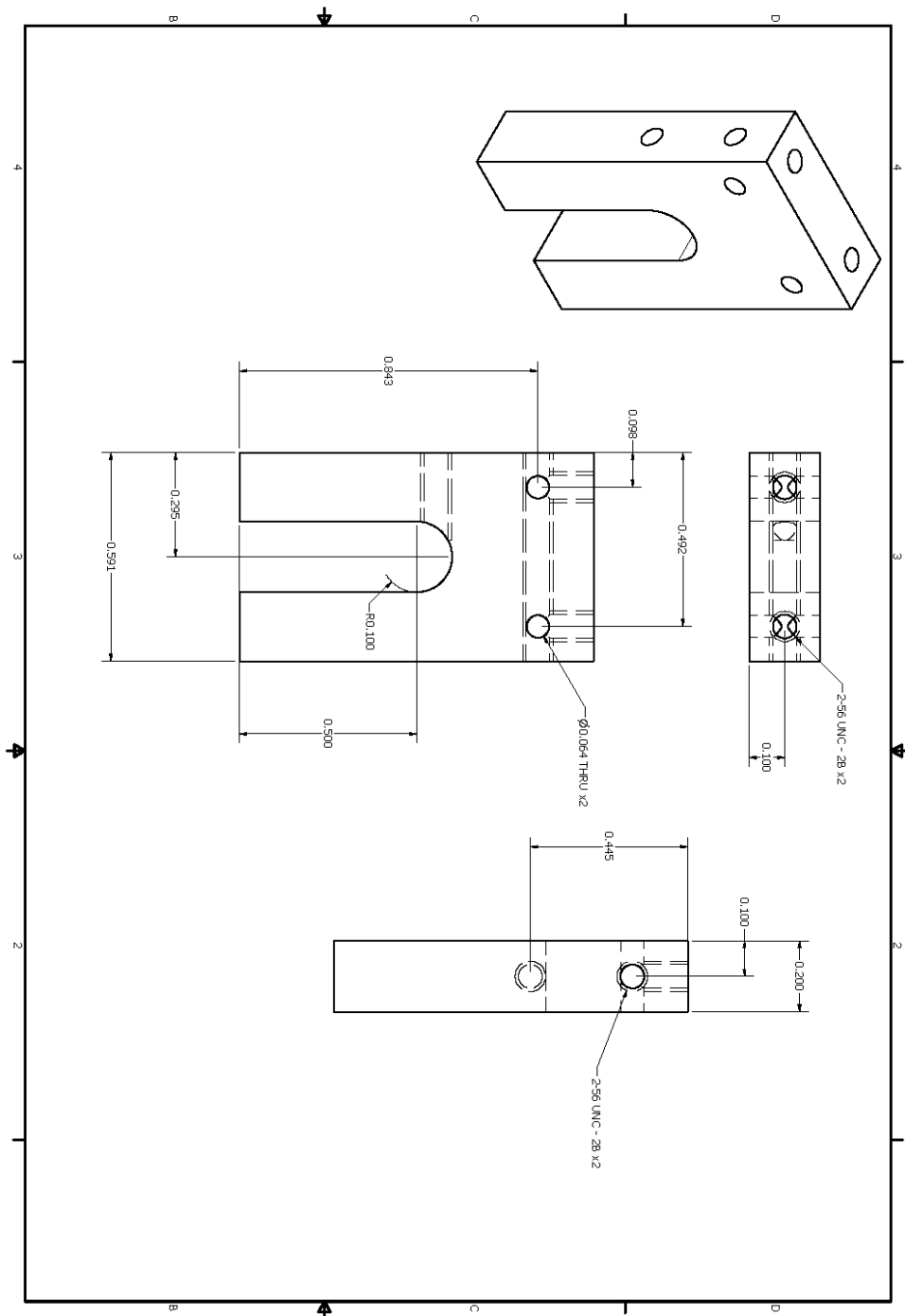


Figure A.4: In order to prevent accidental tip-sample sample, we designed the microscope such that the cantilever “slides” into place. This is the stationary element of the “slider”.

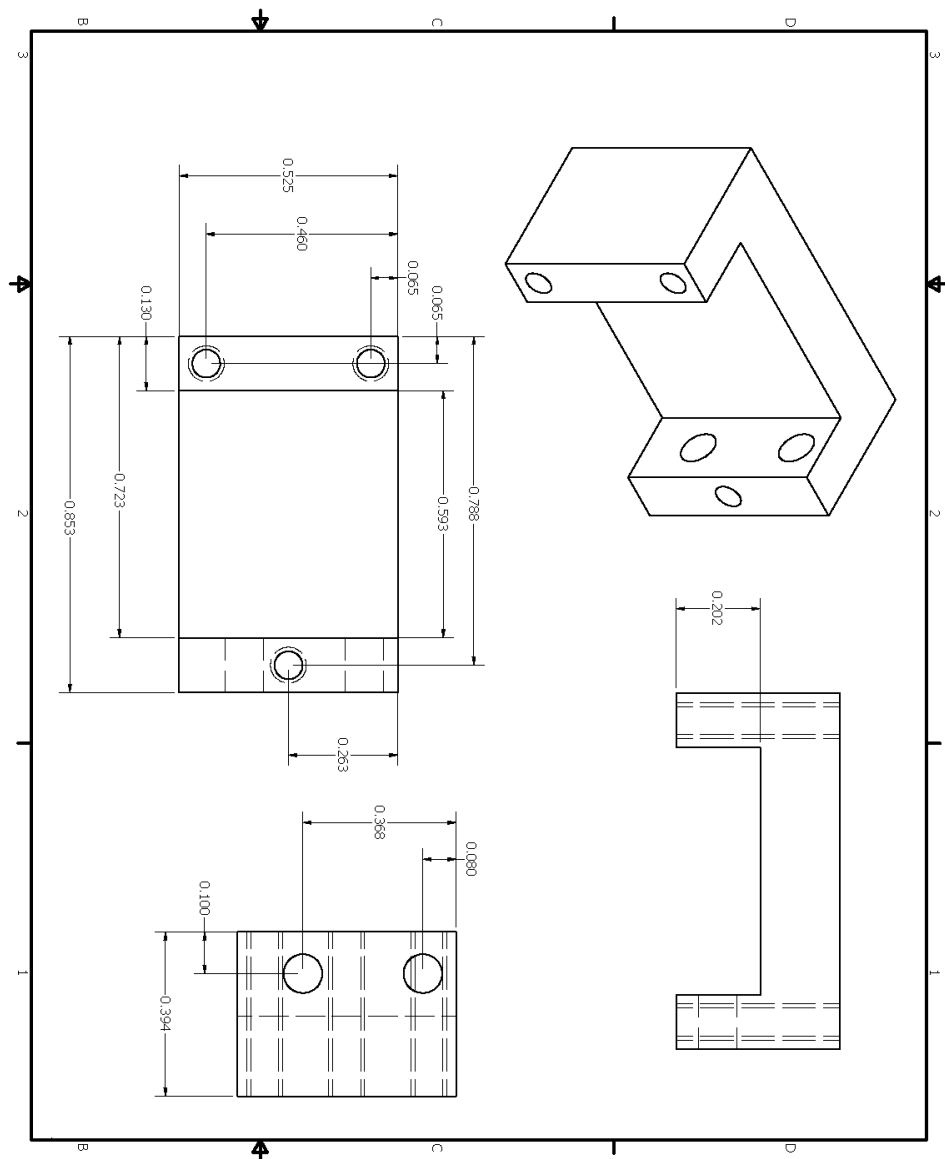


Figure A.5: In order to prevent accidental tip-sample crashes, we designed the microscope such that the cantilever “slides” into place. This is the moving element of the “slider”.

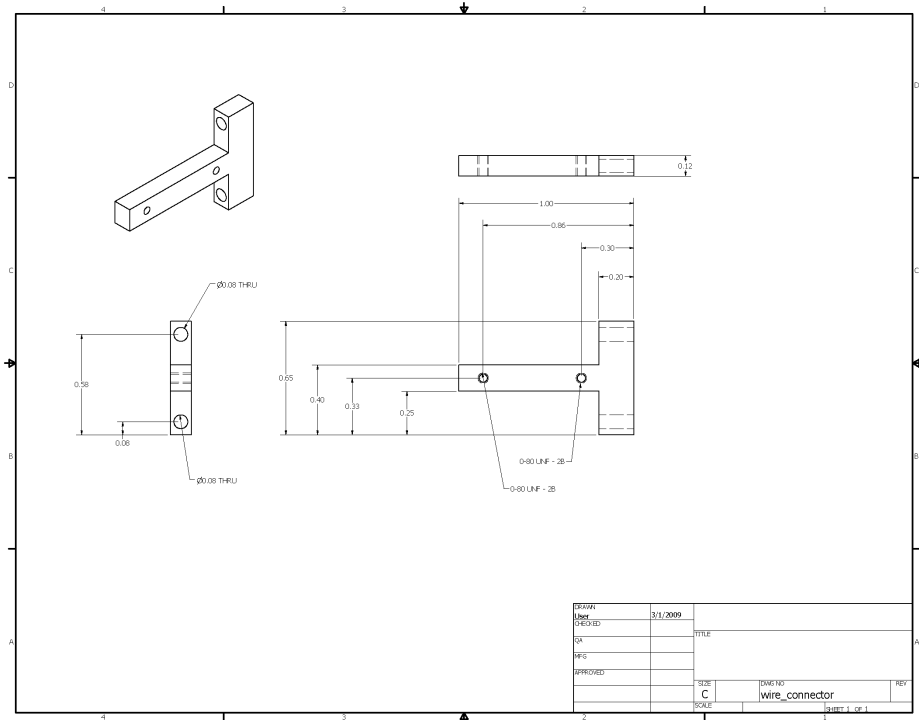


Figure A.6: Plastic (Delrin) adaptor for the 16-pin connector holding the wires to the microscope.

## APPENDIX B

### CANTILEVER FABRICATION RECIPE

This recipe was adapted from Appendix G of Ref. [47], which was itself adapted from a process pioneered by Stowe *et al.* [3] Our starting material was a silicon-on-insulator (SOI) wafer purchased from Soitech (Thick Unibond<sup>TM</sup>). The SOI wafer has three layers. The top layer consists of a 340 nm thick “device” layer of single-crystal 100 n-type silicon. The middle layer is a 400 nm layer of thermally grown SiO<sub>2</sub>, atop a 450  $\mu\text{m}$  thick base layer of silicon.

The process is comprised of three parts. First, 20  $\mu\text{m}$  by 20  $\mu\text{m}$  pits are etched into the wafer at the location of the cantilever tips. Second, the cantilevers are defined in the device layer, with the tips of the cantilevers aligned to the etched “tip thinning” pits. Finally, the 400 nm of SiO<sub>2</sub> and 450  $\mu\text{m}$  of silicon beneath the cantilevers are painstakingly removed.

#### B.1 Tip thinning pits

1. Clean the SOI wafer with acetone and isopropanol on the spinner. Use the spray bottles in the fumehood, and dispense solvent for roughly 10 seconds.
2. Deposit 1 pipette (roughly 2 mL) of MicroPrime MP-P20 (P20) onto the wafer and spin at 3000 rpm for 30 seconds. P20 is manufactured by Shin-Etsu MicroSci and consists of 20% hexamethyldisilazane (HMDS) in 80% propylene glycol methyl ether acetate (PGMEA), a solvent. HMDS, which has a molecular formula of (CH<sub>3</sub>)<sub>3</sub>Si-NH-Si(CH<sub>3</sub>)<sub>3</sub>, promotes the adhesion of photoresist to the wafer in the following manner. The surface of a silicon wafer is typically passi-

vated by a layer of adsorbed water, rendering the silicon hydrophilic. When the surface is coated with an organic photoresist, dewetting and adhesion problems can occur. “Priming” the silicon surface with HDMS displaces the adsorbed water and renders it hydrophobic, promoting adhesion of the photoresist [114].

3. Deposit 1 pipette (roughly 2 mL) of photoresist onto the wafer. We used Megaposit SPR-955-CM, a general purpose i-Line positive photoresist. Spin at 3000 rpm for 30 seconds. The resulting film should be about  $2 \mu\text{m}$  thick.
4. “Soft bake” the wafer on a hot plate at  $90^\circ\text{C}$  for 90 seconds. The purpose of the soft bake is three-fold: to drive away residual PGMEA, to improve adhesion, and to anneal away the shear stresses induced by spin coating [114].
5. Using the mask marked “Tip thinning holes”, expose the wafer for 0.3 seconds on the 5x GCA Autostep.
6. Develop in Hamatech automated wafer developer using the “300 MIF 120 seconds” recipe. MIF is manufactured by AZ Electronic Materials USA Corporation and its active ingredient is tetramethylammonium hydroxide (TMAH). TMAH is used in preference to a simple solution of NaOH to avoid contamination by metal ions.[114]
7. Etch  $220 \pm 20 \text{ nm}$  of the exposed silicon using the  $\text{SF}_6/\text{O}_2$  process in the Oxford 80 Reactive Ion Etcher. The etch is essentially isotropic. The etch rate is nominally on the order of 700 nm/minute but it can vary substantially. To establish the etch rate, either calibrate using a standard silicon wafer or etch sequentially in very small increments. We favored the latter approach because we found that the etch rates for SOI and standard silicon wafers could be inconsistent. However, it is possible that the inconsistency arose simply from the fact that our etch times were very short (less than 10 seconds) - it may take tens of seconds for the plasma to stabilize. We measured the depth of the etch pits using a P10 pro-

fileometer. Over-etching will result in narrower cantilevers.

8. Strip the resist in solvent bath 1 for 10 minutes and bath 2 for 10 minutes. The baths contain AZ 300T, a trade name for a mixture of 1,2-propanediol, 1-methyl-2-pyrrolidinone and tetramethylammonium hydroxide. Alternatively, sonicate in acetone for 15 minutes.

## B.2 Cantilever definition

1. Clean the wafer with acetone and isopropanol.
2. Deposit 1 pipette of P20 onto the wafer and spin at 3000 rpm for 30 seconds.
3. Deposit 1 pipette (roughly 2 mL) of Megaposit SPR-955-CM onto the wafer.
4. Using the mask marked “Cantilever dissipation Showey”, expose for 0.6 seconds on the 5x GCA Autostep. Set the key offset to -0.252. The units of the offset are millimeters.
5. Bake on a hot plate at 90° for 120 s.
6. Develop in Hamatech automated wafer developer using the “300 MIF 120 seconds” recipe.
7. Etch away the entire unexposed device layer using the SF<sub>6</sub>/O<sub>2</sub> process in the Oxford 80 Reactive Ion Etcher.
8. Strip the resist in solvent bath 1 for 10 minutes and bath 2 for 10 minutes.
9. Use the P10 profileometer to ensure that the entire device layer (340 nm) has been etched.
10. Repeat Steps 1-8, with the following crucial modification to Step 3: set the key offset to -0.250.
11. Inspect the wafer. At this stage, the cantilevers should be clearly and cleanly

defined. The color of the thinned tips should clearly contrast to the color of the cantilever base.

12. Soak the wafer for at least 10 hours in Microposit Remover 1165 (1165), a solvent manufactured by Shipley Company. 1165 is comprised of 1-methyl-2-pyrrolidone (molecular formula C<sub>5</sub>H<sub>9</sub>NO and a trade secret pyrrolidone compound. It is superior to acetone for resist removal, but it takes a good deal longer to achieve results. An alternative strategy is to sonicate in acetone for 15 minutes.

13. Rinse with DI H<sub>2</sub>O and blow dry with N<sub>2</sub>(g) using the chemical hood nozzles. 14. Deposit 1.5  $\mu$ m of low stress SiO<sub>2</sub> using the GSI PECVD TEOS recipe. TEOS uses tetraethylorthosilicate (C<sub>8</sub>H<sub>20</sub>O<sub>4</sub>Si) as its source material. The more standard PECVD recipes ("n 1.46", for instance) use silane or a silane derivative. "1.46" refers to the refractive index of amorphous silicon oxide. TEOS is advantageous because its silicon atoms are already fully oxidized and the process of oxide formation resembles a rearrangement rather than a reaction - a lower energy (and thus lower stress) process. During my tenure at Cornell, the TEOS processes had been disabled and we used the standard n=1.46 recipe.

### B.3 Backside processing

1. Clean the back of the SOI wafer with acetone and isopropanol on the spinner.
2. Deposit 1 pipette of P20 onto the wafer and spin at 3000 rpm for 30 seconds.
3. Steps 3-8 were devised by Steven Hickman. Deposit 2 pipettes (roughly 4 mL) of Shipley 620-7i photoresist onto the wafer in a "swirl" pattern.
4. Spin at 1800 rpm for 45 seconds. Set the spinner to accelerate at 100 rpm for 5 seconds, then 1000 rpm for 40 seconds. The period of slow acceleration

helps to evenly distribute the thick resist over the wafer. Aim for a thickness of roughly  $11\ \mu\text{m}$ .

4. Bake on a hot plate at  $90^\circ$  for 120 seconds.
5. Using the mask marked “Backside wafer Showey”, expose for 25 seconds using the EV620 contact aligner. During my tenure at Cornell, the power was  $8\text{mW/cm}^2$ . Use the “Bottom side soft contact” recipe.
6. Develop in Hamatech automated wafer developer using the “300 MIF 120 seconds” recipe.
7. If necessary, develop in Hamatech automated wafer developer using the “300 MIF 30 seconds” recipe.
8. Bake at  $90$  degrees in the convection oven for at least four hours, and preferably overnight.
9. Etch the wafer using the “1 THRU” recipe on the Unaxis ICP 770. The “1 THRU recipe” is faster than “0 TRENCH” but harsher on the wafer. After about 400 loops, remove the wafer and check the etch rate via profileometry. We found it was prudent to switch to “0 TRENCH” after the initial 400 loops. Proceed very carefully over the final 200 loops. When all of the silicon has been etched away, a thin, iridescent layer of silicon oxide will be clearly visible. Roughly 900 loops are required in total. The entire process takes 4-5 hours.
10. Remove the residual resist (if there is any; depending on the etch rate, it is possible that it will have all been etched away in Step 9) using the “Oxygen Clean” recipe in the Oxford 80 Reactive Ion Etcher. The Oxford etch rates can be quite variable, but roughly 15 minutes of etch time are required.
11. Place the wafer in teflon wafer boat custom designed by Sean Garner. The boat has a convenient teflon handle that makes transfer between solvent baths easier. Remove the silicon oxide layer by etching it in 6:1 Buffered Oxide Etch

(BOE) (manufactured by Mallinckrodt Baker). BOE is a mixture of ammonium fluoride and hydrofluoric acid (HF) and is preferable to neat HF because it enables more readily controllable etching. Residual HF is disposed of in the appropriate bottle. The HF bath itself is rinsed several times for at least two or three minutes with full-pressure streams of both DI and city water.

12. Rinse for four minutes in de-ionized H<sub>2</sub>O. Repeat three times.
13. Rinse for four minutes in isopropanol. Repeat three times.
14. Carefully transfer to the critical point dryer and run the process.
15. Inspect the finished product under the optical microscope.
16. Evaporate 15 nm of Pt onto the cantilever tips using the shadow mask technique described in Chapter 2.

## APPENDIX C

### SUBSTRATE FABRICATION RECIPE

This recipe for an interdigitated field-effect transistor was adapted from a recipe contained in Ref. [49]. The final transistors consist of a gate layer made from highly doped silicon, a 300 nm dielectric layer of  $\text{SiO}_2$  and a patterned array of metal electrodes. Wafers were purchased from Wafer Works, inc. The wafers were n-type, with phosphorus as the dopant, and had a resistivity of 0.0007-60 ( $\Omega\text{-cm}$ ).

1. Clean the wafer with acetone and isopropanol on the spinner.
2. Deposit 1 pipette (roughly 2 mL) of P20 onto the wafer and spin at 3000 rpm for 30 seconds.
3. Deposit 1 pipette (roughly 2 mL) of photoresist onto the wafer. We used Shipley 1813, a general purpose i-Line positive photoresist. Spin at 3000 rpm for 30 seconds. The resulting film should be about 2  $\mu\text{m}$  thick.
4. “Soft bake” the wafer on a hot plate at 90° for 90 seconds.
5. Using the mask marked “Gate layer”, expose the wafer for 25 seconds on the EV 620 Contact Aligner in “soft contact proximity” mode.
6. Develop in the Hamatech automated wafer developer using the “300 MIF 60 seconds” recipe.
7. “Hard bake” the wafer on a hot plate at 90° for 60 seconds.
8. Etch away the entire exposed oxide layer (300 nm) using the  $\text{CHF}_3/\text{O}_2$  process in the Oxford 80 Reactive Ion Etcher. Etch rates can vary considerably, so it is advisable to first test the apparatus on a sacrificial wafer. We used the P10 profileometer to measure all film thicknesses.
9. Etch 20-30 nm into the silicon layer using the  $\text{SiF}_6/\text{O}_2$  recipe on the Oxford 80.

10. Sonicate the wafer in acetone for 15-20 minutes to remove the resist. Rinse with dionized water and blow dry with N<sub>2</sub>.
11. Clean the wafer with acetone and isopropanol on the spinner.
12. Deposit 1 pipette (roughly 2 mL) of P20 onto the wafer and spin at 3000 rpm for 30 seconds.
13. Deposit 1 pipette (roughly 2 mL) of photoresist onto the wafer.
14. “Soft bake” the wafer on a hot plate at 90° for 90 seconds.
15. Using the mask marked “Source-Drain layer”, expose the wafer for 25 seconds on the EV 620 Contact Aligner.
16. Place the wafer into the Image Reversal oven (YES), which slowly floods the chamber with ammonia.
17. “Flood expose” using the EV 620 Contact Aligner for 25 seconds.
18. Develop in MF 321 for 60 seconds.
19. Remove residual organic material with a 2 minute “oxygen clean” in the Oxford 80 RIE etcher.
20. Using the CHA thermal evaporator, deposit 5 nm of chromium (adhesion layer) followed by 50 nm of Au. We used an evaporation rate of roughly 0.4 kÅ/s.
21. Strip resist in 1165 overnight. If lift-off has not completed, sonicate in acetone for 15-20 minutes.

## APPENDIX D

### DIELECTRIC SPECTROSCOPY

All dielectric spectroscopy measurements described below were carried out by Seppe Kuehn for the purposes of the experiments carried out in Ref. [13]. Our polymer samples were identical to those prepared by Kuehn and co-workers, so we did not find it necessary to repeat the measurements.

Dielectric spectroscopy measurements were made on 450 nm thick PMMA and PVAc films. These measurements required constructing thin-film capacitors of PMMA and PVAc of known area.

Capacitor substrates were constructed from standard quartz wafers by dicing the wafers into 1-inch squares using a commercial wafer dicing saw. The substrate squares were cleaned by repeated ultrasonication in methanol. The squares were loaded into an electron gun evaporator supplied with a custom-made evaporation jig that exposed a 1-inch by 0.5-inch area (Fig. D.1(a)). A 50 nm thick layer of aluminum was evaporated onto the quartz substrate at a rate of 0.5 nm/s to create the bottom electrode of the capacitor.

A thin film of PMMA or PVAc was spin cast onto the metalized substrate and annealed as discussed in the paper. The films were removed from the annealing oven and placed in the high vacuum chamber of the electron gun evaporator within 30 minutes to minimize contamination and water absorption. A second evaporation was then carried out to create the top electrode of the capacitor. Again the jig of Fig. D.1(a) was used, but now the substrate was rotated by 180°. To minimize substrate heating, the evaporation rate was kept below 0.1 nm/s so as not to melt the polymer thin film. During this second evaporation, the

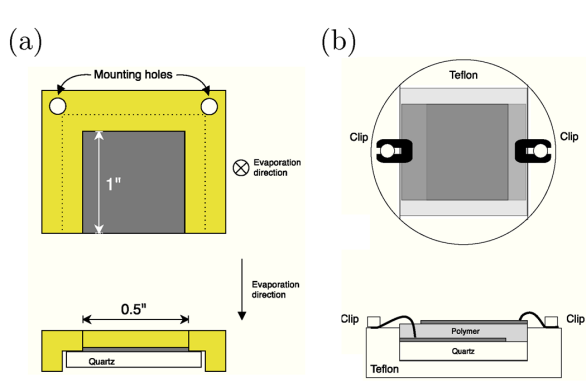


Figure D.1: Dielectric spectroscopy apparatus. (a) A custom brass evaporation jig for making capacitors from polymer thin films on quartz substrates. The actual jig evaporates four substrates simultaneously. Top down view (top): the exposed portion of the quartz substrate is evaporated with a 50 nm aluminum thin film by electron gun evaporation. The mounting holes allow mounting in the evaporator using machine screws. Profile view (bottom): the quartz substrate and the aluminum electrode. (b) Custom dielectric spectroscopy jig for capacitors constructed from thin films. Electrical contacts to electrodes are made with clips which are connected to the leads of the spectrum analyzer. For the low frequency measurements presented here coaxial cables were not necessary.

substrate thermometer did not exceed 17 °C. Slow evaporation was especially important for the low- $T_g$  PVAc samples.

The result was a capacitor where top and bottom electrodes could be independently contacted with clips, as shown in Fig. D.1(b). The capacitor had a total area of  $A = 0.5 \text{ in} \times 0.75 \text{ in} = 2.4 \times 10^{-4} \text{ m}^2$  and an electrode separation set by the thickness of the spin-cast polymer film. Several devices were sacrificed to check that evaporation of the second electrode did not alter the film thickness and to check the overall thickness of the devices by profilometry. Attempts were made to construct capacitor electrodes by sputtering gold, since sputtering gold electrodes required only a few minutes instead of the 2 hours required to sputter aluminum electrodes. Disappointingly, gold electrodes shorted with-

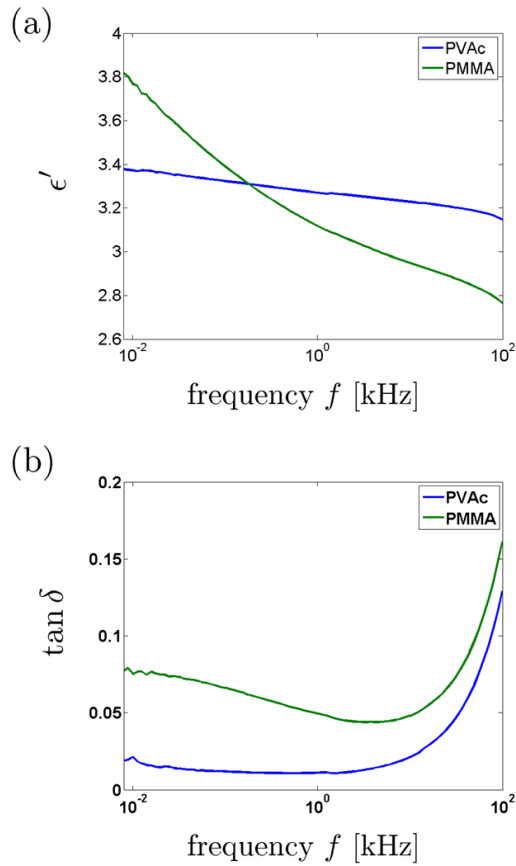


Figure D.2: Dielectric spectra of PMMA and PVAc: (a) real part of the relative dielectric constant and (b) loss tangent.

out exception. This failure was presumably the result of penetration of the gold into the polymer during evaporation or a consequence of the high mobility of gold within the polymer film at room temperature. Aluminum electrodes were unshorted 90% of the time.

A commercial impedance analyzer (Hewlett Packard; Model No. 4192 A LF) was used to measure the real portion of the capacitance and the loss tangent, defined as

$$\tan \delta = \frac{C''}{C'} = \frac{\hat{\epsilon}''}{\hat{\epsilon}'}. \quad (\text{D.1})$$

The observed (real) capacitance  $C'(f)$  was converted to (real) dielectric constant  $\epsilon'(f)$  using the parallel-plate-capacitor formula and the known area of the electrodes and the measured thickness of the polymer film. We constructed three copies of PMMA and PVAc capacitors and measured each using the impedance analyzer. There was approximately a 10% variation in the measured values across the three capacitors for both PMMA and PVAc. This variation is likely due to variation in the film thickness and possibly the metal roughness. These measurements were averaged to produce the resulting spectra shown in Fig. D.2.

We believe that the rise of  $\tan \delta$  at high frequency apparent in Fig. D.2(b) is an artifact of the lead capacitance. The lead capacitance can be compensated for [115], but this would have required measuring the lead capacitance independently, which we did not do. The error introduced by the lead-capacitance artifact in the frequency range of interest, 5 to 500 Hz, is less than 10% — smaller than the sample-to-sample variation in capacitance and therefore negligible.

Capacitors with dielectric layers of polystyrene were also constructed. The sensitivity of the Hewlett Packard 4192 A LF impedance analyzer was unfortunately not sufficient to measure the very low losses in polystyrene ( $\tan \delta \leq 0.001$ ).

Professor Ranko Richert of Arizona State University kindly provided us with the room temperature dielectric spectrum of polystyrene. The polystyrene had a weight-averaged molecular weight of  $M_w = 181,000 \text{ g/mol}$  and a polydispersity of  $M_w/M_n = 1.03$ . In the 1 to 100 Hz range, the average values for the dielectric constants are  $\epsilon' = 2.82$  and  $\epsilon'' = 5 \times 10^{-4}$ . The data was measured in the course of doing work for Ref. [116], but the spectra were not published.

APPENDIX E  
MEASUREMENT OF THE MINIMUM DETECTABLE FORCE

## E.1 Introduction to the minimum detectable force

In this section, we state the equation for the minimum force detectable by a cantilever and briefly discuss the experimental techniques involved in measuring it. In doing so, we hope to underscore the importance of the non-contact friction parameter  $\Gamma$ , which is one of the key observable quantities in the present work.

A cantilever in an atomic force microscope can be modeled quite faithfully as a harmonic oscillator that is subject to perturbation by the sample. In principle, the motion of a cantilever can be entirely described by the following equation,

$$m\ddot{x}(t) + \Gamma\dot{x}(t) + kx(t) = F(t), \quad (\text{E.1})$$

where  $x(t)$  is the direction of the cantilever's motion,  $m$  is the effective mass of cantilever,  $k$  is the cantilever's spring constant,  $\Gamma$  is the friction coefficient and  $F(t)$  is force. The resonance frequency of the cantilever  $f_c$  is related to  $m$  and  $k$  via  $f_c = \sqrt{k/4\pi^2m}$ . The frictional damping constant  $\Gamma$  is defined as  $\Gamma = k/2\pi f_c Q$ , where  $Q$  is the mechanical quality factor of the oscillator. The minimum detectable force for a cantilever is [53],

$$F_{\min} = \sqrt{\frac{2kk_B Tb}{\pi Q f_c}} \quad (\text{E.2})$$

where  $b$  is the bandwidth of the measurement. We will now discuss the experimental methods used to determine  $k$ ,  $f_c$ , and  $Q$  from an analysis of the cantilever fluctuations.

In EFM experiments,  $F(t)$  is a coherent AC force applied at the cantilever's resonance frequency. However, the cantilever is always in motion, even in the absence of an applied driving force. This is because an oscillator is subject to random forces arising from its interactions with the bath in which it resides. The source of these forces is thermal energy, and the resulting motion is known as Brownian motion. For the cantilevers used in our experiments, the Brownian motion is on the order of 10 nm at room temperature. The smallest force that can be measured *in a given bandwidth* is determined by  $\Gamma$  and temperature  $T$ . The smallest force detectable by a harmonic oscillator is thus determined by the magnitude of the time-random thermal forces ( $F(t)$ ) to which the oscillator is subject and by the intrinsic ability of the cantilever to respond to these forces ( $k_c$ ,  $f_c$  and  $Q$ ). The factors that influence  $\Gamma$  include the geometry of the cantilever and the integrity of the silicon crystal used to make the cantilever; the study of the factors affecting  $Q$  is itself an entire field of study (see, for instance, Ref. [117]).

The root-mean-square variation in cantilever displacement at a given temperature can be determined from classical and statistical mechanics. For any system where the energy is a quadratic function of a generalized coordinate and the sum over states in the partition function may be approximated as an integral [47], the equipartition theorem states,

$$\frac{1}{2}k\langle x^2 \rangle = \frac{1}{2}k_B T \quad (\text{E.3})$$

The rms thermal position fluctuations experienced by a cantilever at equilibrium in a bath,  $\langle x^2 \rangle$ , is thus set by the cantilever's spring constant and by the temperature. The spring constant  $k$  may be determined by means of the following simple experiment. If one changes the frequency of AC driving force to a cantilever, it is a property of a harmonic oscillator that  $P_{\delta x}(f)$ , the power spectrum of the cantilever's position fluctuations, will assume a roughly Lorentzian

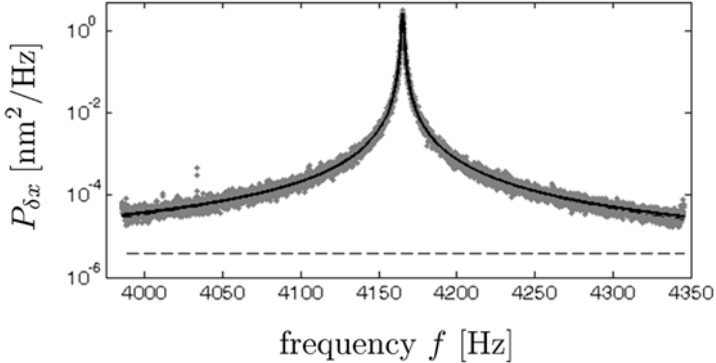


Figure E.1: Power spectrum of cantilever position fluctuations at room temperature. We slowly varied the frequency of an applied AC driving force to the cantilever, and found that the spectral density of the resulting fluctuations in the cantilever's position follow a Lorentzian distribution. For this cantilever,  $k = 0.87 \text{ mN/m}$  and  $Q = 3500$ .

lineshape centered at  $f_c$ , the cantilever's resonance frequency.  $P_{\delta x}(f)$  was discussed in Chapters 3 and 4; here it is sufficient to state that  $P_{\delta x}(f)$  is the power spectrum of the cantilever's time-dependent displacement  $x(t)$ . The results of such an experiment are shown in Figure E.1.

It is now useful to invoke Parseval's theorem. Loosely stated, Parseval's theorem states that the integral of the square of a function (in this instance,  $x(t)$ ) is equivalent to the integral of the square of its Fourier transform (in this instance,  $P_{\delta x}(f)$ ),

$$\langle x^2 \rangle = \int_0^\infty P_{\delta x} df \quad (\text{E.4})$$

Combining Eq.(E.4) and Eq.(E.3) yields the following expression:

$$\int_0^\infty P_{\delta x} df = \frac{k_B T}{k} \quad (\text{E.5})$$

In short, the integral under a power spectrum such as the one shown in E.1 is proportional to the spring constant  $k$ , which is itself proportional to  $\langle x^2 \rangle$ . This is a very useful finding because it provides direct access to the spring constant

$k$ . To determine  $Q$  we turn again to classical mechanics, which also predicts the functional form of  $P_{\delta x}(f)$ :

$$P_{\delta x}(f) = \frac{P_x(0)f_c^4}{(f^2 - f_c^2)^2 - f^2 f_c^2/Q^2} + S_x \quad (\text{E.6})$$

Here  $S_x$  is the detector noise floor and  $P_x(0)$  is the apparent position fluctuation at zero frequency, defined as follows:

$$P_x(0) = \frac{P_F(0)}{k^2} \quad (\text{E.7})$$

where  $P_F(0)$  is the power spectrum of frequency fluctuations at zero frequency. It is convenient to assume that the random force fluctuations driving the oscillator are “white” - i.e. that the power spectrum  $P_F(f)$  is flat. Fitting the data of E.1 to the equation returns least-squares estimates for  $f_c$ ,  $k$ , and  $P_x(0)$ . Combining Eqs. (E.5) and (E.6) yields the following expression for  $k$ :

$$k = \frac{2k_B T}{\pi P_x(0) Q f_c} \quad (\text{E.8})$$

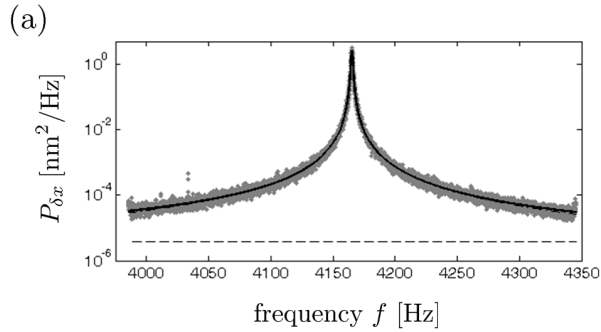
Let us revisit Eq.(E.2). Given that  $\Gamma$  is defined as  $\Gamma = k/2\pi f_c Q$ , Eq.(E.2) can thus be re-written as,

$$F_{\min} = \sqrt{4\Gamma b k_B T} \quad (\text{E.9})$$

Here  $b$  is the bandwidth of the measurement. Stated in this way, the minimum detectable force is set only by  $\Gamma$  and by the temperature.

## E.2 Details of the measurement of $k$

The spring constant  $k$  of each cantilever was measured by analyzing thermomechanical position fluctuations using the equipartition theorem, according to the approach of Hutter and Beckhoefer [82], as follows.



(b)

The position-fluctuation power spectrum was fit to the equation  
 $P_x(f) = P_x(0) f_0^4 / ((f^2 - f_0^2)^2 - f^2 * f_0^2 / Q^2) + S_x$

From curve fitting the position-fluctuation power spectrum:

avgs = 25  
 $P_x(0) = 2.053e-007 \pm 2.2445e-009 \text{ nm}^2/\text{Hz}$   
 $f_0 = 4165.2132 \pm 0.041919 \text{ Hz}$   
 $Q = 3533.7018 \pm 250.7428 \text{ unitless}$   
 $S_x = 3.8776e-006 \pm 6.9954e-007 \text{ nm}^2/\text{Hz}$   
noise floor =  $0.0019692 \pm 0.00035526 \text{ nm}/\sqrt{\text{Hz}}$

From analysis of the area under the position-fluctuation power spectrum:

$T = 300 \text{ K}$   
 $k = 0.87263 \pm 0.062651 \text{ mN/m}$

Predicted frequency noise:

$\%_{\text{ms}} = 50 \text{ nm}$   
 $S_{\text{in}} = 2237.8956 \pm 225.8997 \times 10^{-6} \text{ Hz}^2/\text{Hz}$   
 $S_{\text{det}} = 1.5511 \pm 0.27982 \times 10^{-9} \text{ 1/Hz}$

Figure E.2: (a) Power spectrum of cantilever position fluctuations. The solid line is the thermal contribution and the dotted line is the instrument noise floor contribution. (b) Analysis of position fluctuations.

Cantilever position fluctuations,  $\delta x(t)$ , were detected using a calibrated interferometer. A 25-second transient of position fluctuations was recorded and its power spectrum computed. Since the decay time of the cantilever could be as long as a second, it was important to record up to 25 seconds of position-fluctuation data in order to accurately capture the lineshape of the cantilever resonance in the power spectrum. Twenty-five transients were averaged to give a position-fluctuation power spectrum,  $P_{\delta x}$ . A representative power spectrum is shown in Fig. E.2(a). The power spectrum was fit to Eq.(E.6), which contains both a thermomechanical contribution and a detector noise floor contribution. The area under the thermomechanical contribution to the power spectrum, equal to  $\langle (\delta x_{\text{th}})^2 \rangle$ , was computed (with error bars) from fitted parameters as described in Sec. VI of the Ref. [14] Supplement.

The spring constant was computed as  $k = k_B T / \langle x_{\text{th}}^2 \rangle$ . A representative spring constant and associated error is shown in Fig. E.2(b):  $8.7 \pm 0.6 \times 10^{-4}$  N/m. The typical error in the measurement of the spring constant is 5 to 10%.

## BIBLIOGRAPHY

- [1] D. Rugar, B.C. Stipe, H.J. Mamin, C.S. Yannoni, T.D. Stowe, K.Y. Yasumura, and T.W. Kenny. Adventures in attonewton force detection. *Appl. Phys. A*, 72:S3, 2001.
- [2] G. Binnig, C.F. Quate, and Ch. Gerber. Atomic force microscope. *Phys. Rev. Lett.*, 56(9):930, 1986.
- [3] T. D. Stowe, K. Yasumura, T. W. Kenny, D. Botkin, K. Wago, and D. Rugar. Attoneutron force detection using ultrathin silicon cantilevers. *Appl. Phys. Lett.*, 71:288, 1997.
- [4] HJ Mamin and D Rugar. Sub-attoneutron force detection at millikelvin temperatures. *Appl. Phys. Lett.*, 79:3358, 2001.
- [5] T. D. Stowe, T. W. Kenny, D. J. Thomson, and D. Rugar. Silicon dopant imaging by dissipation force microscopy. *Appl. Phys. Lett.*, 75:2785, 1999.
- [6] B. C. Stipe, H. J. Mamin, T. D. Stowe, T. W. Kenny, and D. Rugar. Magnetic dissipation and fluctuations in individual nanomagnets measured by ultrasensitive cantilever magnetometry. *Phys. Rev. Lett.*, 86:2874, 2001.
- [7] N. Jenkins, L. DeFlores, J. Allen, T. Ng, S. Garner, S. Kuehn, J. Dawlaty, and J. Marohn. Batch fabrication and characterization of ultrasensitive cantilevers with submicron magnetic tips. *J. Vac. Sci. Technol. B*, 22:909, 2004.
- [8] T.N. Ng, N.E. Jenkins, and J.A. Marohn. Thermomagnetic fluctuations and hysteresis loops of magnetic cantilevers for magnetic resonance force microscopy. *IEEE Trans. Mag.*, 42:378, 2006.
- [9] S. R. Garner, S. Kuehn, J. M. Dawlaty, N. E. Jenkins, and J. A. Marohn. Force-gradient detected nuclear magnetic resonance. *Appl. Phys. Lett.*, 84:5091, 2004.
- [10] C. L. Degen, M. Poggio, H. J. Mamin, C. T. Rettner, and D. Rugar. Nanoscale magnetic resonance imaging. *Proc. Natl. Acad. Sci.*, 106:1313, 2009.
- [11] D. Rugar, R. Budakian, H. J. Mamin, and B. W. Chui. Single spin detection by magnetic resonance force microscopy. *Nature*, 430:329, 2004.

- [12] B. Stipe, H. Mamin, T. Stowe, T. Kenny, and D. Rugar. Noncontact friction and force fluctuations between closely spaced bodies. *Phys. Rev. Lett.*, 87:96801, 2001.
- [13] S. Kuehn, R. Loring, and J.A. Marohn. Dielectric fluctuations and the origins of noncontact friction. *Phys. Rev. Lett.*, 96:156103, 2006.
- [14] S.M. Yazdanian, J.A. Marohn, and R.F. Loring. Dielectric fluctuations in force microscopy: Noncontact friction and frequency jitter. *J. Chem. Phys.*, 128:224706, 2008.
- [15] S.M. Yazdanian, N. Hoepker, S. Kuehn, R.F. Loring, and J.A. Marohn. Quantifying electric field gradient fluctuations over polymers using ultrasensitive cantilevers. *Nano Lett.*, 9:2273, 2009.
- [16] D. Rugar, H. Mamin, P. Guethner, S.E. Lambert, J. Stern, I. McFadyen, and T. Yogi. Improved fiber-optic interferometer for atomic force microscopy. *Appl. Phys. Lett.*, 55:2588, 1989.
- [17] Y. Martin, D. Abraham, and H. Wickramasinghe. Magnetic imaging by "force microscopy" with 1000 angstrom resolution. *Appl. Phys. Lett.*, 50:1455, 1987.
- [18] C. Frisbie, L. Rozsnyai, A. Noy, M. Wrighton, and C. Lieber. Functional group mapping by chemical force microscopy. *Science*, 265:2071, 1994.
- [19] S. Kuehn, S.A. Hickman, and J.A. Marohn. Advances in mechanical detection of magnetic resonance. *J. Chem. Phys.*, 128:52208, 2008.
- [20] E. Russell, N. Israeloff, and H. Gomariz. Nanometer scale dielectric fluctuations at the glass transition. *Phys. Rev. Lett.*, 81:1461, 1998.
- [21] M. Surin, P. Leclere, R. Lazzaroni, J.D. Yuen, G. Wang, D. Moses, A.J. Heeger, S. Cho, and K. Lee. Relationship between the microscopic morphology and the charge transport properties in poly(3-hexylthiophene) field-effect transistors. *J. Appl. Phys.*, 100:33712, 2006.
- [22] D.M. Eigler and E.K. Schweizer. Positioning single atoms with a scanning tunnelling microscope. *Nature*, 344:524, 1990.
- [23] M. Ternes, C. Lutz, C. Hirjibehedin, F. Giessibl, and A. Heinrich. The forces needed to move an atom on a surface. *Science*, 22:1066, 2008.

- [24] Y. Martin, D.W. Abraham, and H.K. Wickramasinghe. High-resolution capacitance measurement and potentiometry by force microscopy. *Appl. Phys. Lett.*, 52:1103, 1988.
- [25] G.M. Sacha, A. Verdaguer, J. Martinez, J.J. Saenz, D.F. Ogletree, and M. Salmeron. Effective tip radius in electrostatic force microscopy. *Appl. Phys. Lett.*, 86:123101, 2005.
- [26] E.M. Muller and J.A. Marohn. Microscopic evidence for spatially inhomogenous charge trapping in pentacene. *Adv. Mat.*, 17:1410, 2005.
- [27] O. A. Semenikhin, L. Jiang, T. Iyoda, K. Hashimoto, and A. Fujishima. Atomic force microscopy and Kelvin probe force microscopy evidence of local structural inhomogeneity and nonuniform dopant distribution in conducting polybithiophene. *J. Phys. Chem.*, 100:18603, 1996.
- [28] L. Chen, R. Ludeke, X. Cui, A.G. Schrott, C.R. Kagan, and L.E. Brus. Electrostatic field and partial Fermi level pinning at the pentacene-SiO<sub>2</sub> interface. *J. Phys. Chem. B*, 109:1834, 2005.
- [29] L. Burgi, H. Sirringhaus, and R.H. Friend. Noncontact potentiometry of polymer field-effect transistors. *Appl. Phys. Lett.*, 80:2913, 2002.
- [30] L. Burgi, T.J. Richards, R.H. Friend, and H. Sirringhaus. Close look at charge carrier injection in polymer field-effect transistors. *J. Appl. Phys.*, 94:6129, 2003.
- [31] W. Silveira. *Microscopic view of charge injection in a model organic semiconductor*. PhD thesis, Cornell University, 2004.
- [32] T.N. Ng, W.R. Silveira, and J.A. Marohn. Dependence of charge injection on temperature, electric field, and energetic disorder in an organic semiconductor. *Phys. Rev. Lett.*, 98:066101, 2007.
- [33] L. Burgi, R.H. Friend, and H. Sirringhaus. Formation of the accumulation layer in polymer field-effect transistors. *Appl. Phys. Lett.*, 82:1482, 2003.
- [34] T. Hassenkam, D. R. Greve, and T. Bjornholm. Direct visualization of the nanoscale morphology of conducting polythiophene monolayers studied by electrostatic force microscopy. *Adv. Mater.*, 13:631, 2001.

- [35] L.C. Teague, B.H. Hamadani, O.D. Jurchescu, S. Subramanian, J.E. Anthony, T.N. Jackson, C.A. Richter, D.J. Gundlach, and J.G. Kushmerick. Surface potential imaging of solution processable acene-based thin film transistors. *Adv. Mater.*, 20:4513, 2008.
- [36] L. Burgi, T. Richards, M. Chiesa, R.H. Friend, and H. Sirringhaus. A microscopic view of charge transport in polymer transistors. *Synth. Met.*, 146:297, 2004.
- [37] E.M. Muller and J.A. Marohn. Microscopic evidence for spatially inhomogeneous charge trapping in pentacene. *Adv. Mater.*, 17:1410, 2005.
- [38] T.N Ng, J.A. Marohn, and M.L. Chabinyc. Comparing the kinetics of bias stress in organic field-effect transistors with different dielectric interfaces. *J. Appl. Phys.*, 100:084505, 2006.
- [39] M. Jaquith, E.M. Muller, and J.A. Marohn. Time-resolved electric force microscopy of charge trapping in polycrystalline pentacene. *J. Phys. Chem. B*, 111:7711, 2007.
- [40] T.N Ng, W.R Silveira, and J.A. Marohn. Non-ideal behavior in a model system: Contact degradation in a molecularly doped polymer revealed by variable-temperature electric force microscopy. *Proc. SPIE*, 6336:63360A, 2006.
- [41] O. Tal, Y. Rosenwaks, Y. Preezant, N. Tessler, C.K. Chan, and A. Kahn. Direct determination of the hole density of states in undoped and doped amorphous organic films with high lateral resolution. *Phys. Rev. Lett.*, 95:256405, 2005.
- [42] J.D. Slinker, J. A. DeFranco, M.J. Jaquith, W.R. Silveira, Y.W. Zhong, J.M. Moran-Mirabal, H.G. Craighead, H.D. Abruna, J.A. Marohn, and G.G. Malliaras. Direct measurement of the electric-field distribution in a light-emitting electrochemical cell. *Nature Mater.*, 6:894, 2007.
- [43] L.S.C. Pingree, D.B. Rodovsky, D.C. Coffey, G.P. Bartholomew, and D.S. Ginger. Scanning Kelvin probe imaging of the potential profiles in fixed and dynamic planar LECs. *J. Am. Chem. Soc.*, 129:15903, 2007.
- [44] D.C. Coffey and D.S. Ginger. Time-resolved electrostatic force microscopy of polymer solar cells. *Nature Mater.*, 5:735, 2006.

- [45] L. Walther, Russell V., N. Israeloff, and H. Gomariz. Atomic force measurement of low-frequency dielectric noise. *Appl. Phys. Lett.*, 72:3223, 1998.
- [46] P. S. Crider, M. R. Majewski, Jingyun Zhang, H. Ouckris, and N. E. Israeloff. Local dielectric spectroscopy of polymer films. *Appl. Phys. Lett.*, 91:013102, 2007.
- [47] S. Kuehn. *Force-gradient detected nuclear magnetic resonance and the origins of noncontact friction*. PhD thesis, Cornell University, 2007.
- [48] L.C. Sawyer and D.T. Grubb, editors. *Polymer Microscopy*. Springer, 2008.
- [49] E.M. Muller. *Electric force microscopy of charge trapping in thin-film pentacene transistors*. PhD thesis, Cornell University, 2005.
- [50] Y. Obukhov, K.C. Fong, D. Daughton, and P.C. Hammel. Real time cantilever signal frequency determination using digital signal processing. *J. Appl. Phys.*, 101:034315, 2007.
- [51] T. Stowe. *Extending the lower limits of force detection using micromachined silicon cantilevers*. PhD thesis, Stanford University, 2000.
- [52] J. Yang, T. Ono, and M. Esashi. Surface effects and high quality factors in ultrathin single-crystal silicon cantilevers. *Appl. Phys. Lett.*, 77:3860, 2000.
- [53] T. Yasumura, T. Stowe, E. Chow, T. Pfafman, T. Kenny, B. Stipe, and D. Rugar. Quality factors in micron- and submicron-thick cantilevers. *J. Microelectromechanical Systems*, 9:117, 2000.
- [54] J.M. Nichol, E.R. Hemesath, L. J. Lauhon, and R. Budakian. Displacement detection of silicon nanowires by polarization-enhanced fiber-optic interferometry. *Appl. Phys. Lett.*, 93:193110, 2008.
- [55] P. S. Crider, M. R. Majewski, Jingyun Zhang, H. Ouckris, and N. E. Israeloff. Local dielectric spectroscopy of near-surface glassy polymer dynamics. *J. Chem. Phys.*, 128:044908, 2008.
- [56] A. Chumak, P. Milonni, and G. Berman. Effects of electrostatic fields and Casimir force on cantilever vibrations. *Phys. Rev. B*, 70:85407, 2004.
- [57] A. Volokitin and B. Persson. Resonant photon tunneling enhancement of the van der Waals friction. *Phys. Rev. Lett.*, 91:106101, 2003.

- [58] A. Volokitin and B. Persson. Adsorbate-induced enhancement of electrostatic noncontact friction. *Phys. Rev. Lett.*, 94:86104, 2005.
- [59] J.R. Zurita-Sanchez, J.J. Greffet, and L. Novotny. Friction forces arising from fluctuating thermal fields. *Phys. Rev. A*, 69:022902, 2004.
- [60] J. Labaziewicz, Y. Ge, D. Leibrandt, S. Wang, R. Shewmon, and I. Chuang. Temperature dependence of electric field noise above gold surfaces. *Phys. Rev. Lett.*, 101:180602, 2008.
- [61] S. Kuehn, J.A. Marohn, and R.F. Loring. Noncontact dielectric friction. *J. Phys. Chem. B*, 110:14525, 2006.
- [62] S. Rast, U. Gysin, P. Ruff, C. Gerber, E. Meyer, and D. Lee. Force microscopy experiments with ultrasensitive cantilevers. *Nanotechnology*, 17:S189, 2006.
- [63] Z. Zhang and B. Persson. Theory of friction: Coulomb drag between two closely spaced solids. *Phys. Rev. B*, 57:7327, 1998.
- [64] E. Vidal Russell and N. E. Israeloff. Direct observation of molecular cooperativity near the glass transition. *Nature*, 408:695, 2000.
- [65] K. Sinnathamby, H. Oukris, and N. Israeloff. Local polarization fluctuations in an aging glass. *Phys. Rev. Lett.*, 95:67205, 2005.
- [66] P. S. Crider and N. E. Israeloff. Imaging nanoscale spatio-temporal thermal fluctuations. *Nano Lett.*, 6:887, 2006.
- [67] B. Bagchi, D. Oxtoby, and G. Fleming. Theory of the time development of the Stokes shift in polar media. *Chem. Phys.*, 86:257, 1984.
- [68] P. Wolynes. Linearized microscopic theories of nonequilibrium solvation. *J. Chem. Phys.*, 86:5133, 1987.
- [69] L. Onsager. Electric moments of molecules in liquids. *J. Am. Chem. Soc.*, 58:1486, 1936.
- [70] G. van der Zwan and J. T. Hynes. Time-dependent fluorescence solvent shifts, dielectric friction, and nonequilibrium solvation in polar solvents. *J. Phys. Chem.*, 89:4181, 1985.

- [71] I. Rips, J. Klafter, and J. Jortner. Dynamics of ionic solvation. *J. Chem. Phys.*, 88:3246, 1988.
- [72] E. Lifshitz. The theory of molecular attractive forces between solids. *Sov. Phys. JETP*, 2:73, 1956.
- [73] L. Landau and E. Lifshitz. *Electrodynamics of Continuous Media*. Pergamon, Oxford, 1960.
- [74] A. Volokitin and B. Persson. Theory of rubber friction: nonstationary sliding. *Phys. Rev.B*, 65:115419, 2002.
- [75] J. Mahanty and B. Ninham, editors. *Dispersion Forces*. Academic, London, 1976.
- [76] S. K. Lamoreaux. Casimir forces: Still surprising after 60 years. *Phys. Today*, 60:40, 2007.
- [77] W. Denk and D. Pohl. Local electrical dissipation imaged by scanning force microscopy. *Appl. Phys. Lett.*, 59:2171, 1991.
- [78] A. Volokitin, B. Persson, and H. Ueba. Enhancement of noncontact friction between closely spaced bodies by two-dimensional systems. *Phys. Rev. B.*, 73:165423, 2006.
- [79] K. Fukao, S. Uno, Y. Miyamoto, A. Hoshino, and H. Miyaji. Relaxation dynamics in thin supported polymer films. *J. Non-Cryst. Solids*, 307-310:517, 2002.
- [80] J. Keddie, R. Jones, and R. Cory. Interface and surface effects on the glass-transition temperature in thin polymer films. *Faraday Discuss.*, 98:219, 1994.
- [81] Y. Wada, H. Hirose, T. Asano, and S. Fukutomi. On the dynamic mechanical properties of polymers at ultrasonic frequencies in relation to their glass transition phenomena. *J. Phys. Soc. Jpn.*, 14:1064, 1959.
- [82] J.L. Hutter and J. Bechhoefer. Calibration of atomic-force microscope tips. *Rev. Sci. Instrum.*, 64:1868, 1993.
- [83] T. Albrecht, P. Grütter, D. Horne, and D. Rugar. Frequency modulation de-

- tection using high-q cantilevers for enhanced force microscope sensitivity. *J. Appl. Phys.*, 69:668, 1991.
- [84] B. D. Terris, J. E. Stern, D. Rugar, and H. J. Mamin. Contact electrification using force microscopy. *Phys. Rev. Lett.*, 63:2669, 1989.
- [85] O. Cherniavskaya, L. Chen, V. Weng, L. Yuditsky, and L.E. Brus. Quantitative non electrostatic force imaging of nanocrystal polarizability. *J. Phys. Chem. B*, 107:1525, 2002.
- [86] Ranko Richert. (personal communication).
- [87] R. Bergman, F. Alvarez, A. Alegria, and J. Colmenero. The merging of the dielectric alpha- and beta-relaxations in poly-(methyl methacrylate). *J. Chem. Phys.*, 109:7546, 1998.
- [88] H. Goldstein. *Classical mechanics*. Addison-Wesley, 1980.
- [89] P.M. Borsenberger and D.S. Weiss. *Organic Photoreceptors for Xerography*. Optical Engineering. Marcel Dekker, Inc., New York, 1998.
- [90] D. H. Dunlap, P. E. Parris, and V. M. Kenkre. Charge-dipole model for the universal field dependence of mobilities in molecularly doped polymers. *Phys. Rev. Lett.*, 77:542, 1996.
- [91] S. V. Novikov, D. H. Dunlap, V. M. Kenkre, P. E. Parris, and A. V. Vannikov. Essential role of correlations in governing charge transport in disordered organic materials. *Phys. Rev. Lett.*, 81:4472, 1998.
- [92] R. A. Street, J. E. Northrup, and A. Salleo. Transport in polycrystalline polymer thin-film transistors. *Phys. Rev. B*, 71:165202, 2005.
- [93] M. Abkowitz, J. S. Facci, and J. Rehm. Direct evaluation of contact injection efficiency into small molecule based transport layers: Influence of extrinsic factors. *J. Appl. Phys.*, 83:2670, 1998.
- [94] Dimitrakopoulos C. and P. Malenfent. Organic thin-film transistors for large area electronics. *Adv. Mat.*, 14(2):99, 2004.
- [95] R. McNeill, R. Siudak, J.H. Wardlaw, and D.E. Weiss. Electronic conduction in polymers. I. the chemical structure of polypyrrole. *Aust. J. Chem.*, 16(663):1056, 1963.

- [96] C.K. Chiang, M.A. Druy, S.C. Gau, A.J. Heeger, E.J. Louis, A.G. MacDiarmid, Y.W. Park, and H. Shirakawa. Synthesis of highly conducting films of derivatives of polyacetylene. *J. Am. Chem. Soc.*, 100(3):1013, 1978.
- [97] S. R. Forrest. The path to ubiquitous and low-cost organic electronic appliances on plastic. *Nature*, 428:911, 2004.
- [98] H.E. Katz and Z. Bao. The physical chemistry of organic field-effect transistors. *J.Phys.Chem.B*, 104:671, 2000.
- [99] S.M. Sze. *The physics of semiconductor devices*. Wiley and Sons, 1981.
- [100] W.F. Pasveer, J. Cottaar, C. Tanase, R. Coehoorn, P.A. Bobbert, P.W.M. Blom, D.M. de Leeuw, and M.A.J. Michels. Unified description of charge-carrier mobilities in disordered semiconducting polymers. *Phys. Rev. Lett.*, 94:206601, 2005.
- [101] G. Horowitz. Organic field-effect transistors. *Adv. Mat.*, 10:365, 1998.
- [102] T. Miyazaki, K. Kobayashi, K. Ishida, S. Hotta, T. Toshihisa, K. Matushige, and H. Yamada. Increase in carrier mobility of organic ultrathin-film transistor with increasing molecular layers investigated by kelvin probe force microscopy. *J. Appl. Phys.*, 97:124503, 2005.
- [103] C. Tanase, E.J. Meijer, P.W.M. Blom, and D.M. De Leeuw. Unification of the hole transport in polymeric field-effect transistors and light-emitting diodes. *Phys. Rev. Lett.*, 91:216601, 2003.
- [104] A.R. Brown, C.P. Jarrett, D.M. de Leeuw, and M. Matters. Field-effect transistors made from solution-processed organic semiconductors. *Synth. Met.*, 88:37, 1997.
- [105] M.C.J.M. Vissenberg and M. Matters. Theory of the field-effect mobility in amorphous organic transistors. *Phys. Rev. B*, 57:12964, 1998.
- [106] R. Dost, A. Das, and M. Grell. Time of flight mobility measurements in organic field effect transistors. *J. Appl. Phys.*, 104:0845519, 2008.
- [107] D. Basu, W. Liang, L. Dunn, B. Yoo, S. Nadkarni, A. Dodabalapur, M. Heeney, and I. McCulloch. Direct measurement of carrier drift velocity and mobility in a polymer field-effect transistor. *Appl. Phys. Lett.*, 89:242104, 2006.

- [108] P. Schouten, J. Warman, and M. de Haas. Effect of accumulated radiation dose on pulse radiolysis conductivity transients in a mesomorphic octa-n-alkoxy-substituted phthalocyanine. *J. Phys. Chem.*, 97:9863, 1993.
- [109] H. Tanaka, S. Watanabe, H. Ito, K. Marumoto, and S. Kuroda. Direct observation of the charge carrier concentration in organic field-effect transistors by electron spin resonance. *Appl. Phys. Lett.*, 94:103308, 2009.
- [110] J. Park, Y. Qi, D. Ogletree, P. Thiel, and M. Salmeron. Influence of carrier density on the friction properties of silicon *pn* junctions. *Phys. Rev. B*, 76:64108, 2007.
- [111] H. Nishizawa and A. Hirao. Relationship between mobility and diffusion coefficient in molecularly doped polymers. *Jap. J. Appl. Phys.*, 45(8):L250, 2006.
- [112] Z. Bao and J. Locklin, editors. *Organic field effect transistors*. CRC Press, 2007.
- [113] H. Tsuji and Y. Furukawa. Voltage-induced infrared spectra from the organic field-effect transistor based on N,N'-bis(3-methylphenyl)-N-N'-diphenyl-1,1'-biphenyl-4,4'-diamine. *Mol. Cryst. Liq. Cryst.*, 455:353, 2006.
- [114] <http://www.cnf.cornell.edu/>.
- [115] W. Scaife and G. McMullin. Instrument artefact in measurements of dielectric properties at relatively low frequencies (5-100 Hz). *Meas. Sci. Technol.*, 5:1576, 1994.
- [116] C. Former, H. Wagner, R. Richert, D. Neher, and K. Mullen. Orientation and dynamics of chainlike dipole arrays: donor-acceptor-substituted oligophenylenevinylenes in a polymer matrix. *Macromol.*, 32:8551, 1999.
- [117] J.A. Henry, Y. Wang, D. Sungupta, and M. Hines. Understanding the effects of surface chemistry on q: mechanical energy dissipation in alkyl-terminated micromechanical silicon resonators. *J. Phys. Chem. B*, 111(1):88, 2007.